

University of Windsor

Scholarship at UWindor

Electronic Theses and Dissertations

Theses, Dissertations, and Major Papers

4-27-2018

A new Measure for Optimization of Field Sensor Network with Application to LiDAR

Farsam Farzadpour
University of Windsor

Follow this and additional works at: <https://scholar.uwindsor.ca/etd>

Recommended Citation

Farzadpour, Farsam, "A new Measure for Optimization of Field Sensor Network with Application to LiDAR" (2018). *Electronic Theses and Dissertations*. 7418.
<https://scholar.uwindsor.ca/etd/7418>

This online database contains the full-text of PhD dissertations and Masters' theses of University of Windsor students from 1954 forward. These documents are made available for personal study and research purposes only, in accordance with the Canadian Copyright Act and the Creative Commons license—CC BY-NC-ND (Attribution, Non-Commercial, No Derivative Works). Under this license, works must always be attributed to the copyright holder (original author), cannot be used for any commercial purposes, and may not be altered. Any other use would require the permission of the copyright holder. Students may inquire about withdrawing their dissertation and/or thesis from this database. For additional inquiries, please contact the repository administrator via email (scholarship@uwindsor.ca) or by telephone at 519-253-3000ext. 3208.

A NEW MEASURE FOR OPTIMIZATION OF FIELD SENSOR NETWORK WITH APPLICATION TO LIDAR

by

Farsam Farzadpour

A DISSERTATION
SUBMITTED TO THE FACULTY OF GRADUATE STUDIES
THROUGH THE DEPARTMENT OF ELECTRICAL AND COMPUTER ENGINEERING
IN PARTIAL FULFILLMENT OF THE REQUIREMENTS FOR
THE DEGREE OF DOCTOR OF PHILOSOPHY
AT THE UNIVERSITY OF WINDSOR

Windsor, Ontario, Canada

2018

© 2018 Farsam Farzadpour

A NEW MEASURE FOR OPTIMIZATION OF FIELD
SENSOR NETWORK WITH APPLICATION TO LIDAR

by

Farsam Farzadpour

APPROVED BY

S. X. Yang, External Examiner
University of Guelph

B. Boufama
School of Computer Science

J. Wu
Department of Electrical and Computer Engineering

B. Shahrrava
Department of Electrical and Computer Engineering

X. Chen, Advisor
Department of Electrical and Computer Engineering

April 17, 2018

Declaration of Co-Authorship and Previous Publication

I. Co-Authorship

I hereby declare that this thesis incorporates material that is result of joint research, as follows: This dissertation incorporates the outcome of a joint research undertaken in collaboration with Dr. Xuebo Zhang under the supervision of professors Xiang Chen. The collaboration is covered in Chapters 3 of the dissertation. The contributions of the Dr. Yongchun Fang, Dr. Philip Church, and Mr. Tong Zhang were primarily through the provision of proof reading and reviewing the research papers regarding the technical and vocabulary contents. In all chapters, the key and primary contributions, experimental designs, data analysis and interpretation, were implemented by the author,

I am aware of the University of Windsor Senate Policy on Authorship and I certify that I have properly acknowledged the contribution of other researchers to my thesis, and have obtained written permission from each of the co-author(s) to include the above material(s) in my thesis.

I certify that, with the above qualification, this thesis, and the research to which it refers, is the product of my own work.

II. Previous Publication

This dissertation includes four original papers that have been previously published/submitted for publication in peer reviewed journals and conferences, as follows:

Thesis Chapter	Citation	Status
Chapter 3.2	F. Farzadpour, X. Zhang, X. Chen, and T. Zhang, (2017, July). "On performance measurement for a heterogeneous planar field sensor network". In <i>Advanced Intelligent Mechatronics (AIM), 2017 IEEE International Conference on</i> (pp. 166-171) (Best Paper Finalist)	Published
Section 4.3	X. Zhang, X. Chen, F. Farzadpour, Y. Fang, "A Visual Distance Approach for Multi-Camera Deployment with Coverage Optimization", submitted to <i>IEEE/ASME Trans. Mechatronics</i> , manuscript no. MECH-01-2017-6279	Accepted with minor revision
Chapter 3.3, 4,6	F. Farzadpour, X. Chen, "Coverage Optimization for Field Sensor Networks: A Comprehensive Approach", intended to be submitted to <i>IEEE/ASME Trans. Mechatronics</i> .	intended to be submitted
Chapter 7	F. Farzadpour, P. Church, and X. Chen, "Modeling and Optimizing the Coverage Performance of the LiDAR Sensor Networks", submitted to 2018 IEEE/ASME International Conference on Advanced Intelligent Mechatronics.	submitted

I certify that I have obtained a written permission from the copyright owner(s) to include the above published material(s) in my dissertation. I certify that the above material describes work completed during my registration as graduate student at the University of Windsor.

I declare that, to the best of my knowledge, my dissertation does not infringe upon anyone's copyright nor violate any proprietary rights and that any ideas, techniques, quotations, or any other material from the work of other people included in my dissertation, published or otherwise, are fully acknowledged in accordance with the standard referencing practices. Furthermore, to the extent that I have included copyrighted material that surpasses the bounds of fair dealing within the meaning of the Canada Copyright Act, I certify that I have obtained a written permission from the copyright owner(s) to include such material(s) in my dissertation.

I declare that this is a true copy of my dissertation, including any final revisions, as approved by my dissertation committee and the Graduate Studies office, and that this dissertation has not been submitted for a higher degree to any other University or Institution.

Abstract

This thesis proposes a solution to the problem of modeling and optimizing the field sensor network in terms of the coverage performance. The term field sensor is referred to a class of sensors which can detect the regions in 2D/3D spaces through non-contact measurements. The most widely used field sensors include cameras, LiDAR, ultrasonic sensor, and RADAR, etc.

The key challenge in the applications of field sensor networks, such as area coverage, is to develop an effective performance measure, which has to involve both sensor and environment parameters. The nature of space distribution in the case of the field sensor incurs a great deal of difficulties for such development and, hence, poses it as a very interesting research problem. Therefore, to tackle this problem, several attempts have been made in the literature. However, they have failed to address a comprehensive and applicable approach to distinctive types of field sensors (in 3D), as only coverage of a particular sensor is usually addressed at the time. In addition, no coverage model has been proposed yet for some types of field sensors such as LiDAR sensors.

In this dissertation, a coverage model is obtained for the field sensors based on the transformation of sensor and task parameters into the sensor geometric model. By providing a mathematical description of the sensor's sensing region, a performance measure is introduced which characterizes the closeness between a single sensor and target configurations. In this regard, the first contribution is developing an Infinity norm based measure which describes the target distance to the closure of the sensing region expressed by an area-based approach. The second contribution can be geometrically interpreted as mapping the sensor's sensing region to an n -ball using a homeomorphism map and developing a performance measure. The third contribution is introducing the measurement principle and establishing the coverage model for the class of solid-state (flash) LiDAR sensors. The fourth contribution is point density analysis and developing the coverage model for the class of mechanical (prism rotating mechanism) LiDAR sensors.

Finally, the effectiveness of the proposed coverage model is illustrated by simulations, experiments, and comparisons is carried out throughout the dissertation. This coverage model is a powerful tool as it applies to the variety of field sensors.

Dedication

❧
to my mother & father,
and
my beloved wife Fereshteh
❧

Acknowledgements

This dissertation is the end of a journey started four years ago and the beginning of a new path in my life. I would like to thank all those people who made this journey possible and a memorable experience for me.

First and foremost, I would like to express my sincere appreciation to my advisor Dr. Xiang Chen for his patience, academic guidance and continuous support of my Ph.D study throughout the research over the past four years. Besides my advisor, I would like to thank the rest of my thesis committee, Dr. Behnam Shahrava, Dr. Boubakeur Boufama, and Dr. Jonathan Wu. They provided valuable feedback toward my research through their insightful comments and encouragement.

Finally, I would like to thank all my fellow graduate students Salman Siddiqui, Tong Zhang, and Youying Hua. In particular, I am grateful to Dr. Xuebo Zhang who has greatly helped me on this project.

My deepest gratitude goes to my parents for their love and support and making me the person I am. Also, my wife who has always been so supportive and helpful.

Contents

Declaration of Co-Authorship and Previous Publication	iii
Abstract	v
Dedication	vi
Acknowledgements	vii
List of Tables	xi
List of Figures	xii
List of Symbols	xiv
1 Introduction	1
1.1 Background	1
1.2 Motivation	5
1.3 Proposition	5
1.4 Thesis Outline	7
 Part I Coverage of Field Sensor	 9
2 State of the Art	10
2.1 Overview	10
2.2 Coverage Model	10
2.3 Sensor Network Deployment	13
2.3.1 Camera Sensor	13
2.3.2 LiDAR Sensor	14
3 Performance Measure	15
3.1 Overview	15
3.2 Infinity-norm Based Performance Measure	15
3.3 Frobenius-norm Based Performance Measure	18
3.3.1 Homeomorphism Map	18
3.3.2 Radial Projection Mapping	19
3.3.3 Sensor Model	20
3.3.4 Task Model	20
3.3.5 Geometric Model	20
3.4 Conclusion	22
4 Coverage of Field Sensor	23
4.1 Overview	23
4.2 Field Sensor Coverage	23

4.3	Field Sensor Network Coverage	24
4.3.1	Environment Model	24
4.3.2	Relevance Model	24
4.3.3	Sensor Network Performance Function	25
4.4	Optimization of Field Sensor Network Coverage	26
4.4.1	Control Law	26
4.4.2	Constrained Control Law	26
4.5	Simulation Validation	27
4.5.1	Circular Sector Sensor Network Deployment	27
4.5.2	Camera Sensor Network Deployment	32
4.6	Conclusion	33
Part II	Application to LiDAR sensor	37
5	LiDAR Sensor Principles	38
5.1	Introduction	38
5.2	Solid-state (Flash) LiDAR	39
5.2.1	Operating Principle	39
5.2.2	Measurement Principle	39
5.2.3	Experimental Validation	45
5.3	Mechanical (Prism rotating) LiDAR	48
5.3.1	Operating Principle	48
5.3.2	Measurement Principle	48
5.3.3	Simulation and Experimental Validation	53
5.4	Conclusion	54
6	Solid-state LiDAR Coverage Model	58
6.1	Overview	58
6.2	Coverage Model of Flash LiDAR	58
6.2.1	Sensor Model	58
6.2.2	Task Model	58
6.2.3	Geometric Model	59
6.2.4	Sensor Coverage Model	61
6.3	Conclusion	61
7	Mechanical LiDAR Coverage Model	63
7.1	Overview	63
7.2	Coverage Model of Mechanical LiDAR	63
7.2.1	Sensor Model	63
7.2.2	Task Model	63
7.2.3	Geometric Model	64
7.2.4	Sensor Coverage Model	64
7.3	LiDAR Sensor Network Coverage Optimization	65
7.4	Conclusion	68
8	Conclusions	70
8.1	Summary of Contributions	70
8.2	Conclusions	71
8.3	Future Research Directions	71
	Theorems, Definitions and Propositions	73

Bibliography	74
Vita Auctoris	82

List of Tables

Table	Page
4.1 Simulation comparison of Zhang et al. [51] and the proposed measure for optimization of camera sensor network deployment.	33
5.1 LiDAR VU8 model specifications for experimental set up.	45
5.2 Comparison of experimental and theoretical results for Flash LiDAR sensor resolutions.	47
5.3 The selected LiDAR (OPAL-120) specifications for simulation and experiment.	53

List of Figures

Figure	Page
1.1 Camera sensor sensing region (viewing frustum).	2
1.2 Ultrasonic sensor sensing region.	3
1.3 Magnetic-field sensor(magnetometer) sensing region [29].	3
1.4 Classification of the single and network of field sensors.	4
1.5 The geometric model of the camera approximated by ellipsoid [39].	6
1.6 The geometric model of the camera represented by a circle [40].	6
1.7 The geometric model of the camera represented by unit cube[51].	7
2.1 The geometry sensor model of the LiDAR sensor represented by sixteen me- dial beam axis[55].	11
2.2 Flash LiDAR geometrical model [59].	12
2.3 LiDAR schematic representation in 3D space[68].	12
3.1 Planar circular sector sensing model coordinate assignment.	16
3.2 The sensor coverage modeling details.	17
3.3 Position of a target point with respect to the boundary of shape U	17
3.4 Representation of an irregular star domain sensing region.	18
3.5 The radial projection mapping of an irregular star region.	19
3.6 The system coordinates description assigned to the sensor.	20
4.1 Field sensor network coverage performance function framework.	24
4.2 Triangular mesh-based surfaces representing a bunny [102].	25
4.3 The visual representation of the sensor coverage model.	27
4.4 Initial sensor network deployment configuration for covering a 2D region.	28
4.5 Final sensor network deployment configuration for covering a 2D region.	28
4.6 Sensor's trajectories history during optimization.	28
4.7 The overall coverage performance functions.	29
4.8 Unconstrained sensor's velocities history.	30
4.9 Number of points covered by more than one sensor.	31
4.10 A set of different target configurations selected for sensitivity analysis.	31
4.11 The performance measure behavior for a set of target configurations.	32
4.12 Initial configuration of camera sensor network which is randomly deployed in 3D space.	34
4.13 Number of covered triangles by camera sensor network during optimization.	34
4.14 Final camera sensor network deployment configuration.	35
4.15 Target area partitioning based on different measures for final sensor network deployment.	36
5.1 The principle of LiDAR sensor sensing method.	38
5.2 Schematic presentation of LiDAR sensors.	39
5.3 Schematic diagram of the laser emission FOV geometry.	40

5.4	Schematic diagram of the receiver FOV geometry.	40
5.5	Description of flash LiDAR Horizontal, Vertical and Depth resolutions.	41
5.6	Schematic representation of flash LiDAR resolution cell.	42
5.7	Relative configuration of emitter and receiver for different systems.	43
5.8	Flash LiDAR sensor ($VU8 - 100^\circ \times 3^\circ$) used for experimental validation.	45
5.9	Experimental set up for vertical resolution validation.	46
5.10	Experimental set up for horizontal resolution validation.	47
5.11	Experimental set up for depth resolution validation.	47
5.12	Screenshot from Leddar VU8 software for depth resolution validation.	48
5.13	Point density requirement example for different applications [113].	49
5.14	Schematic diagram of Risley prism pair steering system.	49
5.15	OPAL-120 (conical) sensor scanning pattern for duration of 1s with 200K Hz PRF).	50
5.16	Illustration of largest non-detectable circle within LiDAR FOV cross-section.	51
5.17	Illustration of different target sensing regions for the target detection application.	53
5.18	The LiDAR sensor (OPAL-120) is placed such that the sensor axis is vertical to the wall for experimental setup.	54
5.19	Experimental and approximated scanning patterns comparison	55
5.20	Target detection using experimental data and approximated data point density.	56
5.21	Target detection using experimental data and maximum detectable range.	56
5.22	Target detection using experimental data and maximum detectable speed.	57
6.1	Overlooking schematic of effective sensing area for co-axial configuration.	59
6.2	Example of the effective sensing region for a co-axial configuration.	60
6.3	Geometric modeling of effective sensing region of flash LiDAR.	60
7.1	The geometric modeling of effective sensing region.	64
7.2	Geometric model of the mechanical scanning LiDAR (prism rotating) sensing region.	65
7.3	The environment model (mesh-based surfaces) selected for area coverage task.	66
7.4	Initial configuration of LiDAR sensor network which is randomly deployed in 3D space.	66
7.5	Final configuration of LiDAR sensor network after optimization.	67
7.6	The overall coverage performance function.	67
7.7	The number of covered triangles by LiDAR sensor network during simulation.	68
7.8	Partitioning of the target area based on the proposed performance measure.	69

List of Symbols

Greek

α_d	Beam divergence (Mechanical LiDAR)
α_i	Central angle of i -th circular sector
β'	Emitter beam diameter
Δ	Scalar value
δ_i	Radius of i -th circular sector
γ, ω, η	Euler angles
λ	Non-negative constant value
Λ_{abc}	Area operator
μ	Decaying rate
ω_i	Sensor's angular velocity
$\phi(\mathbf{v}_t)$	Relevance function
ρ, η	Angles specify target orientation
ρ_p	Point density
ρ_{cr}	CRA point density
τ	Timer resolution
τ_f	Pulse repetition frequency
θ'	Field of view (conical)
θ_1, θ_2	Initial rotatory angles of prisms
θ_a	Acceptable view angle
θ_t	Nominal view angle
ε	Sensor's linear velocity
$\theta_{l,a}$	Azimuth angle
$\theta_{l,e}$	Elevation angle
θ_i	Angle of i -th sensor in F_w
$\varepsilon_{i,\max}, \omega_{i,\max}$	Constraint on Linear and Angular velocities

$K_{\mathbf{x}}, K_{\varphi}$ Step sizes

Sets

\mathbb{B}	Coverage region of the field sensor
\mathbb{B}^n	n -ball, space enclosed by an $(n-1)$ -sphere
\mathbb{D}	Non-negative real numbers
\mathbb{M}	Subset of Real numbers
\mathbb{S}^1	Unit circle in \mathbb{R}^2
\mathbb{S}^n	n -sphere
\mathbb{T}	Target points
$\mathbf{Q}(t)$	Configuration of sensors in time t
\mathbf{V}	Collection of mutually disjoint partitions
S^n	Surface encloses the star domain (D) in \mathbb{R}^3
\mathbf{M}	Domain of interest to be partitioned
D_E	Effective sensing region of the field sensor
D_i	Region in \mathbb{R}^3
D	Open bounded subset of \mathbb{R}^n
J	Convex subset of \mathbb{R}^n
Q	Intersection points in \mathbb{R}^3
s_n	List of sensors

Other Symbols

\mathbf{u}_i^c	Constrained control law
δ_1, δ_2	Deviation angle of prisms
v_t	Target point
\mathcal{H}	Performance function
∂D	Boundary of domain D
\mathbf{n}_s	Sensor optical z-axis
\mathbf{O}_c	center of the star domain in \mathbb{R}^n
\mathbf{p}_i	Arbitrary point in \mathbb{R}^n
\mathbf{q}_i	Sensor configuration
\mathbf{u}	Target surface unit normal
\mathbf{u}_i	Control law
$\mathbf{v}_s, \mathbf{v}_h, \mathbf{v}_g$	Coordinates of the vertices of shape U

\mathbf{x}	Point in \mathbb{R}^3
\mathbf{x}_i	Intersection point in \mathbb{R}^3
A_j	Triangle area
A_{cr}	Cross-section area (at depth z)
c	Speed of light
C_i	Coverage model
d_a	length of laser beam footprint along the X-axis
d_e	Length of laser beam footprint along the Y-axis
D_l, D_o	Laser beam diameter at two different depths
d_s	Performance measure
d_v	Visual distance
f	Focal length
f_1, f_2	Rotatory frequency of prisms
F_i	Implicit surface function
F_s	Sensor frame
F_w	World frame
H	Vertical pixels
K, Y	Topological spaces
L	Distance from the emitter center
l_i	Side length of triangle
n	Number of sensors
P	Depth along z -axis
p_c	Center of maximum undetectable circle (MUC)
R_a	Range resolution (Mechanical LiDAR)
r_b	Laser footprint radius
R_H	Horizontal resolution
R_L	Lateral resolution
R_V	Vertical resolution
$R_{H,E}, R_{V,E}, R_{Ra,E}$	Horizontal, Vertical and Range resolutions (Experimental)
$R_{H,T}, R_{V,T}, R_{Ra,T}$	Horizontal, Vertical and Range resolutions (Theoretical)
R_{Ra}	Range (Depth) resolution (Flash LiDAR)
t	Distance along the ray

t_i	Distance between the intersection point and sensing center along the ray
T_R	Time resolution
t_s	Scanning duration
T_w	Pulse width
t_{fr}	Time frame duration
U, E	Geometric shapes with area of $N_{i,u}$ and $N_{i,w}$
V_i	i -th Voronoi partition
W	Horizontal pixels
X	Point in \mathbb{R}^3
Z_i	Volume of resolution cell
z_M	Maximum acceptable Range
z_m	Minimum detection range
Z_n	Nominal maximum detection range
Z_p	Permissible maximum detection range
Z_R	Depth of imaging
Z_{pr}	Maximum (unambiguous) range
Z_{pw}	Minimum detection range based on emitted pulse width
z_{re}	Received range
z_{tr}	Transmitted range
\mathbf{r}	Target distance in original domain
\mathbf{O}_i	Origin of i -th sensor frame
\mathbf{r}_i	Coordinate of a sensor frame in F_w
\mathbf{r}_t	Coordinate of a target point in F_w
\mathbf{r}_{ti}	Coordinate of target in F_i
\mathbf{s}_i	Position of the i -th sensor in F_w
\mathbf{r}'	Target distance in the mapped domain
wR_s	Sensor rotation matrix with respect to F_w

It is pointless trying to know where the way leads. Think only about your first step,
the rest will come.

Shams Tabrizi (1185-1248)

CHAPTER 1

Introduction

Have patience. All things are
difficult before they become easy.

Saadi Shirazi (1210-1291)

1.1 Background

Sensing the environment plays an important role in the development of robotics and autonomous systems. A sensor is an instrument that can detect and respond to a wide variety of inputs from the physical, chemical or biological environments.

Field Sensor

Regarding the sensing value of the surrounding objects, sensors can be classified into two types: point sensor and field sensor. A point sensor is a sensor that measures a discrete value such as temperature, pressure force, etc. A field sensor, in contrast, can cover a 2D or 3D region through non-contact measurement. Basically, the coverage area/region of a field sensor is regulated by its configuration (pose).

The field sensors are essentially a subset of all directional sensors which possess the feature of orientation in their function. They have received so much attention in both industries and academic communities due to their particular interesting characteristics and performance in many applications. Typically, the field sensors can be used to provide valuable information from the environment; however, they tend to need high computational power. Some examples of field sensors are listed as follows.

A. Camera

Camera sensors are the most widely used field sensors in many industrial applications. They are remote-sensing devices which being used to record and preserve the scenes captured through their lenses. Most cameras being employed today are the digital camera which is incorporated into a variety of devices such as mobile phones (called camera phones), autonomous robotic systems [1], and vehicles [2].

Operating Principle. The light reflected from the object surface enters an enclosed box through the lens, and an image is recorded on the light-sensitive medium. The length of time that light enters is controlled by a shutter mechanism. They have a range up to 1 Km and have a wide field of view, and can observe the colors (Figure 1.1). Nevertheless, they are ineffective in harsh weather conditions and darkness.

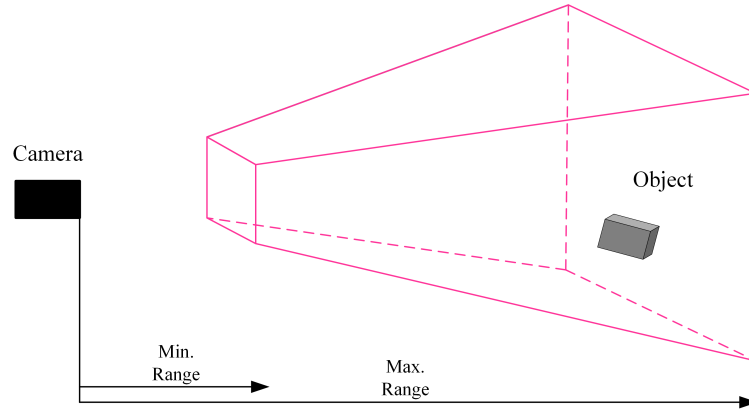


Figure 1.1: Camera sensor sensing region (viewing frustum).

B. Ultrasonic

An ultrasonic sensor (sometimes called ultrasonic transducer) is a device which measures the distance to an object utilizing sound waves. They are mostly used for low speeds and short-range detection. Ultrasonic sensors are used in industrial applications such as water level detection [3], process industry [4], composite structures [5], inspection of welded joints[6], obstacle avoidance [7], fire apparatus [8], and robotic seam tracking [9].

Operating Principle. It operates through recording the elapsed time between sending out a sound wave at a frequency greater than 20 KHz (above the range of human hearing) and the reflected waves (echo) back from them. It works based on the time of flight (ToF) principle. Therefore, considering the speed of the sound wave and the elapsed time, the distance to the object can be determined. However, they cannot recover the position of the targets in 3D space as they have a planar sensing region (Figure 1.2), the atmospheric conditions greatly affect the sensor performance [10]. The ultrasonic beam has a conical shape beam and the distance to the object basically depends on its size, shape, and orientation as well as target surface reflectivity, the temperature, and relative humidity are two major influencing parameters from the environment [11]. The maximum detection range is typically less than 10m [12]. Ultrasonic sensors are short-range sensors due to the attenuation of the sound wave in the air and their slow response time because of the low propagation speed [13]. Furthermore, they are capable of capturing the material property and structure of the object by measuring the reflected signal strength [14].

C. RADAR

The RADAR, which stands for radio detection and ranging, is a system that uses radio waves reflected from the surface of the object to detect the distance, direction, and speed of the object [12]. While common RADARs have 2D coverage and they can only provide range and bearing, the 3D RADARs [15] can also determine the elevation information. Unlike ultrasonic sensors, RADAR sensor is less influenced by temperature. RADARs function mainly for environmental monitoring as it is less affected by environmental factors compared to other sensors [16]. They are used for many applications such as people tracking and data fusion [17], in wind energy applications [18], human motion classification [19], autonomous navigation [20], and safe landing [21].

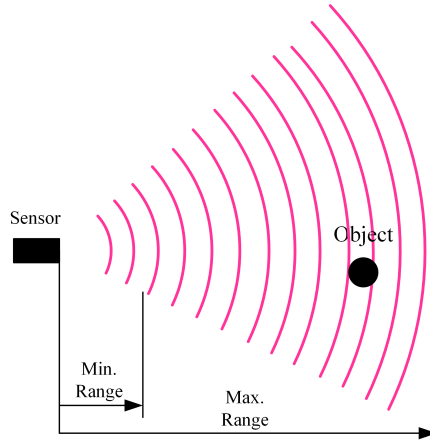


Figure 1.2: Ultrasonic sensor sensing region.

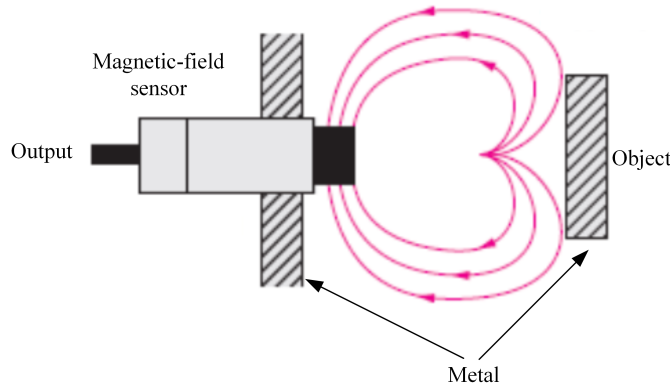


Figure 1.3: Magnetic-field sensor(magnetometer) sensing region [29].

Operating Principle. The RADAR system has five main parts: Transmitter, Duplexer, Receiver, Radar Antenna and Indicator. It transmits a high power pulse with speed of light into space and receives a part of the scattered energy reflected back from the target. It calculates the distance to the target utilizing the time of flight (ToF) measurement, and locate the direction of the target by using the directional antennas. They can be operated at day or night and in all weather conditions (such as fog and rain).

D. Magnetic-field

A magnetic-field sensor is a transducer which can detect a magnetic field from a permanent magnet, an electromagnet, or a current [22] and converts it into an electronic signal [23](Figure 1.3). Different from other sensors, these sensors do not directly measure the physical property of the environment. In addition, the object requires being equipped with a magnet as they are only in reaction to magnets. They are being used for detection, localization, tracking, and discrimination of objects for security and military applications [24]. Nondestructive evaluation, medical [25] and biomedical engineering [26], and obstacle detection and avoidance systems [27] are other examples of the sensor applications [28].

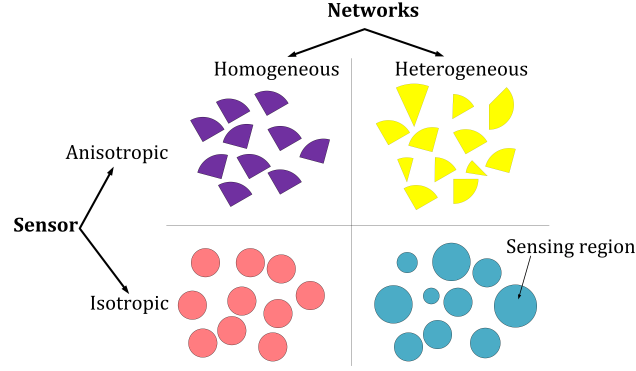


Figure 1.4: Classification of the single and network of field sensors.

Operating Principle. The magnetic-field sensor detect variations (disturbances) within the magnetic fields and provide information on properties such as direction, presence, rotation, angle, or electrical currents [22]. In other words, the output signal also needs to be translated into the desired parameter through some signal processing. This variation would depends on object material and size, view angle (approaching angle), and the distance between the magnets and object. The sensor spatial resolution is usually on the scale of micrometer and it is affected by the distance between the two pairs of magnets [30]. A typical low-cost magnetic sensor having a resolution of 0.1 microteslas would have the maximum detection range of 4cm [31].

So even though it is not easy to implement these type of sensors, they have a diverse range of interest in different applications. This is due to the fact that not only they provide accurate and reliable data measurements [32], environmental effects such as temperature, rain, snow, day, or night have no significant impact on the magnetic signal [33]. According to the sensing variation of the magnetic field, they are often categorized into three groups of the low field [25], Earth field [34], and bias magnetic field [35] sensors.

Field Sensor Network

The field sensors are usually implemented in groups to collect data and share information between each other. They are categorized into two groups of anisotropic (directional) or isotropic based on their dependence on the sensor orientation. In network applications, based on their sensing range, they are generally classified into two groups of homogeneous and heterogeneous networks as depicted in the Figure 1.4.

When it comes to the optimization of the field sensor network deployment, it usually requires minimization or maximization of a performance function which could be a quantitative or qualitative optimization approach. This includes developing a coverage model for the field sensors to assist us to find the position and orientation of sensors placed in the network. In fact, it is a challenging task to measure the performance of a sensor network as it is intimately linked to the coverage quality of the sensors.

Accordingly, there is still a great demand to construct the coverage model of the field sensors which involves developing the sensor and task models as two main parts of the coverage model. The sensor model typically comprises of intrinsic and extrinsic parameters while the task model describes the task-related parameters which are required to be performed (varying with applications).

1.2 Motivation

Autonomy is one of the key elements of the fourth industrial revolution (Industry 4.0 [36]). In autonomous operations, the perception of the environment plays a critical role which needs high-performance sensing accuracy and precision. An economical way to accomplish autonomous operation needs is the implementation of cost-effective field sensor networks. Consequently, the sensors benefit from complementing each other and providing a large scale of field coverage. These types of tasks tend to be difficult for human operators when it is associated with the increase of coverage area or surface complexity. Therefore, the automatic or semi-automatic approaches of field sensor deployment could provide significant advantages over manual solutions to obtain high performance and efficiency.

Generally, two of the most important questions arise out of these types of approaches are: 'How well a single field sensor work?' and 'How well a field sensor network sense some phenomenon?'. One way to address these questions is to establish a coverage performance model of the sensor.

There are various types of field sensors being used for perception of the environment. In contrast to traditional omni-directional field sensors, directional sensors require their own method for modeling the coverage performance [37, 38, 39, 40, 41]. Thus, it is desirable to have a general solution for modeling the coverage of various directional field sensors which is proposed here. In other words, the scope of this dissertation is not limited to developing an approach for modeling the coverage of a particular sensor but a variety of field sensors such as camera, LiDAR, ultrasonic, and RADAR, etc. This will bring us one step closer toward the autonomous operations.

Since there has been no coverage model developed in the literature for the LiDAR sensors, it is selected here as an example of directional field sensor. LiDAR sensor, among other field sensors, is a remote-sensing which can provide required sensing accuracy and precision for autonomous operations. Compared to the camera, the LiDAR measured-data requires low processing power, which allows fast object detection, localization and tracking [42]. LiDAR sensor has been used extensively in today's industries such as mining [43, 44], marine [45], oil [46, 47], etc. to aid real-world automation. Currently, it has received a great attention due to recent advances in LiDAR technology and its application in autonomous driving vehicles [48].

1.3 Proposition

This dissertation addresses the problem of coverage optimization for the field sensors with application to LiDAR sensor networks. One of the difficulties encountered in the modeling of the coverage of directional field sensors is interpreting a measure which can sense not only the position changes but also variations in the orientation of the target with respect to the sensor.

There are many coverage models developed for the camera sensor in the literature which rely on the transformation of different sensor and task parameters into geometric constraints [49, 50]. A geometric model of visual coverage for multi-camera systems was introduced by Mavrinnac [38]. They formulated a coverage model based on eight different task parameters described by geometrical constraints. Despite his improvement in providing a comprehensive coverage model for camera sensor, it was a range-limited partially binary model. Thus, it is necessary to establish a more general coverage model that can function as a continuous performance measure which also has a flexible sensing range based on the applications.

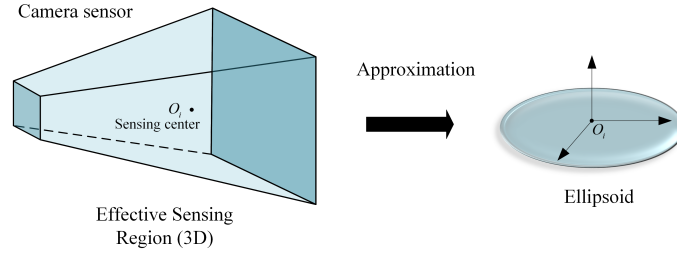


Figure 1.5: The geometric model of the camera approximated by ellipsoid [39].

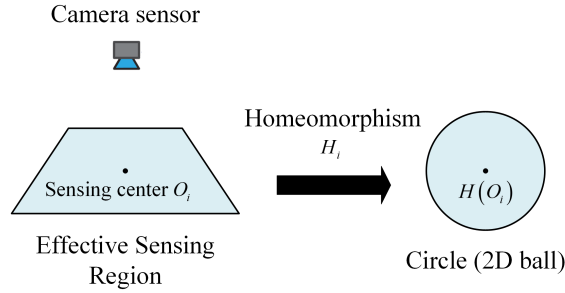


Figure 1.6: The geometric model of the camera represented by a circle [40].

Recently, an appealing idea was proposed by Alarcon [39] in which a geometric model was constructed based on the geometric constraints (Figure 1.5). They developed and validated a sensor-based coverage model (named vision distance), and showed its better performance compare with the coverage model developed by Mavrinac [38] due to the existence of multiple local optima. Nevertheless, this model did not provide sufficient information about the physics of the sensor as the sensing region of the sensor was approximate with an ellipsoid.

To solve this problem, a performance measure (coverage distance) was developed based on an idea of homeomorphism mapping to utilize the sensor exact geometric model (the model obtained from the geometric constraints) [40]. They developed a coverage model based on mapping the 2D anisotropic sensing region to isotropic sensing one (circle)(Figure 1.6). This approach was further extended for developing a coverage model for camera sensor by mapping a 4D visual frustum (a combination of the 3D viewing frustum and view angle) to a 4D unit cube [51](Figure 1.7). They used the infinity norm of an array to construct the performance measure. However, from the optimization point of view, the performance function suffers from the existence of the multiple local optima in some configurations of the sensor and target. This is due to the nature of the infinity norm.

Different from previous works, this dissertation proposes an approach for modeling and optimizing the coverage which is generalized to various types of field sensors where no coverage modeling approach has been reported throughout the literature that can be applied to all types of field sensors. The coverage model for the field sensor is introduced through developing a performance measure which characterize the closeness of the target to the field sensor with considering the position and orientation changes.

Since there is a class of 2D field sensors having a circular sector sensing geometry (such as 2D RADAR or LiDAR), a performance measure is developed based on Infinity norm. In another attempt, the coverage model for the field sensor is developed through

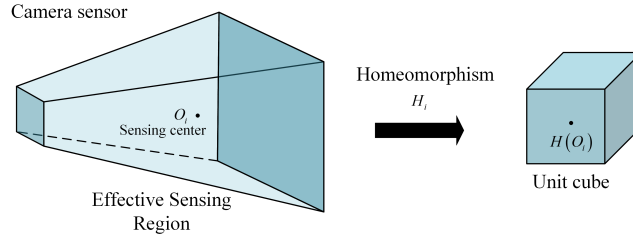


Figure 1.7: The geometric model of the camera represented by unit cube[51].

exploring the sensor parameters and employing the concept of star domain from the set theory. Since the sensing region of the most widely used field sensors such as camera, LiDAR, ultrasonic, and RADAR is star domain, mapping this region to an n -ball (\mathbb{B}^n for $n = 2, 3$) allows construction of a coverage model which can be implemented to different types of 2D/3D field sensors. This is performed by deploying the radial projection of the points of the surface which encloses the star domain, onto an n -sphere (\mathbb{S}^n for $n = 1, 2$) followed by developing a performance measure based on the Frobenius norm.

Based on the proposed performance measurements, the field sensor network is deployed optimally for the area coverage problem through a gradient-based control law. Additionally, simulation and experimental results are provided to assess the practical aspect of the presented approach. To further validate this approach, a comparison with the performance measure presented by Zhang et al. [51] is made.

1.4 Thesis Outline

The first part of the dissertation aims at providing a literature review of the sensor coverage model and deployment of field sensor networks in Chapter 2. This includes reviewing the state of the art in modeling the field sensors; in particular, mechanical and solid-state LiDAR sensors in Section 2.2, followed by sensor network deployment in Section 2.3. Chapter 3 introduces two performance measures based on Infinity-norm and Frobenius-norm for construction of field sensor coverage model established in Chapter 4. These non-negative scalar functions reveal the degree of closeness of a target to the sensor considering both relative position and orientation. A performance measure is developed for the class of 2D fields sensors in Section 3.2. Utilizing the definition of star domain and considering orientation change of the target with respect to the sensor, a Frobenius-norm based measure is introduced in 3.3 which can be applied to the field sensors having in 2D/3D sensing regions. Chapter 4 presents the coverage of single (Section 4.2) and network of field sensors(Section 4.3) along with optimization of field sensor network coverage in Section 4.4 and simulations for validation of the proposed performance measure as well as coverage of field sensor network in Section 4.5.1 and 4.5.2

The second part of this dissertation deals with the application of the field sensor coverage model for LiDAR sensors. It begins with introducing the measurement principles of two classes of solid-state (flash) and mechanical (prism rotating) LiDARs in Chapter 5. The simulation and experimental verifications for the measurement principle of both LiDARs are provided in Section 5.2.3 and 5.2.3. Developing the coverage model for solid-state (flash) LiDAR comes after in Chapter 6. The coverage model is introduced by defining the sensor geometric model obtained from sensor and task parameters in Section 6.2. The optimization of the mechanical LiDAR sensor networks is conducted in Chapter 7. In this chapter, coverage model of the LiDAR having Risley-

prism rotating mechanism is proposed (Section 7.2) using the coverage model developed in Chapter 4. This involves developing the geometric model of the sensor considering sensor and task models. Simulation is also conducted for coverage optimization of the mechanical LiDAR sensor network in Section 7.3 to verify the proposed coverage model and the optimization framework for LiDAR sensor.

The contributions of the works performed in this dissertation are provided in Section 8.1 followed by proposing some potential future directions in Section 8.3.

Part I

Coverage of Field Sensor

CHAPTER 2

State of the Art

You yourself are your own
obstacle, rise above yourself.

Hafez (1315-1390)

2.1 Overview

In literature, there are several works addressing the coverage of a single or a network of field sensors, some examples are taken and presented here. Since the LiDAR sensor is selected as an application example for field sensor coverage model developed in this dissertation, in this chapter more attention has been paid on the state of the art in the modeling of the LiDAR sensor. The modeling of LiDAR sensor has not received enough attention during recent years, especially in modeling the sensor coverage. Only a few studies have been conducted on the modeling and deployment of LiDAR sensor networks, which are presented throughout this chapter.

2.2 Coverage Model

The literature has lots of examples of sensor's model demonstrating isotropic and homogeneous properties in their capability. An isotropic model for heterogeneous locational optimization of autonomous agents was proposed by Guruprasad et al. [52] in which they used an arbitrary non-optimal node function. The mobile agents equipped with anisotropic (elliptic) sensors was studied [53] wherein they approximated the sensor model with an isotropic model. Another study on anisotropic sensors performed by Ai et al. [54] in which they attempted to maximize the coverage with a minimum number of sensors via implementation of a distributed greedy algorithm (DGA). However, in this study the sensing region was modeled with a binary detection model that is not often an efficient and practical solution.

Since in real life applications, most of the commonly used field sensors networks are dealing with anisotropic sensing area (region), the optimization of a planar heterogeneous anisotropic sensor network deployment in area coverage problem is discussed in detail in Section 4.5.1 for performance measure 3.2 validation purpose.

There are several studies reported to model LiDAR sensor behavior in the literature for both solid-state and mechanical LiDAR sensors which are listed in following subsection.

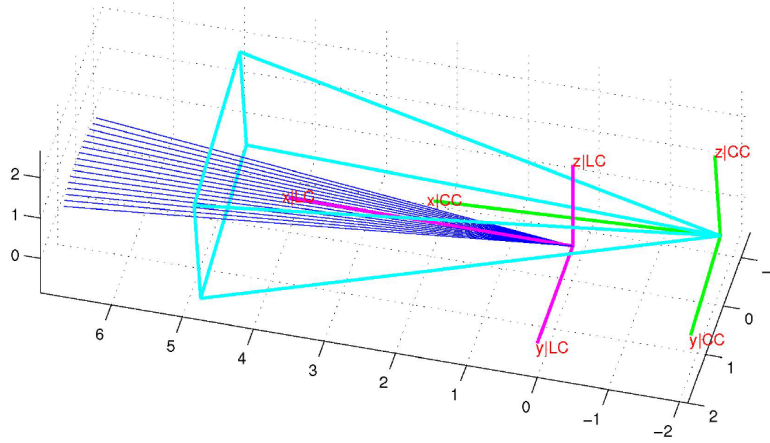


Figure 2.1: The geometry sensor model of the LiDAR sensor represented by sixteen medial beam axis[55].

Solid-State LiDAR

The solid-state LiDAR sensors (such as flash LiDAR) have many advantages over mechanical LiDAR sensors, including simplicity, efficiency, high measurement speed, and lower price.

A geometry sensor model was considered by Mahlich et al. [55] for a flash LiDAR sensor. They modeled the sensor with sixteen medial beam axis, and projected the rays onto the image domain in a detection and tracking framework (Figure 2.1). An incoherent model was introduced by Dolce [56] to specify the relation between target intensity and received intensity in the focal plane.

Flash LiDAR sensors are extensively implemented for surveillance and exploration to detect obstacles for safety guidance of unmanned ground or aerial vehicles in the defense sector [57]. Although these sensors currently have a smaller Field of view (FOV) compare to mechanical LiDAR, the ongoing advances in FOV improvement make those flash LiDAR sensors a more viable candidate for the sake of environmental surveillance and exploration.

Zhao et al. [58] developed and implemented a flash LiDAR model to illustrate the influence of atmospheric turbulence on 3D target range imagery. However, they obtained blurred images due to the spreading impact of the optical-beam during turbulence effect.

Since the flash LiDAR and camera sensor have the similar structure, in a very recent study, a geometrical model based on the pinhole camera model was developed by Jang et al. [59] for modeling the flash LiDAR (Figure 2.2). In this study, a sensor performance analysis was carried out by considering the focal length, resolution, and pixel size for some advanced driver assistance system (ADAS) applications. However, the relative geometry of emitter and detector as well as detector specifications were not considered in modeling the LiDAR sensor.

Mechanical LiDAR

The performance of robots in localization and mapping is greatly influenced by the sensor measurement models. Some models are constructed based on the LiDAR measurement such as feature-based and correlation-based models [60]. A probabilistic model of LiDAR sensor based on the interaction between the beam and the environment, including uncertainty of measurement was introduced by Schaefer et al. [61] which can be considered as a beam-based (ray cast) measurement model.

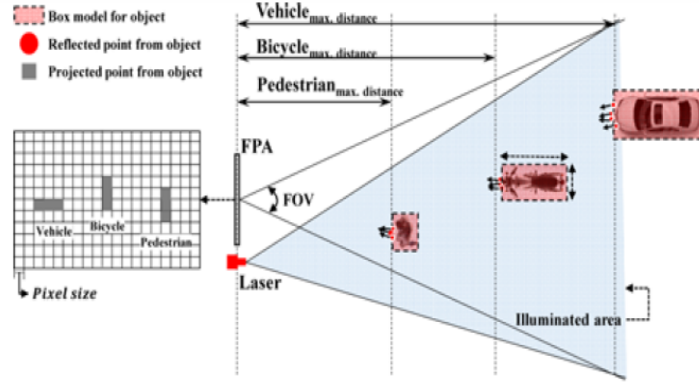


Figure 2.2: Flash LiDAR geometrical model [59].

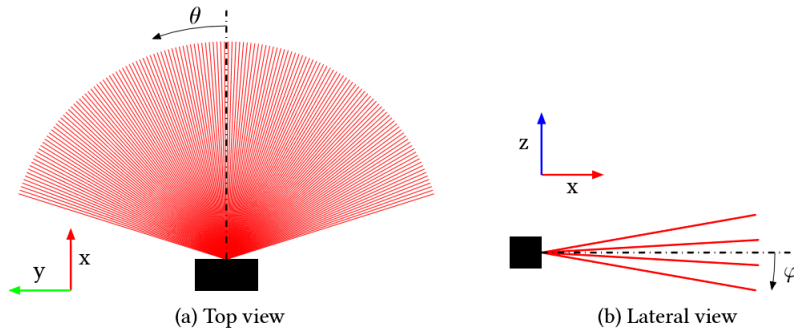


Figure 2.3: LiDAR schematic representation in 3D space[68].

A simple circular sensor model for application of tracking persons was proposed [62, 63] where the beam was modeled as an oriented planar (2D) triangular shape while the lateral profile of the beam was not considered. The full-angle beam width and the distance measurement error as the most effective design parameters were taken into consideration.

Two sensor models for the LiDAR sensor were deployed for low and high-attenuation returns providing information for occupied voxel space and the free voxel space [64]. A mathematical model for point positioning of LiDAR sensor was developed based on the physical sensor model [65]. This model determines the relation between system measurements and LiDAR coordinates.

Several developed LiDAR models are based on the point-intersection model which utilizes the ray tracing technique [66, 57]. However, they suffer from inaccurate behavior prediction of the robot in the complex environments [67].

A 3D Lidar sensor model using probabilistic approaches proposed by Postigo Fernández [68] for the problem of generating occupancy grid map with application to autonomous driving (Figure 2.3). In this study, every laser beam was modeled individually to estimate the probability of occupancy. A probabilistic 2D occupancy map model for an unmanned aerial vehicle is developed based on physics of the LiDAR sensor, including measurement and clutter noise [69]. They showed that drifting motion is an inherent issue in detection of large obstacles using LiDAR sensor. A geometric model of LiDAR systems is suggested by Min et al. [70] that accounts for the LiDAR system sensors (GPS and INS), laser scanner and their corresponding systematic error.

To the best of our knowledge, no research has been conducted to address the coverage model as a specific mechanism to evaluate the LiDAR sensor sensing capability and quality.

2.3 Sensor Network Deployment

One of the important aspects of system integration is optimal sensor network deployment which has received significant attention in the field of robotics, control and sensor networks.

Recent researches in the literature, have addressed the problem of locational optimization for heterogeneous [40, 71, 72, 73, 74] and anisotropic [53, 75] networks. The 2D k-coverage problem proposed by Shi et al. [76] in which a coverage model was developed for an anisotropic sensor network. However, the sensor directions were selected randomly from a limited set of directions which may restrict the coverage performance. In fact, deploying an efficient field sensor network requires an optimal sensor placement strategy. A probability inspired binary particle swarm optimization (PI-BPSO) algorithm to solve the issue of homogeneous sensor network placement was introduced in a research by Fu et al. [77]. The sensor placement (deployment) problem was investigated by Chen et al. [78] for the model-based vision tasks. In their study, the optimal sensor placement graph was achieved using the concept of the genetic algorithm and evaluated by means of the min-max criterion. While there are several researches performed for solving optimal sensor placement problem using heuristic methods [79], there is no guarantee for these methods to get the optimal solution as the sensor network deployment problem is an NP-hard problem [80].

An recursive convex optimization approach was proposed by Zhang et al. [41] to accelerate the computation speed. They defined a resolution criterion including both the distance and the view angle simultaneously.

A coverage optimization approach based on differential evolution is proposed by Zhang et al. [81]. They used a parallel visual occlusion detection algorithm to increase the computing efficiency. The problem of isotropic sensor network deployment having a limited sensing range was addressed by Cortes et al. [82].

A lot of works has been done on distributed optimization approaches [83], [84, 85, 86, 87, 79]. The deployment of the sensors is performed using the Voronoi partition in a spatially distributed way. In addition, a quantitative assessment of the sensing performance was conducted to formulate the problem through a function of the Euclidean distance.

In another study, a non-Euclidian based coverage function is proposed by Farzadpour et al. [88] in which the problem of optimal deployment of heterogeneous anisotropic field sensor network, having different sensing range, is investigated. A more recent study for area coverage problem which addresses the coverage control of mobile robots having heterogeneous sensing capabilities is conducted by Santos et al. [89].

Since the majority of the existing works in this area are mainly conducted in the 2D space, further investigation of sensor modeling in 3D space is required.

2.3.1 Camera Sensor

In many security and entertainment applications, visual information is of the extreme importance [90, 91, 92]. There are many criteria such as camera FOV, resolution, blur, view angle and occlusion, which need to be considered simultaneously in camera coverage modeling. Based on various task requirements, many different approaches have been proposed for modeling of the visual coverage. For example, a multi-camera coverage model was presented by Schwager et al. [84], including resolution-like criterion and FOV

constraint; however, other criteria are not modeled. A generic visual coverage model proposed by Mavrinac [38], where the model was validated through simulation and applied in industrial inspection tasks and view selection. They employed a linear interpolation to assign coverage strength between 0 and 1 for each task point. In another attempt, a coverage model was applied for the camera sensor network deployment [93]. Where a camera overlap graph was constructed in which a greedy algorithm was designed to obtain a better-optimized solution.

2.3.2 LiDAR Sensor

Deployment of an inexpensive network of LiDAR sensors can provide high-performance sensing accuracy and high precision for autonomous operations. However, there is a limited number of works in literature regarding LiDAR sensor network deployment optimization.

One example of LiDAR sensor's network application is tracking objects inside the surveillance area. The detection, localization, and tracking of the objects inside the area of surveillance has been investigated through centralized [94] and decentralized [63] manner. The solution to address the problem of LiDAR sensor network deployment for a surveillance application was proposed by Wenzl et al. [62, 63]. In their study, the configuration of the sensors was determined through selection from a limited set of configurations. In addition, since the target area was not completely covered by the sensor network beams, they used kinematics of moving objects to track them within uncovered regions. Later, they further improved this issue by proposing a decentralized architecture [95]. A LiDAR sensor network was deployed to estimate motion parameters of a small size aircraft having low landing speed [96]. They deployed a network of four Velodyne VLP-16 along taxiways and runways to obtain the required geospatial data to estimate the velocity.

In this dissertation, a generic framework for optimization of field sensor networks deployment is presented. The key part of this framework is the development of a performance measure for the field sensors. Although this framework borrowed in some part from [38] and [41], it is intended to be a more comprehensive approach in scope than previous work, as it not only provides a more competent performance measure but also extends to most common types of field sensors (such as camera, LiDAR, ultrasonic, and RADAR).

Performance Measure

He who searches for his beloved
is not afraid of the world.

Nizami Ganjavi (1141-1209)

3.1 Overview

In this chapter, two different approaches are proposed for construction of the performance measure which reveals the coverage strength of the target to the field sensor. These measures are a non-negative scalar-valued function which characterizes the closeness between the target point and the field sensor in configuration space. Basically, to develop these measures, a model of the sensor as well as the task to be performed are required.

3.2 Infinity-norm Based Performance Measure

Development of a performance measure for the class of field sensors which can be modeled by a planar circular sector is presented in this section. In this approach, the Infinity-norm is utilized to the performance measure along with defining the necessary and sufficient condition for the coverage of target point.

Let consider a set $\mathbf{M} \subset \mathbb{R}^2$. Let set $\mathbf{B} \subset \mathbf{M}$ denote the coverage region of a field sensor which can be modeled by a planar circular sector. It has the radius of $\delta_i \in \mathbb{R}^+$ (which is the set of positive numbers) and central angle of $\alpha_i \in \mathbb{S}^1$ in radians as depicted in Figure 3.1.

Let $F_s(X_i o_i Y_i)$ denote the frame attached to the i -th sensor with its origin located at \mathbf{O}_i , and defined in word frame $F_w(X_w o_w Y_w)$. The sensor configuration is encapsulated as $\mathbf{q}_i = [\mathbf{s}_i^T \theta_i]^T \in (\mathbb{R}^2 \times \mathbb{S}^1)$, where $\mathbf{s}_i = [x_i \ y_i]^T$ is the position of the sensor in frame F_w and θ_i represents the angle defined by counterclockwise rotation of sensor frame (F_s) about the axis perpendicular to the $X_w Y_w$ -plane. Let $\mathbf{T} \subset \mathbf{M}$ denote the set of (target) points whose coverage strength needs to be evaluated. It is assumed that for all target points $\mathbf{v}_t \in \mathbf{T} \cap \mathbf{B}$ have the same coverage strength. Let $\mathbf{r}_t = [x_t \ y_t]^T$ denote the coordinate of a target point $\mathbf{v}_t \in \mathbf{T}$ in frame F_w . Given the position of the a target point \mathbf{v}_t in frame F_w , then its coordinate in frame F_s is obtained as:

$$\mathbf{r}_{ti} = [\mathbf{r}_t - \mathbf{r}_i] \quad (3.1)$$

and its distance from origin \mathbf{O}_i defined by $r_{ti} = \|\mathbf{r}_{ti}\|$ where $\|\cdot\|$ denotes the euclidean norm. Let's define two geometric shapes U and E with the area of $N_{i,u}$ and $N_{i,w}$,

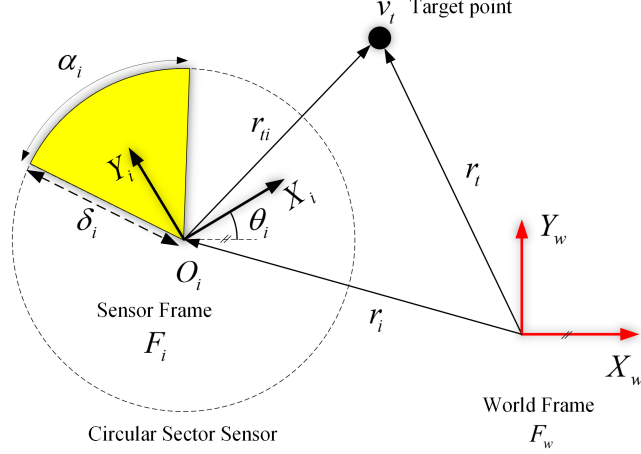


Figure 3.1: Planar circular sector sensing model coordinate assignment.

respectively (as shown in 3.2) such that subtracting W from U will be equal to the sensor's model with area of N_i . In other words, $N_i = N_{i,u} - N_{i,w}$. Then, the coordinates of the vertices of the triangle (in shape U) are obtained as:

$$\mathbf{v}_s = \mathbf{r}_i \quad (3.2)$$

$$\mathbf{v}_h = l_i \begin{bmatrix} \cos(\sigma) & \sin(\sigma) \end{bmatrix} \quad (3.3)$$

$$\mathbf{v}_g = l_i \begin{bmatrix} \cos(\zeta) & \sin(\zeta) \end{bmatrix} \quad (3.4)$$

where $\sigma = \frac{1}{2}(\pi - \alpha_i) + \theta_i$, $\zeta = \frac{1}{2}(\pi + \alpha_i) + \theta_i$, and $l_i \geq \delta_i$ is the side length of triangle U , and all vertices (\mathbf{v}_s , \mathbf{v}_h and \mathbf{v}_g) are defined in frame F_w .

Definition 3.1 (Circular sector coverage). For a target point \mathbf{v}_t , to be covered by a circular sector sensor model; it is required to satisfy the following two conditions: I) Fall within or on the boundary of the geometry shape U . II) Its distance from the origin of the sensor's coordinate (r_{ti}) should be less than or equal to the sensor's radius (δ_i), In other words, $r_{ti} \leq \delta_i$.

Definition 3.2 (Area operator). Given three vertices $a = [a_x, a_y]$, $b = [b_x, b_y]$ and $c = [c_x, c_y] \in \mathbb{R}^2$ of a triangle in 2-D space, the operator Λ_{abc} which yields the area of the triangle, is defined as follows:

$$\Lambda_{abc} = \frac{1}{2} \det \begin{vmatrix} a_x & a_y & 1 \\ b_x & b_y & 1 \\ c_x & c_y & 1 \end{vmatrix} \quad (3.5)$$

To check the first condition, an area test is performed as follows: Given a sensor configuration \mathbf{q}_i and a target point $\mathbf{v}_t \in \mathbb{T}$ (as a vertex); three triangles are constructed by making edges through connecting \mathbf{v}_t to the three vertices of the U denoted as \mathbf{v}_s , \mathbf{v}_g and \mathbf{v}_h as shown in Figure 3.3, and calculating the total area of these triangles $A_j \in \mathbb{R}$ for $j = 1, 2, 3$. Referring to the Definition 3.2, those areas of triangles for the i -th sensor are computed as $A_1 = \Lambda_{tgs}$, $A_2 = \Lambda_{tsh}$ and $A_3 = \Lambda_{tgh}$. Now, we compare the total area of these triangles with the area of U . The point is inside or on the boundary of this geometric shape if $\sum_{j=1}^3 A_j = N_{i,1}$; otherwise, it is outside of this area, and first condition is not satisfied. To check the second condition, the target point is transformed

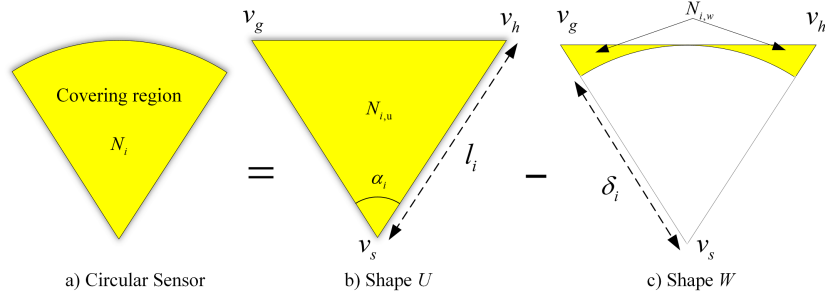
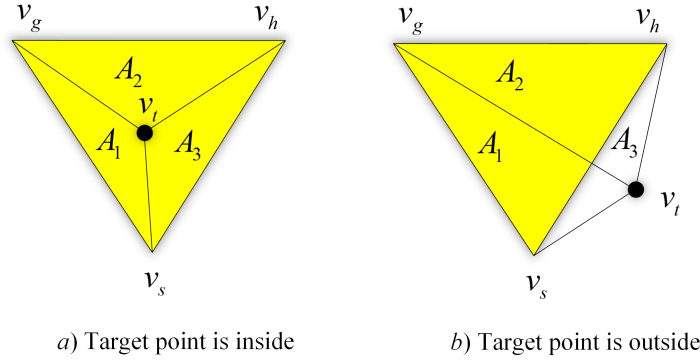


Figure 3.2: The sensor coverage modeling details.


 Figure 3.3: Position of a target point with respect to the boundary of shape U .

from frame F_w to F_s using (3.1), and its distance (r_i) is compared with the circular sector radius (δ_i). By considering these two conditions, the performance measure of a target point (v_t) with respect to the i -th sensor $d_s : \mathbb{R}^2 \times \mathbb{S}^1 \rightarrow \mathbb{D}$ where $\mathbb{D} = \{x \in \mathbb{R} | x \geq 1\}$, is obtained as

$$\begin{aligned} d_s(\mathbf{q}_i, \mathbf{v}_t) &= \left\| \begin{bmatrix} \Gamma(\mathbf{q}_i, \mathbf{v}_t) & \Psi(\mathbf{q}_i, \mathbf{v}_t) \end{bmatrix}^T \right\|_{\infty} \\ &= \max(|\Gamma(\mathbf{q}_i, \mathbf{v}_t)|, |\Psi(\mathbf{q}_i, \mathbf{v}_t)|) \end{aligned} \quad (3.6)$$

where $\Gamma(\mathbf{q}_i, \mathbf{v}_t)$ and $\Psi(\mathbf{q}_i, \mathbf{v}_t)$ are functions corresponding to the conditions one and two, defined as

$$\Gamma(\mathbf{q}_i, \mathbf{v}_t) = \frac{\sum_{j=1}^3 A_j(\mathbf{q}_i, \mathbf{v}_t)}{N_{i,1}} \quad (3.7)$$

$$\Psi(\mathbf{q}_i, \mathbf{v}_t) = \frac{r_i}{\delta_i} \quad (3.8)$$

Theorem 3.1 (Necessary and sufficient condition for coverage). *A necessary and sufficient condition for a target point to be covered is $d_s(\mathbf{q}_i, \mathbf{v}_t) = 1$.*

Proof. According to the definition 3.1, for any target point to be covered, first condition should be satisfied, in other words, $\Gamma(\mathbf{q}_i, \mathbf{v}_t) = 1$. Also, when the second condition is satisfied $r_i \leq \delta_i$ which means $\Psi(\mathbf{q}_i, \mathbf{v}_t) \leq 1$. Therefore, $\max(|\Gamma(\mathbf{q}_i, \mathbf{v}_t)|, |\Psi(\mathbf{q}_i, \mathbf{v}_t)|) = 1$. ■

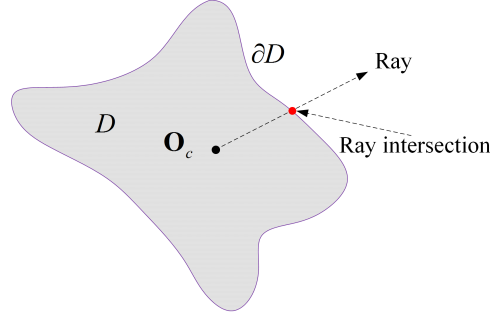


Figure 3.4: Representation of an irregular star domain sensing region.

3.3 Frobenius-norm Based Performance Measure

In this section, a performance measure is developed which can be applied to the field sensors having 2D/3D sensing regions. This measure which is based on the frobenius-norm is inspired from concept of star domain from the set theory. It is obtained by mapping the sensing region of the field sensors to the \mathbb{B}^n followed by considering orientation change of the target with respect to the sensor. Furthermore, the necessary and sufficient condition for coverage of target in 3D space by the field sensor is defined.

3.3.1 Homeomorphism Map

The preliminary concepts of convex and star-domain sets followed by introducing the radial projection map for mapping a star domain onto a \mathbb{B}^n is presented here. The motivation behind this mapping is to enable us to define a measure that characterizes the closeness of a point to the sensor sensing region.

Mathematical Preliminaries

Let's first recall the definition of convex and star-convex sets.

Definition 3.3 (Convex set).

A set $J \subseteq \mathbb{R}^n$ is convex, if for any two points $\mathbf{p}_1, \mathbf{p}_2 \in J$ the line segment connecting \mathbf{p}_1 and \mathbf{p}_2 is also in J . In other words, $\lambda \mathbf{p}_1 + (1 - \lambda) \mathbf{p}_2 \in J$ for $\lambda \in [0, 1]$. Visually, this means that the set has no dents or holes.

Definition 3.4 (Star-convex set).

An open bounded set $D \subseteq \mathbb{R}^n$ is star-convex set (star-shaped or star domain) if it contains a point $\mathbf{O}_c \in D$ such that every ray issuing from \mathbf{O}_c intersect ∂D (boundary) in exactly one point. The set D is then called a star-convex set with respect to \mathbf{O}_c (Figure 3.4).

Remark 3.1 (Convexity of star domain).

According to the above definitions, any convex domain is star convex while the converse is not true.

Although it can be shown that the sensing region $D \subset \mathbb{R}^3$ of the most common type of field sensors are star domain, one possible solution to the real-world shapes that are not star shaped is to segment the shape into a set of disjoint star shapes and finally glue the patches together [97]. The definition 3.4 suggests a method for mapping such a domain to \mathbb{B}^n . This is performed through specifying an interior point \mathbf{O}_c , namely the center of the domain, and using the radial projection. Thus, this was the motivation for the construction of proposed performance measure.

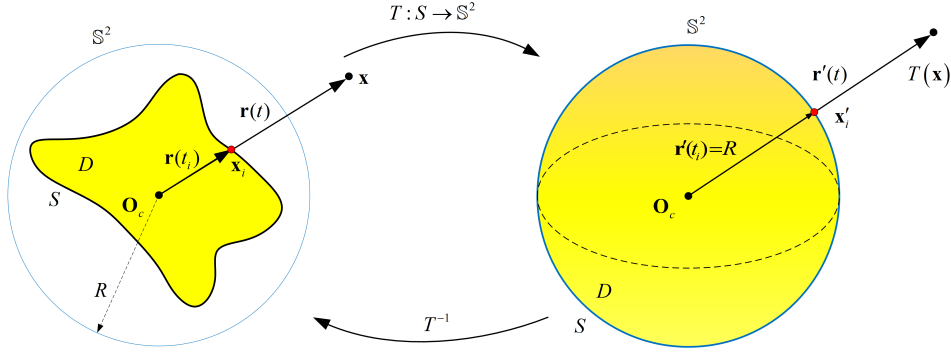


Figure 3.5: The radial projection mapping of an irregular star region.

3.3.2 Radial Projection Mapping

Definition 3.5 (Homeomorphism map).

The map $f : K \rightarrow Y$ of the topological spaces is called a homeomorphism if it is bijective and f^{-1} is also continuous. Thus, we say that K and Y are homeomorphic.

Proposition 3.1 (Radial projection map).

Let S be regular and compact (closed and bounded) surface in \mathbb{R}^3 , the radial projection [98] map $T : S^{n+1} \rightarrow S^n$ (n -sphere for $n = 1, 2$) is a homeomorphism map.

Proof. Since the unit n -sphere $S^n \subset \mathbb{R}^{n+1}$ is a compact space, then every continuous bijective map from a compact space to a Hausdorff space is a homeomorphism map [99]. Therefore, T is a homeomorphism map. ■

Proposition 3.2 (Homeomorphism between surface and sphere).

The surface S^{n+1} which encloses the star domain is homeomorphic to S^n by radial projection.

Proof. Since the surface S^{n+1} that encloses the star domain is compact, based on Proposition 3.1, its radial projection map $T : S^{n+1} \rightarrow S^n$ is a homeomorphism map. ■

Generally, surfaces are being represented mathematically by either implicit or parametric functions [100]. Let $F(\mathbf{X}) = 0$ for $\mathbf{X} \in \mathbb{R}^3$ be an implicit surface defined in Euclidean space. Let $D \subset \mathbb{R}^3$ denote a star domain by surface $S \subset \mathbb{R}^3$ (Figure 3.5). Given a point $\mathbf{x} \in \mathbb{R}^3 - \{\mathbf{O}_c\}$, the parametric equation of the ray starting at the given point \mathbf{O}_c that extends in the direction of vector \mathbf{u} , is given by

$$\mathbf{r}(t) = \mathbf{O}_c + t\mathbf{u} \quad (3.9)$$

where the unit vector \mathbf{u} is defined as

$$\mathbf{u} = \frac{\mathbf{x} - \mathbf{O}_c}{\|\mathbf{x} - \mathbf{O}_c\|} \quad (3.10)$$

where $\|\cdot\|$ denotes the Euclidean norm and $t \in \mathbb{R}^+$ is the distance along the ray. Then, by inserting parametric ray equation $\mathbf{r}(t)$ into implicit surface representation of S , $F(\mathbf{r}(t)) = 0$, the intersection point $\mathbf{x}_i \in \mathbb{R}^3$ of ray $\mathbf{r}(t)$ and the surface S , is obtained by solving $F(\mathbf{r}(t)) = 0$ for t , given by

$$\mathbf{x}_i = \mathbf{r}(t_i) = \mathbf{O}_c + t_i\mathbf{u} \quad (3.11)$$

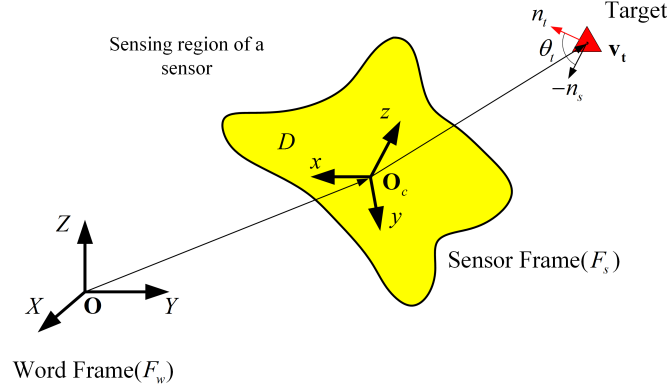


Figure 3.6: The system coordinates description assigned to the sensor.

Therefore, the radial projection T which maps $S \subset \mathbb{R}^3$ to \mathbb{S}^2 (2-sphere of radius R) is defined by

$$T(\mathbf{x}) = \mathbf{r}(t) \frac{R}{\|\mathbf{r}(t_i)\|} ; \forall \mathbf{x} \in D, \mathbf{x}_i \in S \quad (3.12)$$

3.3.3 Sensor Model

The sensor model is an abstract description of the physical sensors which includes two sets of parameters termed intrinsic and extrinsic parameters. The former is a set of generic parameters which often determined by the sensor manufacturer and varies from one type of field sensor to another. For example, the pinhole model is usually adopted for camera sensor which includes the focal length, pixel dimensions, principle point and image size (height and width) as well as aperture size. The latter is a set of parameters describing the position and orientation of the sensor in \mathbb{R}^3 with respect to a world frame. Let $F_s : (x, y, z)$ denote the frame attached to the field sensor with its origin located at point \mathbf{O}_c , and defined in world frame $F_w : (X, Y, Z)$ with the origin $\mathbf{O} \in \mathbb{R}^3$ as illustrated in Figure 3.6. The six degrees of freedom (DOF) of a sensor's pose—namely, position components and orientation angles relative to the world frame (F_w), are the extrinsic parameters of the sensor, defined as

$$\mathbf{q} = [\mathbf{x}_s, \Phi]^T \quad (3.13)$$

where $\mathbf{x}_s = [x_s, y_s, z_s]$ and $\Phi = [\eta, \omega, \gamma]$ (Euler angles). The position and orientation of a triangular mesh (target) can be encapsulated in a vector $\mathbf{v}_t \in \mathbb{R}^3 \times [0, \pi] \times [0, 2\pi]$, named directional point [38], as $\mathbf{v}_t = [\mathbf{x}, \varphi]^T$ where $\mathbf{x} = [x, y, z]^T$ and $\varphi = [\rho, \sigma]^T$ are the position and orientation terms, respectively, defined in the frame F_w .

3.3.4 Task Model

One of the most critical parts of the coverage model is the description of the task model. It consists of a set of parameters specifying the required sensing quality of the environment. For example, for an industrial surveillance application using camera sensor, it could include FOV, focus (image blur), view angle and resolution.

3.3.5 Geometric Model

The effective sensing region of the field sensor (D_E) is obtained from transformation of sensor and task model parameters into geometric constraints. The mathematical

description of this region is provided by sensor geometric model. To map D_E to the \mathbb{B}^n using radial projection, it is required to have the implicit representation of the surfaces available. In other words, the geometric model of the region should be available.

Definition 3.6 (Directional point coverage).

For a directional point, to be covered by a field sensor, it requires not only to fall inside or on the boundary of the sphere but also needs to satisfy the view angle criterion. In other words, its viewing angle should be less or equal to the acceptable view angle.

Position Consideration. Let T denote the set of all directional points whose coverage strength needs to be evaluated. Let D_E denote the given effective sensing region of a field sensor. By using the radial projection T , the region $D_E \subset \mathbb{R}^3$ is mapped to the \mathbb{B}^n . Thus, the distance of a target to the sensing center in the new (mapped) domain, is obtained by

$$\|r'(t)\| = \|r(t)\| \frac{R}{\|r(t_i)\|} \quad (3.14)$$

Thus, for any target point $\mathbf{v}_t \in T \cap D_E$, according to Equation (3.12), we can define a non-negative function $\Gamma \in [0, \infty)$ as,

$$\Gamma(\mathbf{x}) = \frac{\|r'(t)\|}{\|r'(t_i)\|} \quad (3.15)$$

where $\|r'(t_i)\| = R$ is the radius of the \mathbb{S}^n (for $n = 1, 2$). By substitution of Equation (3.14) into above equation, we can define $\Gamma(\mathbf{x})$ in the initial domain as

$$\Gamma(\mathbf{x}) = \frac{\|r(t)\|}{\|r(t_i)\|} \quad (3.16)$$

$\Gamma(\mathbf{x})$ is defined as the proximity of target with respect to the center of sensing region in the Euclidean sense. In other words, when $\Gamma(\mathbf{x}) \leq 1$, the target is located inside the sensing region.

Orientation Consideration. Once the position difference is specified between sensor and target, it is required to calculate the orientation difference. The angle between target's normal (\mathbf{n}_t) and the opposite direction of the sensor optical z -axis (\mathbf{n}_s) is called (nominal) view angle parameter (θ_t), obtained by

$$\theta_t = \cos^{-1}(-\mathbf{n}_s \cdot \mathbf{n}_t) \quad (3.17)$$

where \mathbf{n}_s and \mathbf{n}_t are unit vectors, defined as follow:

$$\mathbf{n}_s = {}^w\mathbf{R}_s \mathbf{I}_3 \quad (3.18)$$

$$\mathbf{n}_t = \begin{bmatrix} \sin(\rho) \cos(\eta) & \sin(\rho) \sin(\eta) & \cos(\rho) \end{bmatrix}^T \quad (3.19)$$

where $\mathbf{I}_3 = [0 \ 0 \ 1]^T$ and ${}^w\mathbf{R}_s$ is the sensor rotation matrix with respect to the world frame (F_w) and defined using Euler angles as ${}^w\mathbf{R}_s = \mathbf{R}_z(\gamma) \mathbf{R}_y(\omega) \mathbf{R}_x(\eta)$, which is obtained by rotation about X , Y and Z axis by η , ω and γ , respectively, as follow:

$$\mathbf{R}_z(\gamma) = \begin{bmatrix} \cos(\gamma) & -\sin(\gamma) & 0 \\ \sin(\gamma) & \cos(\gamma) & 0 \\ 0 & 0 & 1 \end{bmatrix} \quad (3.20)$$

$$\mathbf{R}_y(\omega) = \begin{bmatrix} \cos(\omega) & 0 & \sin(\omega) \\ 0 & 1 & 0 \\ -\sin(\omega) & 0 & \cos(\omega) \end{bmatrix} \quad (3.21)$$

$$R_x(\eta) = \begin{bmatrix} 1 & 0 & 0 \\ 0 & \cos(\eta) & -\sin(\eta) \\ 0 & \sin(\eta) & \cos(\eta) \end{bmatrix} \quad (3.22)$$

Thus, the non-negative function $\Psi : [0, \pi] \rightarrow [0, \infty)$ is defined as,

$$\Psi(\varphi) = \frac{\tan(\theta_t/2)}{\tan(\theta_a/2)} \quad (3.23)$$

where θ_a is the acceptable view angle specified based on application. This function determines the degree of alignment between target and sensor. In other words, $\Psi(\varphi) \leq 1$ means the view angle criterion is satisfied. Now, we need to define a function which can measure both position and orientation of the target with respect to the sensor. This is performed by utilizing the Frobenius norm as follow,

$$d_s(\mathbf{q}, \mathbf{v}_t) = \left\| \begin{bmatrix} \Gamma & \Psi & \Delta(\Gamma + \Psi) \end{bmatrix}^T \right\|_F \quad (3.24)$$

where $d_s : \mathbb{R}^3 \times [0, \pi] \times [0, 2\pi] \rightarrow \mathbb{R}^+$, $\|\cdot\|_F$ is the Frobenius norm, and Δ is defined as

$$\Delta = \lfloor \max(\Gamma, \Psi) \rfloor^+ \quad (3.25)$$

where $\lfloor x \rfloor^+$ denote the largest integer smaller than x . For a given configurations of target and sensor, this measure characterizes their closeness through providing a scalar value.

Theorem 3.2 (Necessary and sufficient condition for coverage). *A necessary and sufficient condition for a task point to be covered by a field sensor is that $d_s(\mathbf{q}, \mathbf{v}_t) \leq \sqrt{2}$.*

Proof. For any point $\mathbf{x} \in S$ inside or on the boundary of the sphere its distance from the center of the sphere $\|r(t)\| \leq R$, so that, $\Gamma(\mathbf{x}) = \frac{\|r(t)\|}{R} \leq 1$.

Also, since any target point needs to satisfy the view angle condition of $\theta_t \leq \theta_a$, so that $\Psi(\varphi) = \frac{\tan(\theta_t/2)}{\tan(\theta_a/2)} \leq 1$. Hence $\max(\Gamma, \Psi) \leq 1$. Then, according to Equation

(3.25), $\Delta(\mathbf{v}_t) = 0$. So $\left\| \begin{bmatrix} \Gamma & \Psi & \Delta(\Gamma + \Psi) \end{bmatrix}^T \right\|_F = \left\| \begin{bmatrix} \Gamma & \Psi \end{bmatrix}^T \right\|_2$. By considering $\Gamma(\mathbf{x}) = \Psi(\varphi) = 1$, its maximum value is obtained as $\sqrt{2}$. This implies that $\left\| \begin{bmatrix} \Gamma & \Psi & \Delta(\Gamma + \Psi) \end{bmatrix}^T \right\|_F \leq \sqrt{2}$. ■

3.4 Conclusion

Two performance measures are introduced in this chapter. While the first measure is developed for the class of 2D field sensors, the second one is proposed for a more general case (3D) which can be applied to any kind of field sensors. In addition, the necessary and sufficient condition for coverage of target by the field sensor for both measures are defined.

These measures, as an atomic unit, later will be used for construction of the coverage of field sensor in next chapter. Furthermore, the validation of the proposed norm-based measures will be carried out through simulation in Section 4.5 after introducing the coverage of field sensor network.

Coverage of Field Sensor

He who searches for his beloved
is not afraid of the world.

Nizami Ganjavi (1141-1209)

4.1 Overview

The problem of optimizing the field sensor network deployment includes developing a coverage model for the field sensor and finding a sensor network configuration which optimizes the overall coverage performance of the network, is conducted in this chapter.

The modeling of field sensor coverage is, in fact, the process of establishing a scalar coverage performance measure as presented in Chapter 3. The sensor network coverage performance is constructed from the extension of the single sensor coverage. In other words, it is obtained from integration of all sensor coverage. This helps in the prediction of the sensor network coverage performance and will be used to simulate and optimize the deployment of field sensor networks.

4.2 Field Sensor Coverage

The capability and quality of a field sensor can be described by the sensor coverage models which depends upon the physical properties of the sensor as well as required parameters of the task that needs to be performed. For example, for a camera sensor, it could include: resolution, FOV, view angle and focus [101].

Due to the existence of many factors such as signal attenuation and the presence of noise, the sensor sensing quality decreases as the distance from the sensor increases. Thus, to characterize the sensing quality of the sensor more accurately, the coverage model of the sensor is constructed using an exponential attenuation model as follows,

$$C_i(\mathbf{q}_i, \mathbf{v}_t) = e^{-\mu d_s(\mathbf{q}_i, \mathbf{v}_t)} \quad (4.1)$$

where $d_s(\mathbf{q}_i, \mathbf{v}_t)$ is the performance measure and $\mu > 0$ is the decaying rate which is a property of the physical space. This model, as a single sensor to single target point coverage model, is used to construct the performance function of the field sensor network.

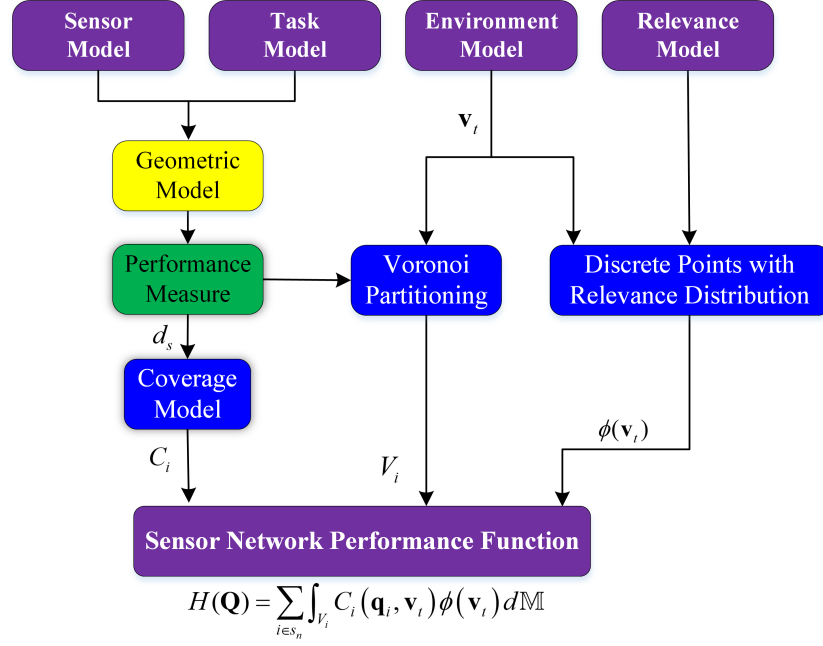


Figure 4.1: Field sensor network coverage performance function framework.

4.3 Field Sensor Network Coverage

A generic framework for optimization of the field sensor networks deployment is presented in this section (Figure 4.1)¹. The four inputs of this framework are sensor model, task model, environment model and relevance model. The key part of this framework is the construction of the coverage model developed in Section 3.2 using the proposed performance measure. The sensor model and task model are already defined in Section 3.3. The brief description of environment and relevance model is also provided in following.

4.3.1 Environment Model

Any 3D model of the environment may be expressed to an arbitrary degree of precision by triangular mesh-based surfaces as basic atomic units (Figure 4.2). To evaluate the coverage of any of these triangles, both the position (with considering the vertices) and the normal direction of the triangle face should be considered. Therefore, to determine any triangular mesh coverage mathematically, we utilize the definition of directional point introduced in Section 3.3.3.

4.3.2 Relevance Model

The degree of importance of triangles in the environment model is described by the relevance model which is the spatial distribution of each triangle and depends on the task requirement. For example, the surveillance of selected forest areas, roads and mining regions might require higher relevance value.

¹This dissertation incorporates the outcome of a joint research which Dr. Xuebo Zhang has undertaken in collaboration with myself under the supervision of professor Xiang Chen.

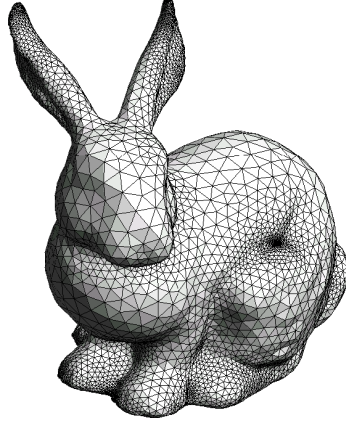


Figure 4.2: Triangular mesh-based surfaces representing a bunny [102].

4.3.3 Sensor Network Performance Function

For distributed computation, dynamic partitioning of the working space is needed. One of the most conventional techniques in the partitioning of an environment is using the Voronoi diagram. The performance of a field sensor network can then be defined as sum of the contributions of all sensors according to their assigned voronoi partition. In fact, we are seeking to find a configuration of sensors that minimize the performance function.

Voronoi Partitioning

While traditional Voronoi partitioning approaches use Euclidian distance, here the environment model (triangular meshes) is partitioned into (disjoint) regions based on the proposed performance measure. The domain of interest \mathbb{M} (target domain) is the space that requires to be partitioned. Let $s_n = \{1, 2, \dots, n\}$ and $\mathbf{Q}(t) = \{\mathbf{q}_1(t), \mathbf{q}_2(t), \dots, \mathbf{q}_n(t)\}$ be the configuration of n sensors at time t . Let's define a modified Voronoi partitioning such that $\mathbb{M} = \cup_{i \in s_n} V_i$, where $\mathbf{V} = \{V_i\}$ is a collection of mutually disjoint interiors, defined as

$$V_i = \{\mathbf{v}_t \in \mathbb{T} | d_s(\mathbf{q}_i, \mathbf{v}_t) \leq d_s(\mathbf{q}_j, \mathbf{v}_t), \forall j \neq i, j \in s_n\} \quad (4.2)$$

Since $d_s(\mathbf{q}_i, \mathbf{v}_t) = Y_1$ or Y_2 , where

$$Y_1 = \left\| \begin{bmatrix} \Gamma & \Psi \end{bmatrix}^T \right\|_F \quad (4.3)$$

and

$$Y_2 = \left\| \begin{bmatrix} \Gamma & \Psi & \Delta(\Gamma + \Psi) \end{bmatrix}^T \right\|_F \quad (4.4)$$

by dividing each partition V_i into two sub-partitions such that

$$V_i = V_i^1 \cup V_i^2 \quad (4.5)$$

we have

$$V_i^1 = \{\mathbf{v}_t \in \mathbb{T} | d_s(\mathbf{q}_i, \mathbf{v}_t) = Y_1\} \quad (4.6)$$

and

$$V_i^2 = \{\mathbf{v}_t \in \mathbb{T} | d_s(\mathbf{q}_i, \mathbf{v}_t) = Y_2\} \quad (4.7)$$

Therefore, the overall performance function of the network is given by

$$\mathcal{H}(\mathbf{Q}) = \int_{\mathbb{M}} \max_{i \in s_n} \{C_i(\mathbf{q}_i, \mathbf{v}_t)\} \phi(\mathbf{v}_t) d\mathbb{M} \quad (4.8)$$

Having dynamic Voronoi partitioning, the above equation can be written as

$$\mathcal{H}(\mathbf{Q}) = \sum_{i \in s_n} \int_{V_i} C_i(\mathbf{q}_i, \mathbf{v}_t) \phi(\mathbf{v}_t) d\mathbb{M} \quad (4.9)$$

where $\phi(\mathbf{v}_t) \in \mathfrak{R}$ is the relevance function which is a measure of relative importance of target point \mathbf{v}_t . In other words, those points being associated with greater weighting values will have smaller (better) coverage strength.

4.4 Optimization of Field Sensor Network Coverage

A gradient-based optimization approach is applied in this section to optimize sensor network performance function \mathcal{H} .

4.4.1 Control Law

Let consider a first-order sensor dynamics, the control law is defined as

$$\dot{\mathbf{q}}_i(t) = \mathbf{u}_i(t) \quad (4.10)$$

where

$$\mathbf{u}_i(t) = [\mathbf{x}_i \quad \boldsymbol{\omega}_i]^T = \left[K_x \frac{\partial H}{\partial \mathbf{x}_{s_i}(t)} \quad K_\varphi \frac{\partial H}{\partial \Phi_i(t)} \right]^T \quad (4.11)$$

where the control law \mathbf{u}_i guides the sensors toward gradient direction for a positive K_x and K_φ . The trajectories of the sensors governed by control law (4.4.1) with any initial configuration having an appropriate constant step sizes (K_x and K_φ) will converge to the critical points of \mathcal{H} (configurations where the $\frac{\partial \mathcal{H}}{\partial \mathbf{q}_i}$ is zero) [103, 52].

4.4.2 Constrained Control Law

Let's define a speed constraints on the sensor's linear velocity $\varepsilon = \|\mathbf{x}_i\|$ where $\|\cdot\|$ is the euclidian norm and angular ω_i velocity as $\varepsilon_{i,\max}$ and $\omega_{i,\max}$, respectively for $i \in s_n$. Thus, in order to take into account the speed constraints, the constrained control law is defined as follows:

$$\mathbf{u}_i^c = [\mathbf{x}_i^c \quad \boldsymbol{\omega}_i^c]^T \quad (4.12)$$

where

$$\mathbf{x}_i^c = \begin{cases} \mathbf{x}_i & \|\mathbf{x}_i\| \leq \varepsilon_{i,\max} \\ \varepsilon_{i,\max} \frac{\mathbf{x}_i}{\|\mathbf{x}_i\|} & \text{otherwise} \end{cases} \quad (4.13)$$

$$\boldsymbol{\omega}_i^c = \begin{cases} \boldsymbol{\omega}_i & \boldsymbol{\omega}_i \leq \boldsymbol{\omega}_{i,\max} \\ \boldsymbol{\omega}_{i,\max} \text{sgn}(\boldsymbol{\omega}_i) & \text{otherwise} \end{cases} \quad (4.14)$$

This control law, under a constraint on maximum speeds, guides the sensors toward the gradient direction that leads to the critical points of \mathcal{H} . Chapter 4 provides an example of constrained control law implementation.

The gradient of the performance function \mathcal{H} with respect to i -th sensors configuration \mathbf{q}_i , is obtained through applying the general form of Leibniz theorem [104] for differentiating an integral, as

$$\frac{\partial \mathcal{H}}{\partial \mathbf{q}_i} = \int_{V_i} \frac{\partial}{\partial \mathbf{q}_i} C_i(\mathbf{q}_i, \mathbf{v}_t) \phi(\mathbf{v}_t) d\mathbb{M} \quad (4.15)$$

To compute the partial derivative of $\frac{\partial}{\partial \mathbf{q}_i} C_i(\mathbf{q}_i, \mathbf{v}_t)$ it is required that C_i be at least piece-wise differentiable. It can prove that the proposed performance measure has this

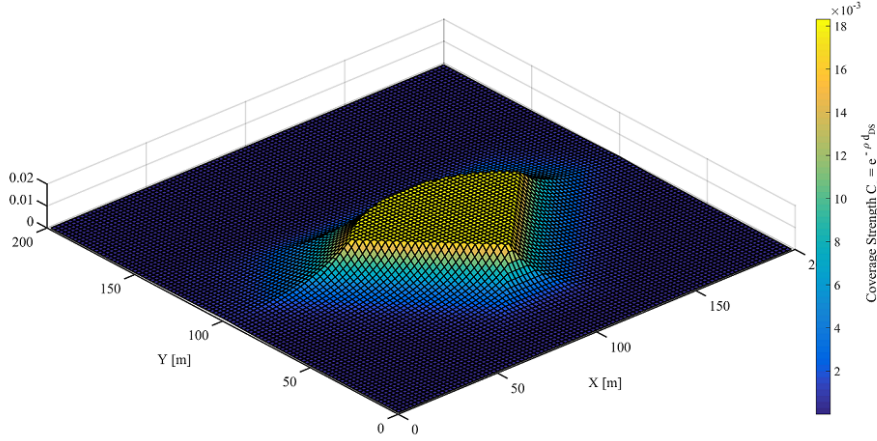


Figure 4.3: The visual representation of the sensor coverage model.

property. Since, the gradient given by Equation (4.15) depends only on the assigned partition V_i , value of $\phi(\mathbf{v}_t)$ and the sensor's coverage function $C_i(\mathbf{q}_i, \mathbf{v}_t)$, by considering sub-partitions of V_i , we have

$$\frac{\partial \mathcal{H}}{\partial \mathbf{q}_i} = \int_{V_i^1} \frac{\partial}{\partial \mathbf{q}_i} \left(e^{-\mu_d Y_1} \right) \phi(\mathbf{v}_t) d\mathbf{M} + \int_{V_i^2} \frac{\partial}{\partial \mathbf{q}_i} \left(e^{-\mu_d Y_2} \right) \phi(\mathbf{v}_t) d\mathbf{M} \quad (4.16)$$

4.5 Simulation Validation

In this section, to evaluate the proposed measures in Chapter 3, simulations for the problem of area coverage using a mobile field sensor network deployment is conducted here. An example of heterogeneous planar field sensor network, having different sensing range, is considered to validate the Infinity-norm based performance measure developed in Section 3.2. In addition, to validate the Frobenius-norm base performance measure developed in Section 3.3, optimization of a camera sensor network deployment is carried out and a comparison validation is performed.

4.5.1 Circular Sector Sensor Network Deployment

A network of $n = 13$ sensors placed in a random initial configuration in a discretized 2-D square environment with the size of $100 \times 100\text{m}$ (having a set of 10,000 target points) as shown in Figure 4.4. The radius δ_i and FOV of circular sectors α_i are selected randomly. Let the relevance function $\phi(\mathbf{v}_t) = 1$ for $\forall \mathbf{v}_t \in \mathbb{T}$, and the decaying rate for all sensor's coverage model be $\mu = 4$. The sensor coverage model Equation 4.1 is visualized in Figure 4.3.

For the given network configuration, two gradient based control laws have been implemented: i) constrained, ii) unconstrained. The proportional constants are set as $K_x = 5$ and $K_\varphi = 0.02$, and maximum linear and angular speeds are selected as $\varepsilon_{i,\max} = 5 \text{ m/s}$ and $\omega_{i,\max} = 0.2 \text{ rad/s}$, respectively. After $t = 500$ sec, sensors spread over almost the whole area as it has shown in Figures 4.5(a) and (b).

Figures 4.6(a) and (b) shows the trajectories of sensors for both control laws. The starting location of the sensors is shown with a circle marker.

Figure 4.7 illustrates the performance evaluation process of the overall coverage performance function during the optimization under both control laws. It is clear that \mathcal{H} has gradually increased under both control laws.

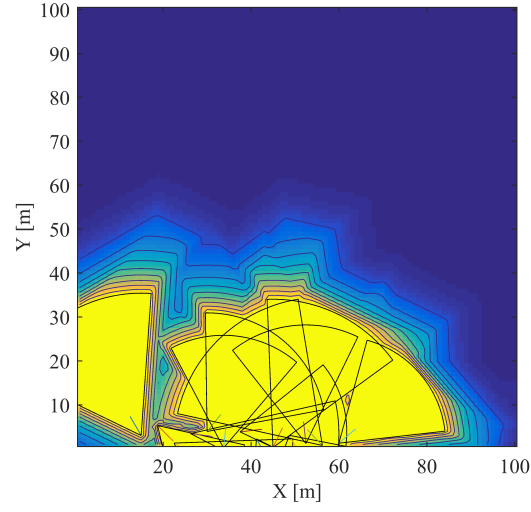
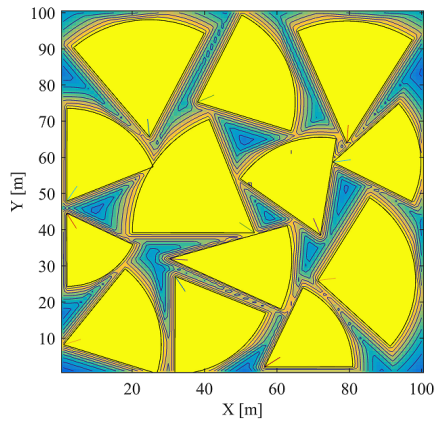
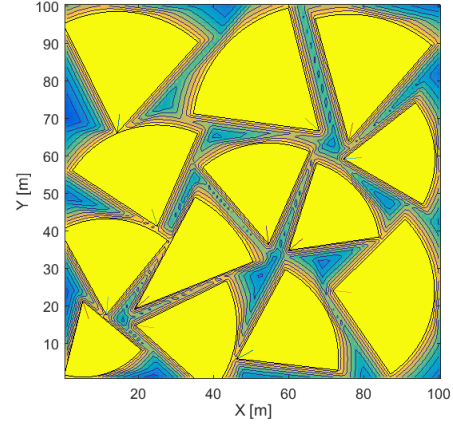


Figure 4.4: Initial sensor network deployment configuration for covering a 2D region.

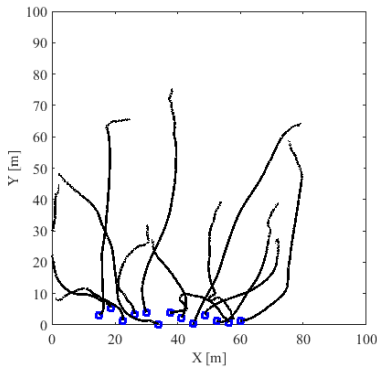


(a) Under unconstrained control law.

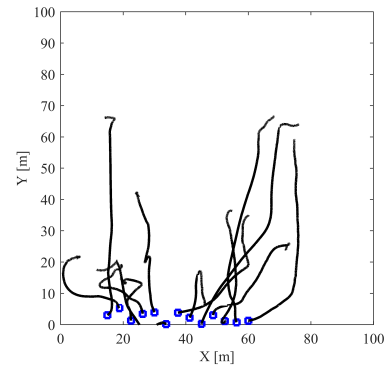


(b) Under constrained control law.

Figure 4.5: Final sensor network deployment configuration for covering a 2D region.



(a) Under unconstrained control law.



(b) Under constrained control law.

Figure 4.6: Sensor's trajectories history during optimization.

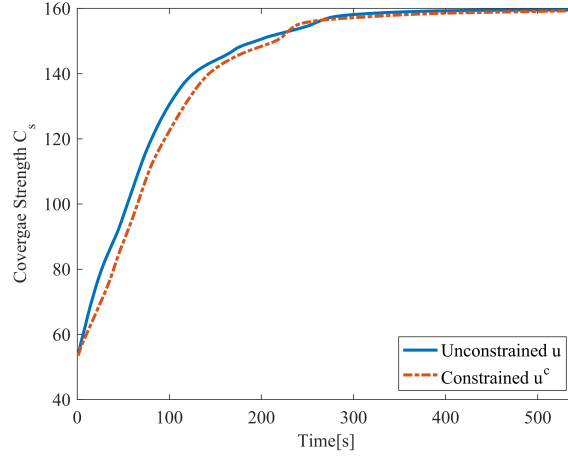
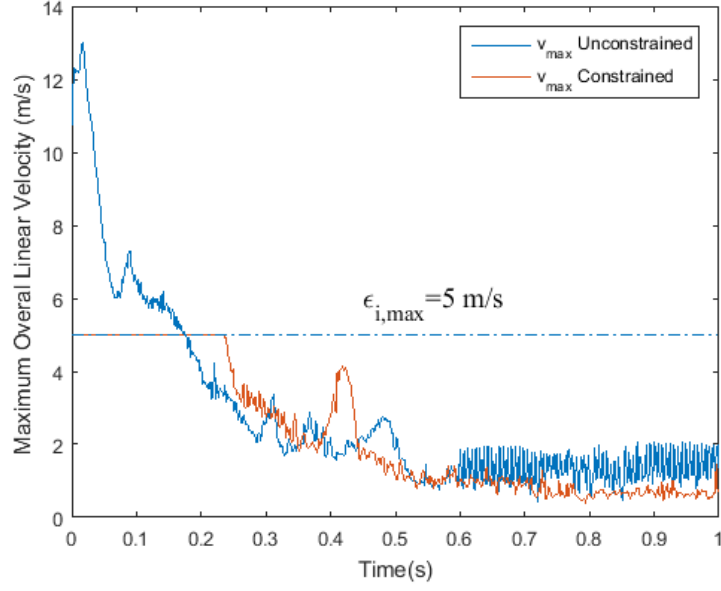


Figure 4.7: The overall coverage performance functions.

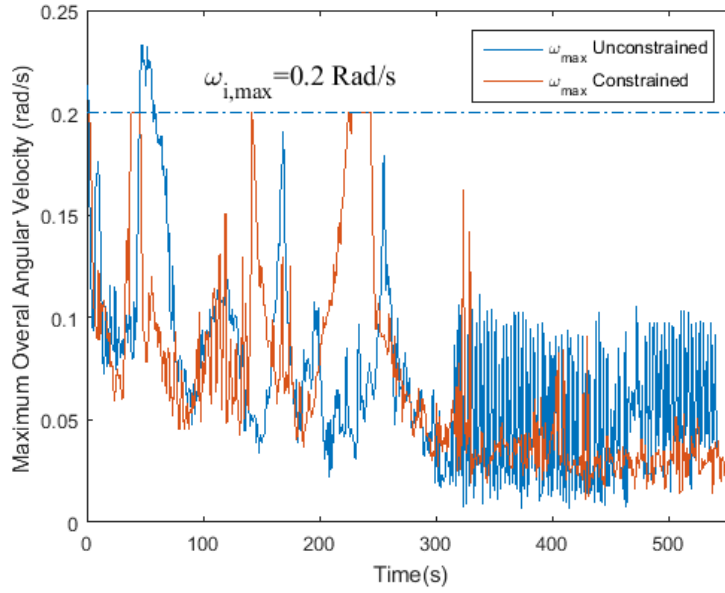
According to the Figures 4.7 and 4.6, It can be observed that using constrained control law, not only could cause the lower speed of convergence, but also different trajectory histories compare to the unconstrained situation. This means that the system under constrained control law, do not necessarily converge to the same critical point of \mathcal{H} for the unconstrained situation.

Figures 4.8(a) and (b) show the sensor's linear and angular velocity changes under both control laws. It is observed that the sensors do not exceed their predefined maximum velocity.

It is clear that the number of overlapped points is significantly decreased when the sensors spread out to achieve better coverage as shown in Figure 4.9.



(a)



(b)

Figure 4.8: Unconstrained sensor's velocities history.

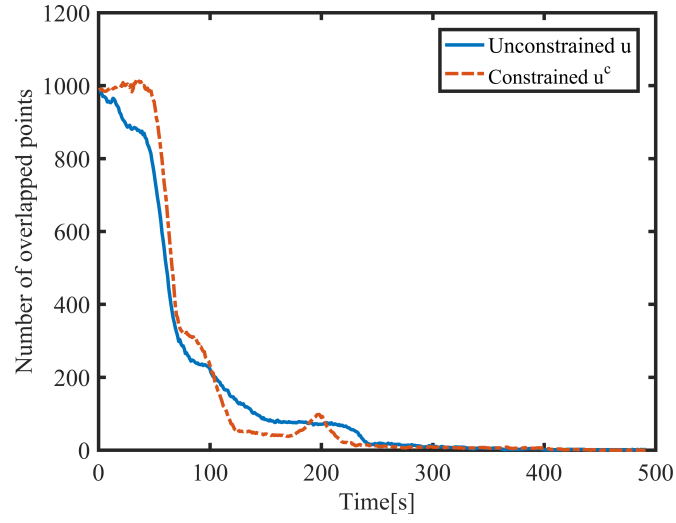


Figure 4.9: Number of points covered by more than one sensor.

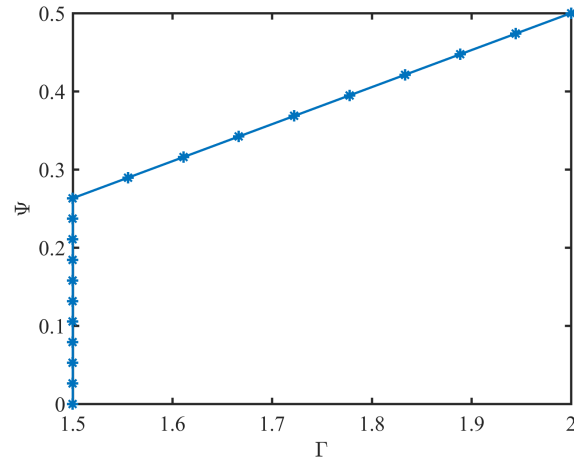
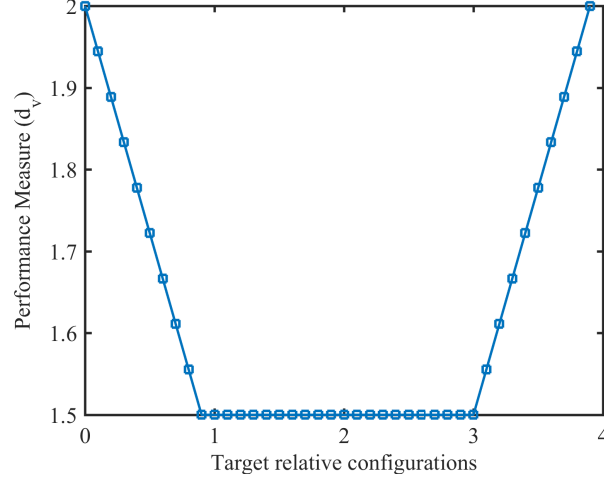


Figure 4.10: A set of different target configurations selected for sensitivity analysis.

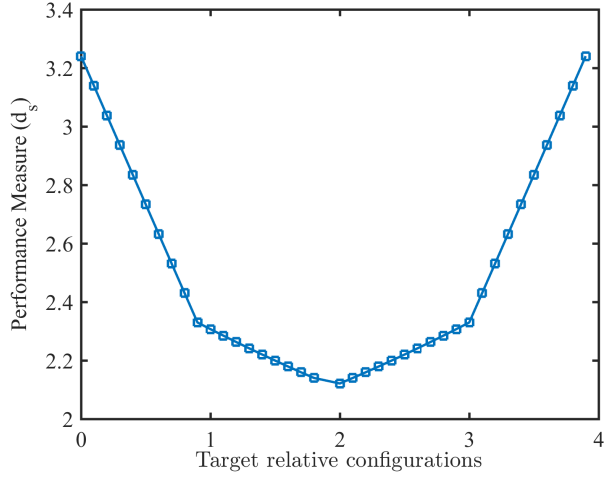
4.5.2 Camera Sensor Network Deployment

To evaluate the effectiveness of the introduced approach using Frobenius-norm Based Performance Measure, two simulations are conducted here.

Sensitivity analysis and configuration optimization



(a) Previous measure (d_v)



(b) Proposed measure (d_s)

Figure 4.11: The performance measure behavior for a set of target configurations.

A simulation is conducted based on a comparison between developed measure and the one (visual distance) proposed by Zhang et al. [51]. In that work, the infinity norm based function (d_v) is used to construct the performance measure which was effective in optimization. However, it is important to note that changes in one component in the array of the proposed measure (visual distance) will not be realized unless it is the maximum value component of the array. This will result in the occurrence of multiple local optima in some situation. To make it more clear, following simulation is conducted.

A simple scene having a field sensor and a target point with a set of 20 target configurations defined in sensor coordinate (Figure 4.10) such that has a global minimum point the configuration corresponds to $(\Gamma, \Psi) = (1.5, 0)$. The simulation results of the

Table 4.1: Simulation comparison of Zhang et al. [51] and the proposed measure for optimization of camera sensor network deployment.

Methods	Covered triangles / ratio	Resolution	Blur	View angle
Zhang et al. [51] (d_v)	347/98%	0.08	0.10	16.91
Proposed measure (d_s)	352/100%	0.08	0.09	10.32

comparison between performance measure of two approaches are depicted in Figure 4.11. As it can be seen from this figure, the infinity norm measure (d_v) has a constant value of $d_v = 1.56$ for a configuration within the set. This shows multiple local optimum and there is no guarantee achieving of the global optimum of the configuration's sets. In another hand, this configuration can be realized by the proposed measure (d_s). Thus, the infinity norm (d_v) based measure is "unaware" of these changes, whereas the proposed measure (in Section 3.3) can detect them. Having these results in hand, it is a better measure for optimization of sensor network deployment.

Camera Sensor Network Deployment

With a 3D representation of a terrain's surface, a simulation is conducted for the optimization of camera sensor network deployment in an area coverage task to validate the proposed approach. Furthermore, a comparison is carried out between the measure proposed here and the one developed by Zhang et al. [51]. The sensor and task model are selected from [41] in which the maximum blur circle, resolutions and view angle allowed are selected as $1.0mm$, $2.0mm$ and 45° , respectively.

The sensing region of the camera sensor is a frustum (truncated pyramid). The detail of geometric model construction for camera sensor is not provided here as it has a similar approach to flash LiDAR presented in Section 6.2.3. A network of $n = 12$ cameras is placed in a random initial configuration (Figure 4.12).

The comparison between the number of covered triangles is depicted in Figure 4.13. Despite Zhang et al. [51] method, the number of covered triangles are increased more rapidly and reach 100% coverage of triangles in 200s duration by the proposed approach.

The final sensor network deployment for both approaches are illustrated in Figure 4.14(a) and Figure 4.14(b).

Table 4.1, demonstrate the quantitative comparative results of two approaches. The proposed approach proves to have more promising results as it provides better coverage ratio, blur, and view angle. The main reason could be the existence of multiple local minima in the measure utilized by Zhang et al. [51] as explained in Section 3.3.

Figure 4.15 shows the Voronoi partitioning representation for the final sensor network deployment where each color belongs to one camera and uncovered triangles have black color. It is shown that some triangles have black color which means we have uncovered triangles.

4.6 Conclusion

This chapter has presented a systematic framework for modeling and optimization of field sensor network deployment through introducing a gradient based control law. It is shown that an optimal deployment of the field sensor networks is achieved, which prove the effectiveness of the proposed measures and deployment methodology.

Although the infinity norm-based performance measure has the advantage of both simplicity and proven performance, it has multiple local minimum issue, and it cannot provide the coverage strength variations of the target within the sensing region of the

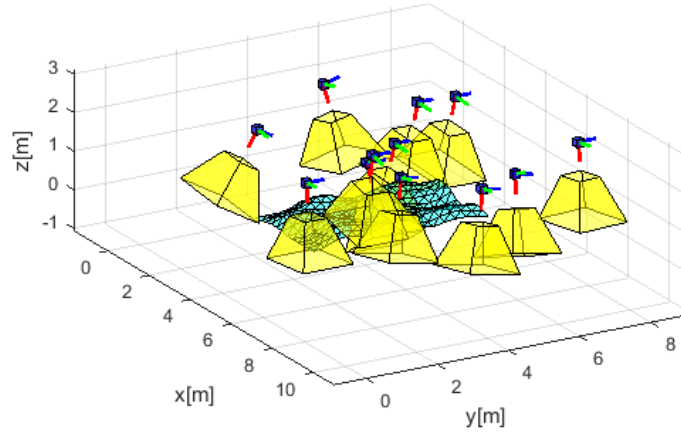


Figure 4.12: Initial configuration of camera sensor network which is randomly deployed in 3D space.

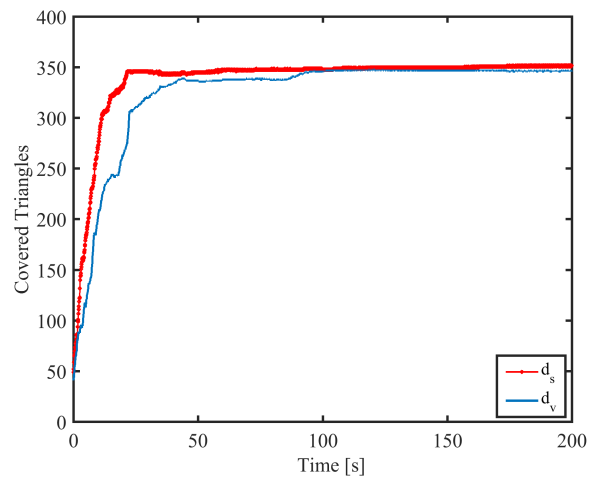
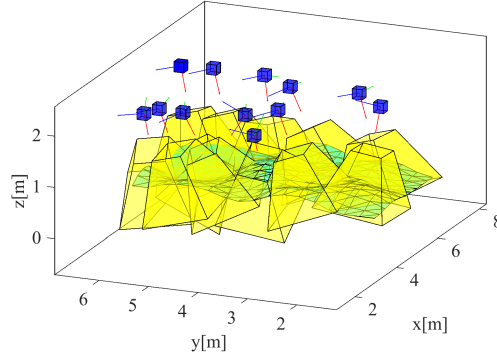
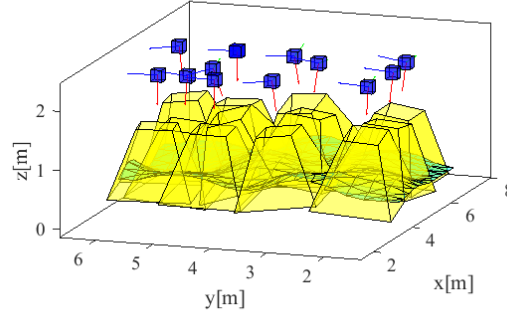


Figure 4.13: Number of covered triangles by camera sensor network during optimization.



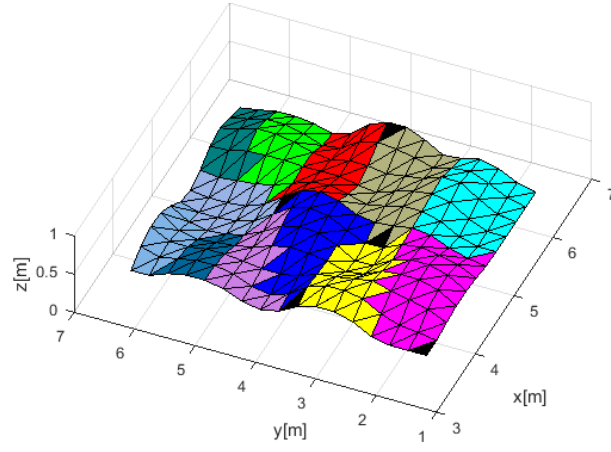
(a) Previous measure (d_v)



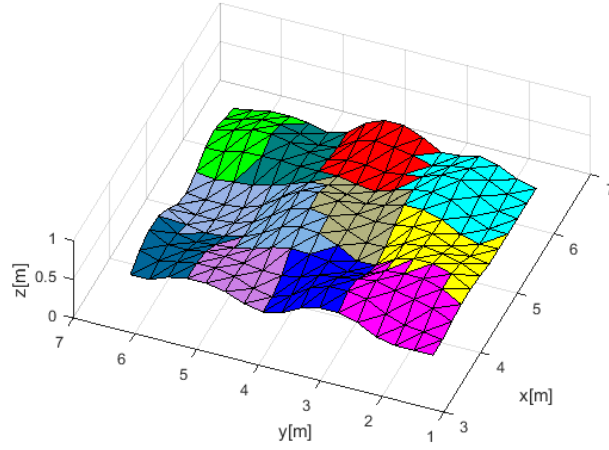
(b) Proposed measure (d_s)

Figure 4.14: Final camera sensor network deployment configuration.

sensor. Therefore, the Frobenius-norm based performance measure has been selected to construct the coverage model, and to optimize the LiDAR sensor network deployment in Part II of this dissertation. This coverage model not only utilizes the sensor exact geometric model but also overcomes the multiple local optima that exist in the performance measure proposed by Zhang et al. [51] which make it an effective approach for modeling the field sensor coverage.



(a) Previous measure (d_v)



(b) Proposed measure (d_s)

Figure 4.15: Target area partitioning based on different measures for final sensor network deployment.

Part II

Application to LiDAR sensor

LiDAR Sensor Principles

Whoever acquires knowledge but does not practice it is as one who ploughs but does not sow.

Saadi Shirazi (1210-1291)

5.1 Introduction

The LiDAR, which stands for Light Detection and Ranging, is an active remote-sensing system. It utilizes laser pulse to measure the distance to the objects. It is an active remote-sensing system which determines the distance to a target surface by measuring the flight time of the laser pulses transmitted to and reflected from the target surfaces (Figure 5.1). According to the scanning mechanism of LiDAR sensors, they can be categorized into two groups of mechanical and solid-state LiDARs. While the former is based on the mechanism of either mirror/prism rotating or scanner rotating (Figure 5.2(a)), the latter is either optical phase array or flash LiDAR (Figure 5.2(b)).

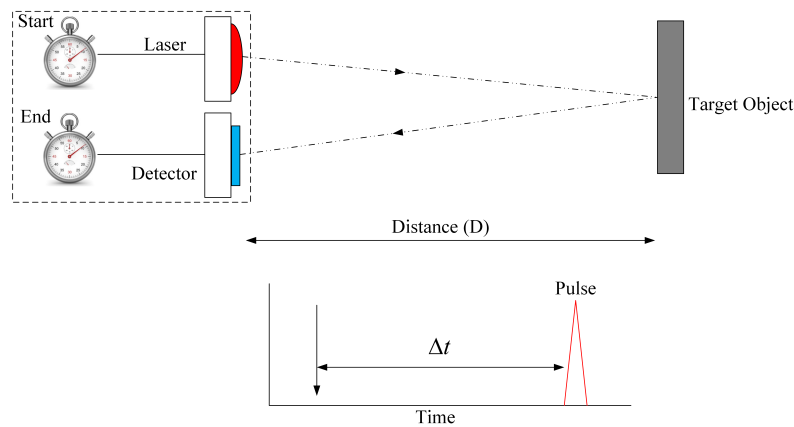


Figure 5.1: The principle of LiDAR sensor sensing method.

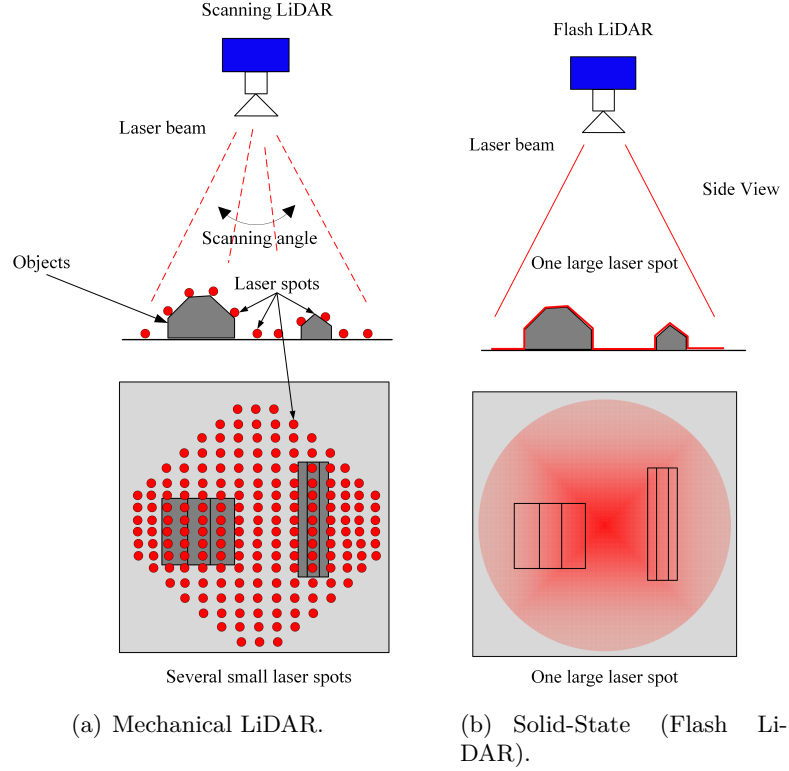


Figure 5.2: Schematic presentation of LiDAR sensors.

5.2 Solid-state (Flash) LiDAR

5.2.1 Operating Principle

In general, emitter, receiver, and optics are the main components of the flash LiDAR sensors. In the emitter, a laser diode shot a single short pulse usually from 5 to 10ns with a wavelength of 905nm to 1550nm. The flashlight illuminates with high-intensity energy over the target area. Then, the reflected pulse is collected by the receiver optics and focused on the detector panel. The Focal Plane Array (FPA) receiver module is extensively used in flash LiDAR design. Whereas the camera sensors utilize the passive light source, and the receivers are often charged-coupled devices (CCD).

5.2.2 Measurement Principle

The general measurement principles of the flash LiDAR are listed and explained as follows.

1) Field of View (FOV)

The flash LiDAR usually illuminate a pulsed laser beam with relatively wide divergence angle to cover the target area. In the absence of occlusion, the visibility of a point feature depends on whether it is within the FOV of the flash LiDAR sensor or not. Its FOV is defined based on the intersection of emitter and receiver FOV. Although an increase in FOV provides better coverage, the size of FOV is limited by the photo-detector sensitivity of receiver and eye safety requirements.

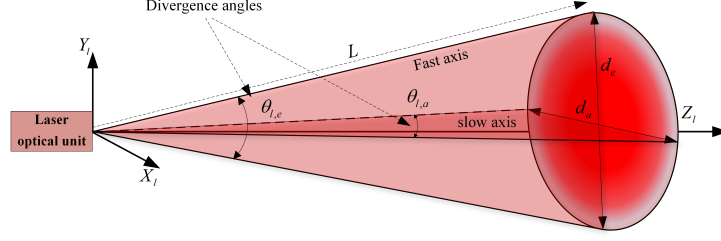


Figure 5.3: Schematic diagram of the laser emission FOV geometry.

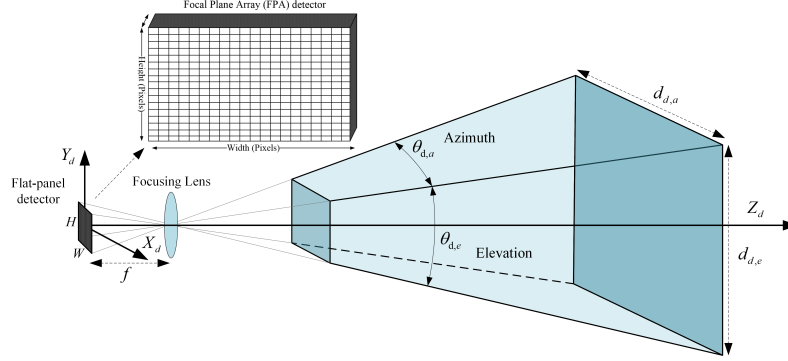


Figure 5.4: Schematic diagram of the receiver FOV geometry.

Emitter FOV. In general, the beam divergence is considered as the FOV of the emitter which is adjustable along horizontal and vertical axis (also termed slow and fast axis) using laser optical unit based on task requirements. Since the beam divergence angles are not necessarily equal in horizontal and vertical axis, the output beam has an elliptical cone shape as shown in Figure 5.3. Thus, the emitter FOV is specified by laser beam divergence angles $\theta_{l,e}$ and $\theta_{l,a}$, as

$$\theta_{l,e} = \tan^{-1} \left(\frac{d_e}{2L} \right) \quad (5.1)$$

where d_e is the length of laser beam footprint along the Y-axis and L is the distance from the emitter center in direction of the Z-axis

$$\theta_{l,a} = \tan^{-1} \left(\frac{d_a}{2L} \right) \quad (5.2)$$

where d_a is the length of laser beam footprint along the X-axis

Receiver FOV. The dimension of the detector and receiving lens specify the receiver FOV. It is constructed from elevation $\theta_{d,e}$ and azimuth $\theta_{d,a}$ angles (Figure 5.4), defined as

$$\theta_{d,e} = \tan^{-1} \left(\frac{H}{2f} \right) \quad (5.3)$$

where f is the focal length of the receiving lens, and H is the vertical number of the pixels.

$$\theta_{d,a} = \tan^{-1} \left(\frac{W}{2f} \right) \quad (5.4)$$

where W is the horizontal number of the pixels.

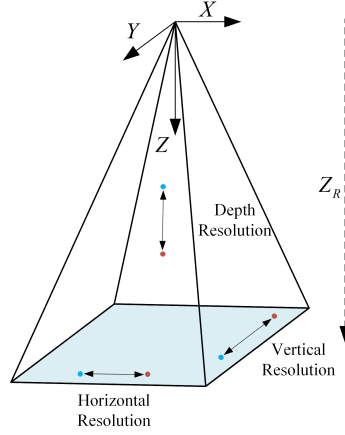


Figure 5.5: Description of flash LiDAR Horizontal, Vertical and Depth resolutions.

2) Resolution

The ability of an imaging system to distinguish between two objects located close to each other in space is called spatial resolution, which is measured in the unit of distance. The higher spatial resolution implies that smaller distances between objects can be distinguished.

Spatial resolution can be divided into two categories: axial (range or depth) resolution which is defined in the detector normal direction (Z-axis) and lateral (cross-range) resolution, that is the defined in the direction perpendicular to the Z-axis. Lateral resolution is commonly further sub-categorized into horizontal and vertical resolutions.

The flash LiDARs are usually constructed from a 2D detector array, called Focal Plane Array (FPA) detector, which captures 3D and intensity data through the illumination of a laser pulse over the entire scene. In fact, each pixel will enable the detector to measure the travel time of each laser pulse independently. Due to structural similarity of FPA with the 2D camera detector, the lateral resolutions are similar to the resolution of camera sensor, and can be defined as the number of units of length that are represented by a pixel [105]. Thus, the resolution is determined based on the receiver optics and the pixel number of the array.

Horizontal resolution (m/pixel). It is defined as the resolution perpendicular to the direction of the Z-axis along X (Figure 5.5), given by

$$R_H = \frac{2Z_R \tan\left(\frac{\theta_{d,a}}{2}\right)}{W} \quad (5.5)$$

where $\theta_{d,a}$ is the azimuth angle, Z_R is the depth of imaging, and W is detector width (horizontal number of the pixels).

Vertical resolution (m/pixel). It is defined as the resolution perpendicular to the direction of Z-axis along Y, given by

$$R_V = \frac{2Z_R \tan\left(\frac{\theta_{d,e}}{2}\right)}{H} \quad (5.6)$$

where $\theta_{d,e}$ is the elevation angle and H is the detector height (vertical number of pixels). Therefore, detector lateral resolution is defined by considering the worst case resolution

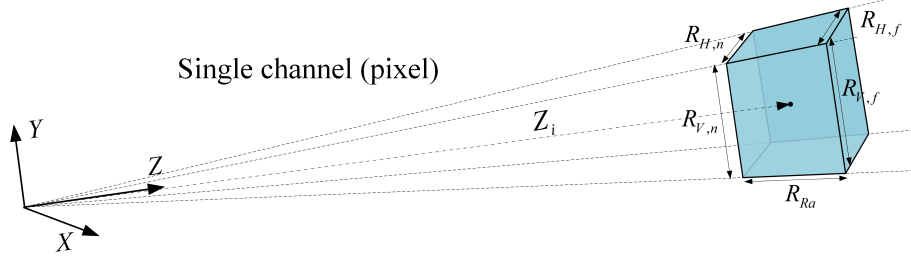


Figure 5.6: Schematic representation of flash LiDAR resolution cell.

as

$$R_L = \max(R_H, R_V) \quad (5.7)$$

In other words, detector lateral resolution is affected by detector dimension and the depth of imaging.

Range (Depth) resolution(m). The ability of flash LiDAR to distinguish two points that are separated along the single channel (pixel) on different azimuth or elevation angles. It can be defined by

$$R_{Ra} = \frac{cT_w}{2} = \frac{c\tau}{2} \quad (5.8)$$

where $T_w(s)$ is pulse width, $c = 3 \times 10^8 \text{m/s}$ is the speed of light and τ is the resolution of the timer for recording pulses. That is to say, the shorter pulse width, the higher range resolution will be. It is affected by pulse width, target type, target size and the efficiency of the receiver. In this study, only the effect of the pulse width is considered.

Resolution cell. The resolution cell (sampling volume) at depth Z_i is a volume of space which is constructed from sensor axial and lateral resolutions depicted in Figure 5.6. This means that any two objects that are located inside the same resolution cell, are not distinguishable. This term is validated in the experimental section for the proposed flash LiDAR (VU8).

3) Range Accuracy

In general, range accuracy is the error between the result of a depth measurement and its true value. It is affected by many factors such as system temperature and calibration algorithm, background light, laser pulse power fluctuation, noise from the detector, and time resolution. In this study, only the impact of the time resolution is investigated. The resolution is the smallest increment of measure that a device can make. Since the accuracy of a system can never go beyond its resolution, it will specify an upper bound on the range accuracy. For example, to have a desired range accuracy of A_d , the range resolution should be $R_{Ra} \geq A_d$. Thus, the required time resolution (T_R) could be defined as,

$$T_R = \frac{2R_{Ra}}{c} \quad (5.9)$$

where c is the speed of light.

4) Detection Range

The detection range is a fundamental quantity measured by most of the remote sensors. It is calculated from the speed of light in the medium and round-trip travel time of an emitted pulse \mathbf{T}_R .

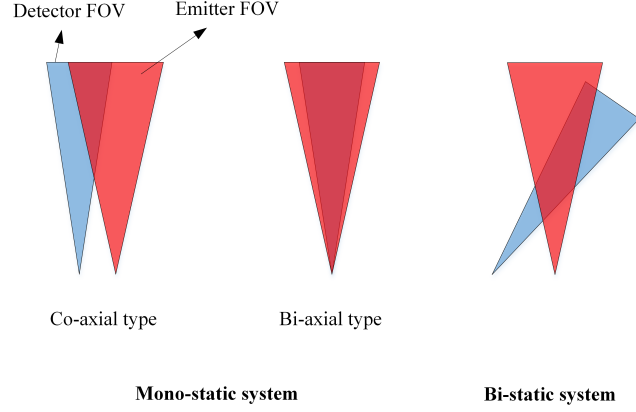


Figure 5.7: Relative configuration of emitter and receiver for different systems.

Minimum Detection Range. Generally, LiDAR sensors have a minimum detection range z_m (blind range) limitation. This means that closer objects might not be detected or sensor might deliver inaccurate values. Three most primary factors which affect the minimum detection range are listed as follows,

- (i) **Relative configuration of emitter and receiver.** The relative geometry of emitter and receiver may limit detection at short distances. LiDAR sensors are usually designed in either mono-static or bi-static systems (Figure 5.7) [106]. Clearly, for short-distance detection, bi-axial configuration is more appropriate. For Bi-static systems, the detection range is given by

$$z_{tr} + z_{re} = T_R \quad (5.10)$$

where z_{tr} and z_{re} are transmitted and received ranges, respectively. For mono-static systems,

$$z = \frac{cT_R}{2} \quad (5.11)$$

where $z = z_{tr} = z_{re}$. During transmission of the pulse, some of the light from the transmitter might scatter off the optical surface and reach the receiver. Thus, this needs to be removed from the collected data chain to allow detection of nearby objects.

- (ii) **Emitted pulse width.** The emitted pulse duration also has impact on the minimum range detection of the LiDAR sensor. Since the return pulses require to be distinguishable at the detector, they should be sufficiently separated. Therefore, a time interval equal to pulse duration is required for the detector before a new return can be handled. Therefore, according to (3.1), the minimum detection range is given by

$$Z_{pw} = \frac{cT_w}{2} \quad (5.12)$$

where T_w is pulse width and c is the speed of light in the free space. Thus, the shorter pulse width will result in lower the minimum detection range.

- (iii) **Detector saturation level.** Another factor affecting minimum detection range is detector saturation. The detector can be temporarily blinded by relatively strong pulses. Thus, the target should be far enough to avoid detector saturation effect.

Maximum Acceptable Range. The acceptable maximum detection range along sensor's z-axis (z_M) is obtained by

$$z_M = \min(Z_p, Z_n) \quad (5.13)$$

where Z_n and Z_p are the nominal and permissible detection range, respectively.

Nominal detection range (Z_n). The nominal maximum detection range of a LiDAR sensor is influenced by many factors. The most primary elements are listed as follows,

- (i) **Laser power.** The reflected beam energy needs to be sufficient to trigger the detector, as it is required to define some limiting threshold to eliminate the ambient light noise. This means that at far distances, some returns may be missed by the detector.
- (ii) **Object reflectivity effect.** The object reflectance property affects the nominal maximum detection range. A white surface usually has a better reflectance property than a darker surface. The reflectance of the object's material describes the relationship between the power of the reflected and incident laser pulse. The amount of the reflected pulse from the surface through the scanning probe is inversely proportional to the square of the surface distance. For instance, a surface with 90% reflectivity might be detected three times farther as compare to a 10% one.
- (iii) **Pulse-Repetition Frequency(PRF).** The pulse repetition frequency (τ_f) of a laser emitter is defined as the number of transmitted pulses per second. According to Equation (5.10), the longest distance it can achieve from a round trip of the pulse during one pulse-repetition period, is called maximum (unambiguous) range, and obtained by

$$Z_{pr} = \frac{cT_R}{2} \quad (5.14)$$

where $T_R = \frac{1}{\tau_f}$ and τ_f is pulse repetition frequency.

Although a high τ_f , short period between successive pulses, enhances resolution and range accuracy by providing more target samplings, it will limit the maximum range. In addition, there is a chance that an echo from a far target returns after emitter has sent another pulse. Thus, it might not be possible to determine whether the received pulse is the echo of the just transmitted pulse, or it is from preceding pulse. This situation is referred as range ambiguity [107] which means the range information is unreliable. Therefore, the emitter cannot send out a pulse until a time window has passed. This will limit the nominal maximum detection range.

- (iv) **Atmospheric visibility.** Another primary factor which influences the nominal maximum detection range is atmospheric visibility. It is determined by the distributions of aerosol particles, which can be in the form of liquid water or solid particles. Due to attenuation of the transmitted laser radiation as well as the backward reflected radiation in low visibility conditions, this factor might have a significant impact. One way to characterize atmospheric visibility effect is utilizing experimental-based models such as the one proposed by Horvath [108].

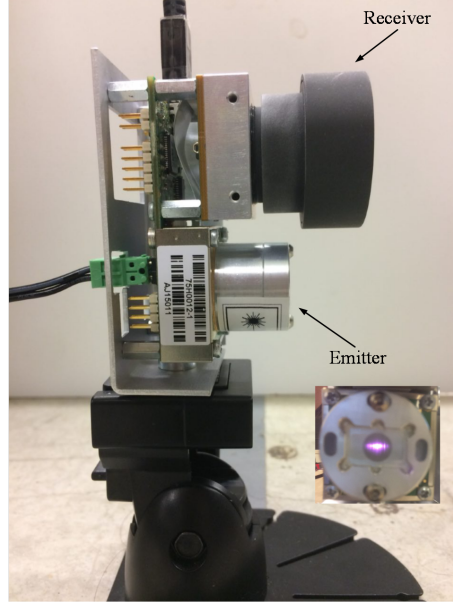


Figure 5.8: Flash LiDAR sensor ($VU8 - 100^\circ \times 3^\circ$) used for experimental validation.

Permissible detection range. According to the application required resolution (R_d), the permissible detection range Z_p will be specified based on the task desired lateral resolutions, as

$$Z_p = \min(Z_{R,W}, Z_{R,H}) \quad (5.15)$$

where

$$Z_{R,W} = \frac{R_d W}{2 \tan\left(\frac{\theta_{d,a}}{2}\right)} \quad (5.16)$$

$$Z_{R,H} = \frac{R_d H}{2 \tan\left(\frac{\theta_{d,e}}{2}\right)} \quad (5.17)$$

5.2.3 Experimental Validation

In this section, validation of the resolution cell is performed through verifying of horizontal, vertical and depth resolution. For this purpose, an experiment is set up to validate the resolutions obtained from theory.

The flash LiDAR sensor ($VU8 - 100^\circ \times 3^\circ$) with the accuracy of $\pm 10 \text{ cm}$, depicted in Figure 5.8 is selected for the experiment which currently is the only affordable flash LiDAR in the market. A box with the dimension of $15 \times 20 \times 60 \text{ cm}$ is selected as the target. The LiDAR specifications are listed in Table 5.1.

Table 5.1: LiDAR VU8 model specifications for experimental set up.

Parameters	Variable	Value
Pulse width	T_w	20 ns
Azimuth angle	$\theta_{d,a}$	$92^\circ \pm 4^\circ$
Elevation angle	$\theta_{d,e}$	$3^\circ \pm 0.6^\circ$
Detector width	W	8 channels
Detector height	H	1 channel

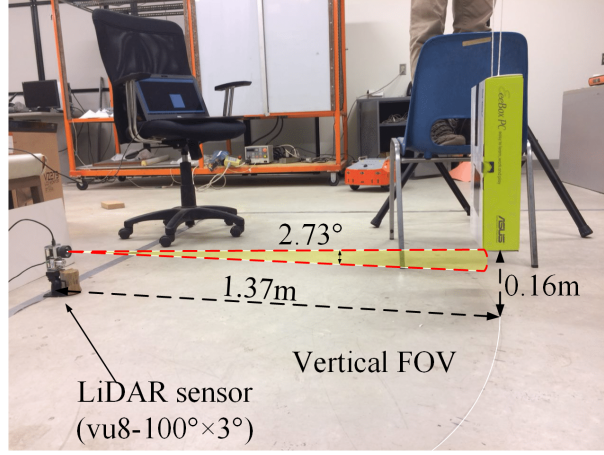


Figure 5.9: Experimental set up for vertical resolution validation.

Vertical Resolution Validation

Since the selected LiDAR has 8 channels that are placed horizontally, the number of vertical pixels $H = 1$ and vertical FOV (with tolerance) is $3^\circ \pm 0.6^\circ$. Thus, the vertical resolution is determined as $R_{V,T} = 2(1.37) \tan\left(\frac{3^\circ}{2}\right) = 0.072m/pixel$. To verify the vertical resolution, the LiDAR sensor is positioned above the ground to detect the boundary of the channel, as depicted in Figure 5.9. The elevation angle of the channel is obtained as 2.7° . Thus, the Vertical resolution is determined by $R_{V,E} = 2(1.37) \tan\left(\frac{2.7^\circ}{2}\right) = 0.065 m/pixel$.

Horizontal Resolution Validation

The number of pixels $W = 8$ and horizontal FOV (with tolerance) is $92^\circ \pm 4^\circ$. The horizontal resolution of flash LiDAR at distance $Z_R = 1.37m/pixel$ is obtained as $R_{H,T} = \frac{2(1.37) \tan\left(\frac{90^\circ}{2}\right)}{8} = 0.3425m/pixel$. To verify the horizontal resolution, the LiDAR sensor is placed on the ground and using a target box, all its channels are determined as illustrated in the Figure 5.10. While there are some overlaps between channels, the average angle of each channel is obtained as 11.6° . Thus, the horizontal resolution is determined as $R_{H,E} = 2(1.37) \tan\left(\frac{11.6^\circ}{2}\right) = 0.28m$.

Range Resolution Validation

The laser pulse width is $T_w = 20ns$, according to Equation (5.8), the depth resolution ($R_{Ra,T}$) for flash LiDAR is calculated as $R_{Ra,T} = \frac{(3 \times 10^8) \times (20 \times 10^{-9})}{2} = 3m$. To verify the depth resolution, two target boxes were placed on channel 4 (pixel) having different azimuth angles as depicted in Figure 5.11 and Figure 5.12. The minimum detectable distance between the boxes is obtained as $R_{Ra,E} = 3.39m$.

While the experiment implementation provided for different resolutions incurred in some error, the result of resolution validations observation is listed in Table 5.2.

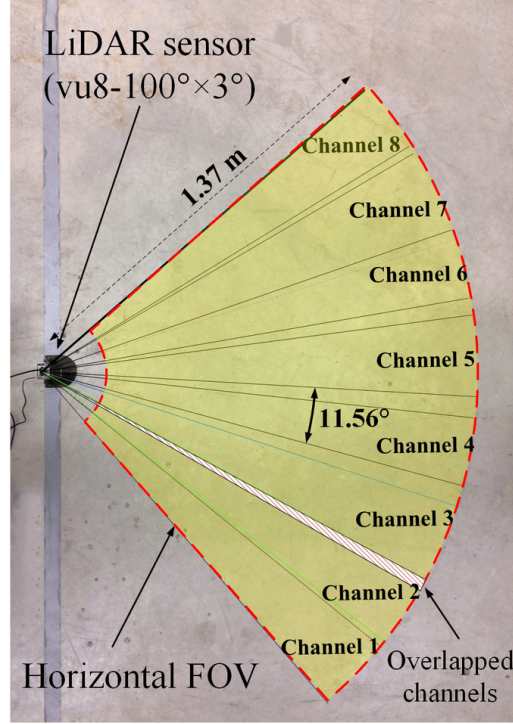


Figure 5.10: Experimental set up for horizontal resolution validation.

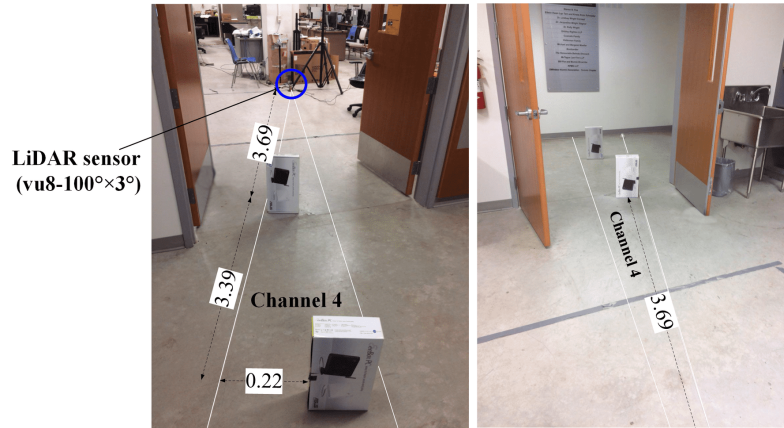


Figure 5.11: Experimental set up for depth resolution validation.

Table 5.2: Comparison of experimental and theoretical results for Flash LiDAR sensor resolutions.

Parameters	Theory	Experiment	Error (%)
Horizontal Resolution ($m/pixel$)	0.34	0.28	18
Vertical Resolution ($m/pixel$)	0.072	0.065	10
Range Resolution (m)	3.0	3.39	13

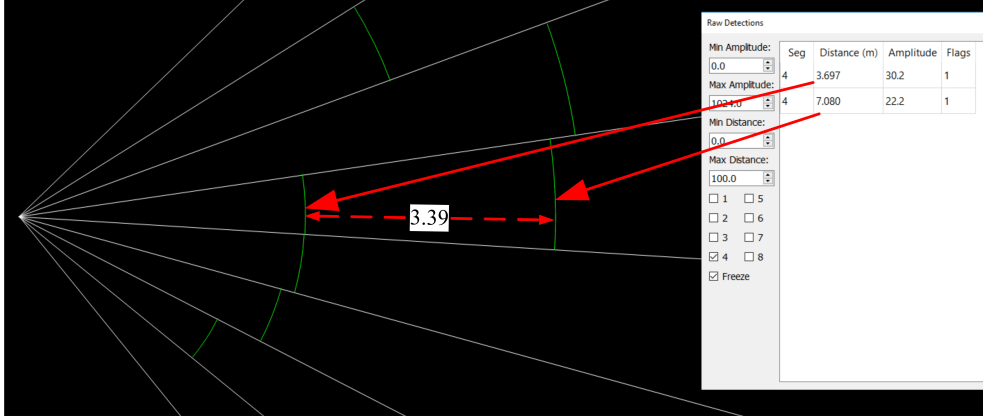


Figure 5.12: Screenshot from Leddar VU8 software for depth resolution validation.

5.3 Mechanical (Prism rotating) LiDAR

5.3.1 Operating Principle

The mechanical LiDAR sensor has three main parts: the light source, detector, and scanning mechanism. The laser emits light that has an elliptical cone shape which is collimated by emitter lens placed at the focal distance of the laser diode to generate an appropriate laser beam. The echoes from the target surface will be focused on the detector to eventually measure the distance of the target surface to the detector. Rather than using a FPA as a detector to detect the return laser pulses such as in the case of flash LiDAR, in these sensors usually, one detector is used to acquire data. Different scanning mechanisms have been widely used in mechanical LiDARs such as oscillating mirror, rotating polygon, palmer scanner (nutating mirror), Risley prism scanner [109], [110]. In contrast to flash LiDAR, it typically enables a wider scanning area up to 360° azimuth angle.

5.3.2 Measurement Principle

In this dissertation, a mechanical scanning LiDAR having prism rotating mechanism is selected. In following the measurement principles are listed and explained.

1) Field of View (FOV)

The FOV is defined as the observable region of the sensor determined by analyzing scanning mechanism. Since the selected mechanical LiDAR is OPAL-120 (conical), the Risley prisms scanner is considered as the scanning mechanism in this thesis. For the Risley-prism-based beam steering systems, the geometry and material properties of the prisms determine the sensor FOV (θ') which typically has a range from 15° to 120° [111].

2) Resolution

The ability of mechanical LiDAR to distinguish two points that are separated along a single beam at different azimuth angles is called range resolution (R_a). For these types of LiDAR sensors only range resolution is considered. This resolution relies upon the emitter pulse width (T_w), object type and size as well as the efficiency of the LiDAR receiver. However, among those mentioned parameters, the pulse width plays a key role

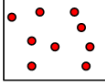
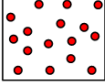
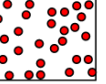
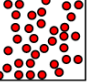
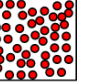
					
Point density (<i>pts / m²</i>)	0.5-1	1-2	2-5	5-10	10+
Application	• Basic surface model	• Flood modelling	• Multi-purpose data sets	• Basic 3D models	• Detailed 3D city models

Figure 5.13: Point density requirement example for different applications [113].

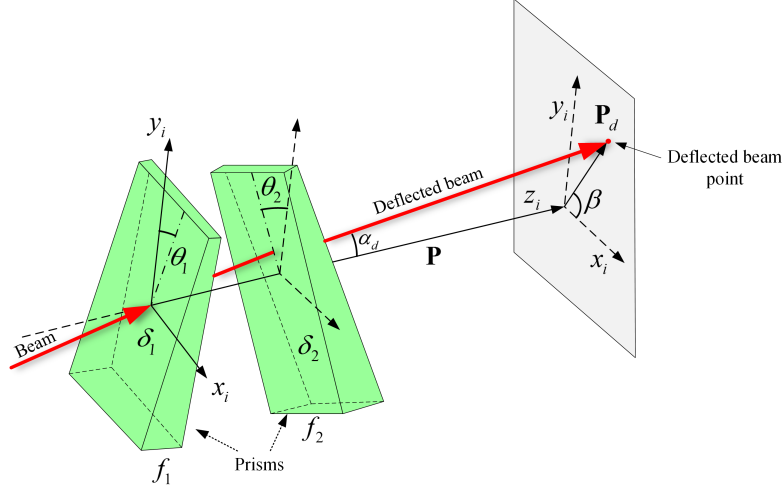


Figure 5.14: Schematic diagram of Risley prism pair steering system.

in determining the range resolution[112], given by

$$R_a = \frac{cT_w}{2} \quad (5.18)$$

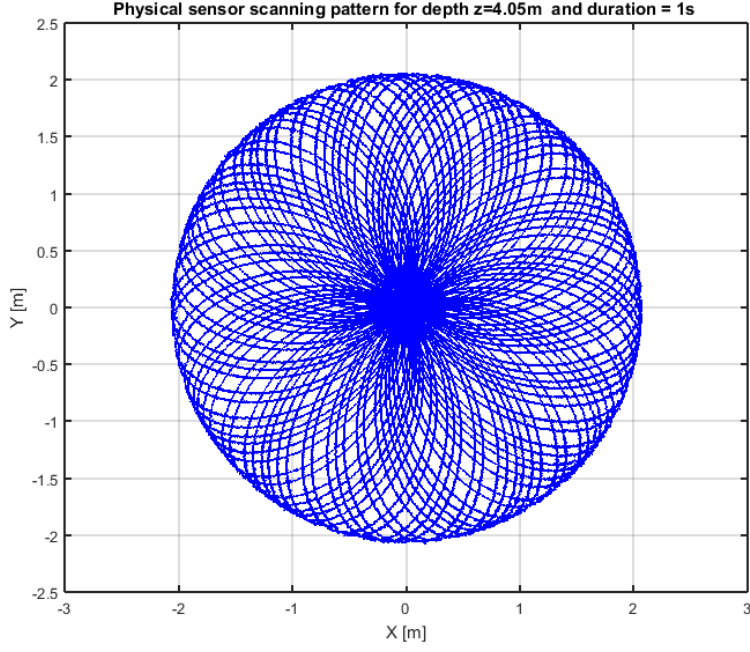
3) Point Density

The data obtained from the mechanical LiDAR is usually a point cloud. The most significant aspect of the point cloud is clearly its point density (ρ_p). It is the number of points defined in unit of area, given by

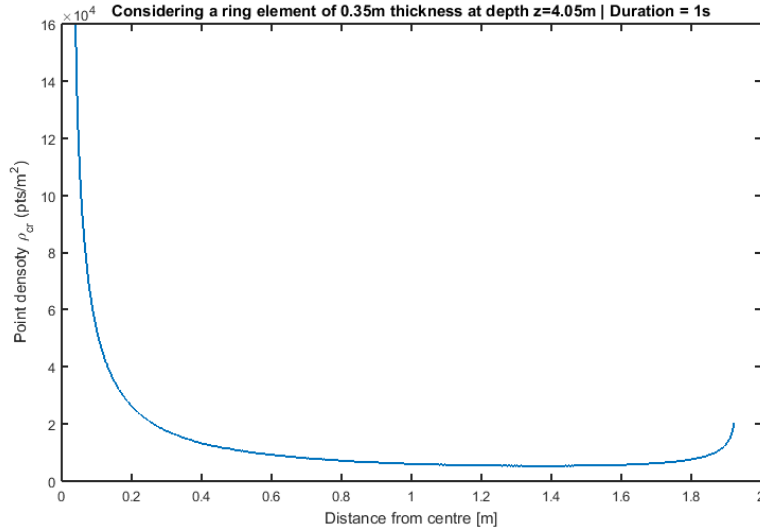
$$\rho_p = \frac{N_p}{A_p} \quad (5.19)$$

where N_p (*pts*) is the number of points and A_p is the area (m^2). The higher the scanning point density, the more expensive LiDAR sensor will be. This is because the point density is the dominant factor in overall cost of the sensor. The common point density requirements based on different applications are listed in Figure 5.13.

A mechanical LiDAR sensor generally provides a collection of measurements within sensor's FOV through sweeping the beam direction. In case of OPAL-120, the Risley-prism-based beam steering system is implemented for data scanning as it is depicted in Figure 5.14. This is a system which can continuously scan the beam over a wide angular range and depends on the geometry and material properties of the Risley prism pair, which is performed through mechanical rotation of two wedge prisms. The coordinate of the deflected beam point $\mathbf{P}_d = [x_d, y_d]$ can be determined through a first-order



(a) Scanning pattern.



(b) Point density distribution.

Figure 5.15: OPAL-120 (conical) sensor scanning pattern for duration of 1s with 200K Hz PRF).

approximation [114], given by

$$x_d = P([\delta_1 \cos(2\pi f_1 t + \theta_1)] + [\delta_2 \cos(\pm 2\pi f_2 t + \theta_2)]) \quad (5.20)$$

$$y_d = P([\delta_1 \sin(2\pi f_1 t + \theta_1)] + [\delta_2 \sin(\pm 2\pi f_2 t + \theta_2)]) \quad (5.21)$$

where P is the depth along z -axis, f_1, f_2 denote the rotatory frequency of the two prisms, δ_1, δ_2 are deviation angle of two prisms, θ_1, θ_2 are the initial rotatory angles of prisms. The positive or negative signs are considered when two prisms rotate in the same or opposite direction, respectively.

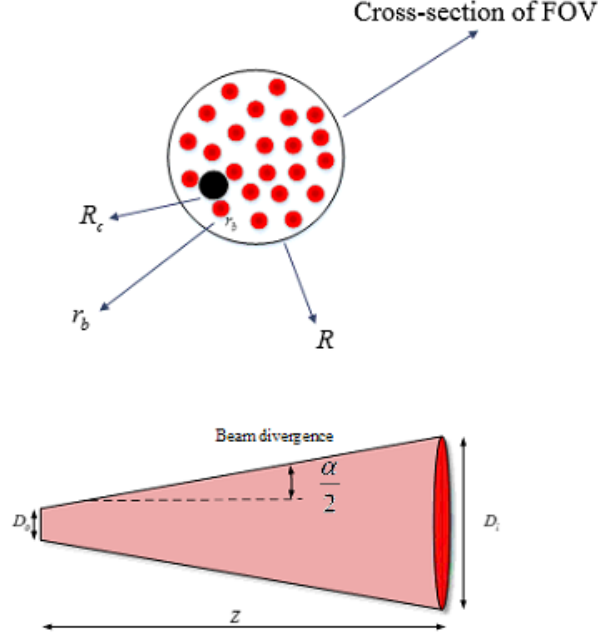


Figure 5.16: Illustration of largest non-detectable circle within LiDAR FOV cross-section.

Cross-range average (CRA) point density

Based on (5.19), the CRA point density is defined within LiDAR FOV cross-section as

$$\rho_{cr}(z) = \frac{\tau_f t_s}{A_{cr}(z)} \quad (5.22)$$

where t_s is the scanning duration, $A_{cr}(z)$ is cross-section area defined as

$$A_{cr}(z) = \pi \left(z \tan \left(\frac{\theta'}{2} \right) \right)^2 \quad (5.23)$$

The scanning pattern of physical sensor obtained for $t = 1s$ duration at the range $z = 4.05m$ is depicted in Figure 5.15 where the ring shape elements are considered to calculate the cross-range (CR) point density from the center to the boundary of the sensor scanning pattern.

Definition 5.1 (Maximum undetectable circle).

The size of the largest undetectable circle with radius R_c , which can be fitted among laser footprints along FOV cross-section is termed maximum undetectable circle (MUC)(Figure 5.16).

Although the location of MUC might not be unique, any circle greater than this size will be detectable with at least one laser footprint, and it is affected by laser footprint radius (r_b) and depth of imaging (Z).

According to Figure 5.16, the laser footprint (r_b) is defined as

$$r_b = \frac{1}{2} D_l = \frac{1}{2} (D_o + L \tan(\alpha)) \quad (5.24)$$

where D_l and D_o are laser beam diameter at two different depths and α is beam divergence.

Target detection. One important question in the study of the target detection problems is the performance of the sensor in the detection of high-speed targets, and whether the sensor can detect the presence of a target at a given time or distance from the sensor. To answer these questions, analyzing the sensor point density is required.

The CRA point density ρ_{cr} is not a reliable indicator for evaluation of the target point density when the scanning pattern distribution is not uniform (such as OPAL-120, which has a non-overlapped scanning pattern). Thus, in such cases, the target point density at a specific range within sensor FOV can be defined by considering the worst-case scenario. This means finding a location within the FOV cross section in which the target will have the minimum point density. It can be achieved by placing the target at the point p_c (center of MUC). To investigate sensor performance in target detection problem, the following example task is proposed.

Definition 5.2 (Target effective area).

The area defined by the projection of the target on the plane perpendicular to the z-axis is defined as target effective area.

Target sensing regions. Let consider a moving target approaching the LiDAR sensor (Figure 5.17). The sensor FOV can be divided into three different regions based on the size and the minimum point density requirement of the target, as follows:

1. *Undetectable region.* It is a sub-region of the sensor FOV calculated from Z_p to z_n , where the target cannot be detected according to the minimum point density requirement.
2. *Detectable region.* It is a sub-region of the sensor FOV calculated from l_{safe} to Z_p , where the target can be detected according to the minimum point density requirement.
3. *Safe region.* The safe region is a sub-region of the sensor FOV defined from the sensor minimum detection range to l_{safe} , where the presence of the target should be determined before it enters this region.

Let assume a moving target with the known effective area has a circular shape or can be approximated by a circle, is moving toward the sensor (within FOV). We need to know how fast the target can move but still can be detected by the sensor before entering the predefined safe distance (l_{safe}) from the sensor. Figure 5.17 illustrates LiDAR sensor operation in the context of a moving target detection.

Maximum detectable speed. The presence of the target can be detected with at most one time frame (t_{fr}) after it entered the detectable region. This is because maximum CRA takes place at the end of the frame time. Thus, by defining the safe distance l_{safe} , the maximum speed of target that still can be detected by sensor, is given by

$$V_{max} = \frac{Z_p - l_{safe}}{t_{fr}} \quad (5.25)$$

where Z_p depends on the target size and type. In other words, for targets moving at slower speed (by considering frame Rate), the detection within the detectable region is guaranteed while if it moves faster, there is a chance to miss detection of the target.

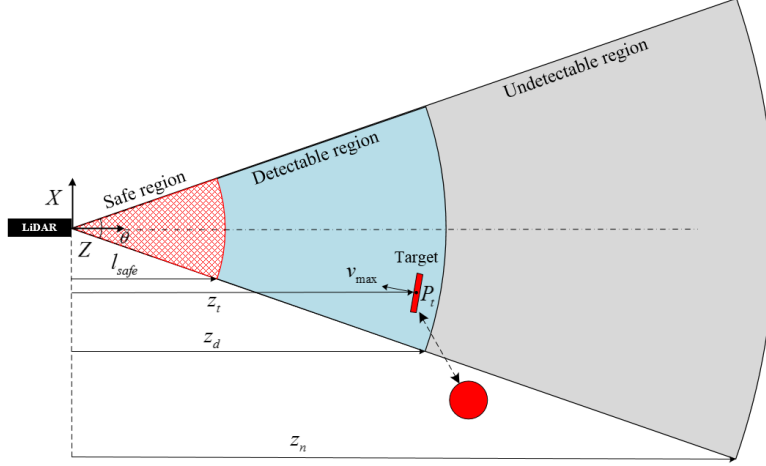


Figure 5.17: Illustration of different target sensing regions for the target detection application.

4) Detection Range

The result of detection range for flash LiDAR (Section 5.2.2) can be applied to mechanical LiDAR. The only difference is the way the permissible detection range is determined. In contrast to flash LiDAR which depends on lateral resolution, the scanner point density (5.22) determines the permissible detection range (Z_p) as

$$Z_p = \frac{1}{\tan\left(\frac{\theta'}{2}\right)} \sqrt{\frac{\tau_f t_s}{\rho_{cr} \pi}} \quad (5.26)$$

5.3.3 Simulation and Experimental Validation

In this section, we present some simulation and experimental results for point density evaluation of the LiDAR sensor model through analysis of scanning pattern. Furthermore, we analyze the scanning pattern for the cases of stationary sensor deployment. In the following, it is assumed that the LiDAR is operated in a good visibility condition, and the target has a high-reflectivity at least 90%. The specification of the selected sensor is listed in Table 5.3.

Table 5.3: The selected LiDAR (OPAL-120) specifications for simulation and experiment.

Parameters	Variable	Value
Frame rate	t_{fr}	2 Hz
Pulse Repetition Frequency (PRF)	τ_f	200 kHz
Inner prism rotatory frequency	f_1	72.0 Hz
Outer prism rotatory frequency	f_2	21.37 Hz
FOV (conical)	θ'	90°

We have set up an experiment to perform the stationary scanning as shown in Figure 5.18. The scanning data was gathered by placing the OPAL-120 (conical) sensor $d = 4.05m$ away from the wall.

The comparison between experimental and approximated (simulated) scanning patterns within one time frame ($t_{fr} = 0.5s$) is shown in Figure 5.19(a). According to Figure

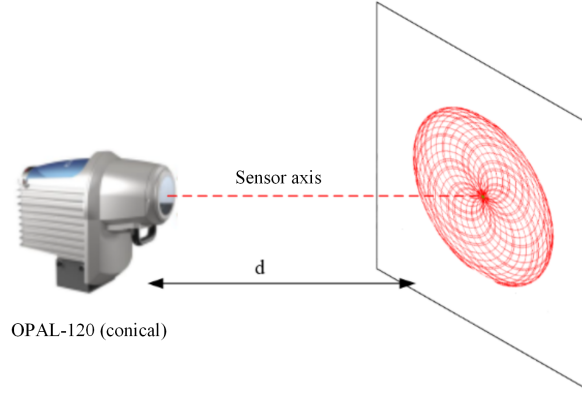


Figure 5.18: The LiDAR sensor (OPAL-120) is placed such that the sensor axis is vertical to the wall for experimental setup.

5.19(b), the maximum error does not exceed $17cm$. This error can further be improved by implementation of a higher order approximation model. For OPAL-120 (conical) LiDAR sensor, the FOV has the following relation to the scanning depth $\theta' = 2\tan^{-1}\left(\frac{R_M}{z_M}\right)$, where R_M is scanning radius at depth z_M . Thus, having the depth of scanning pattern, we have obtained the physical sensor FOV using Figure 5.19(b) as 108° .

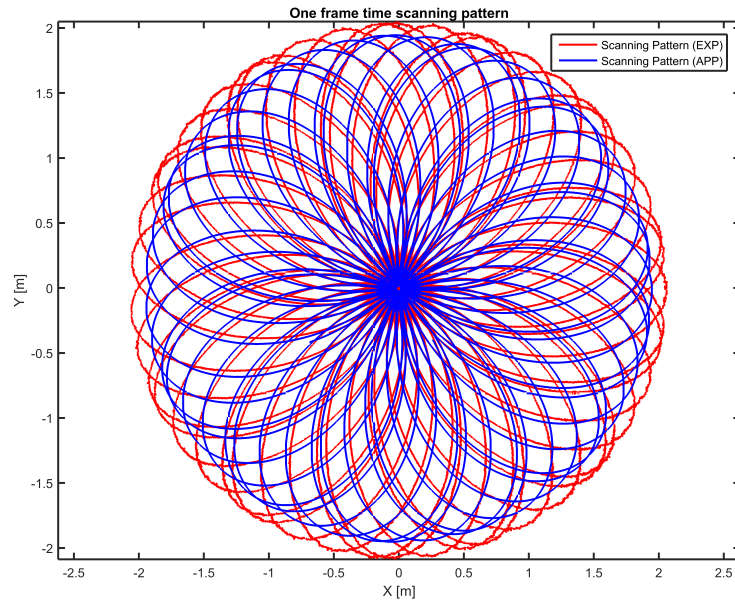
Using the experimental data, the relation between 'target minimum point density' and 'maximum detectable range' as shown in Figure 5.20 for a single target size. The target is approximated by a circle of radius $20cm$. As it can be seen, the approximated model predicts farther detection range for the majority of the time with a maximum of 30% which is due to an error in modeling sensor scanning pattern.

Using the experimental data and for different target size, the relation between 'target size', 'target minimum point density' and 'maximum detectable range' is illustrated in Figure 5.21. Although the sensor might detect the presence of a target farther than what is shown in the graph, the provided graphs show the worst-case scenario which can guarantee detection of the target under proposed circumstances. Proceeding in a similar manner, the effect of different target size and 'target minimum point density' on the 'maximum detectable speed of the target' is illustrated in Figure 5.22. It is shown that for a given target size, the maximum detection speed increases as the target minimum point density decreases.

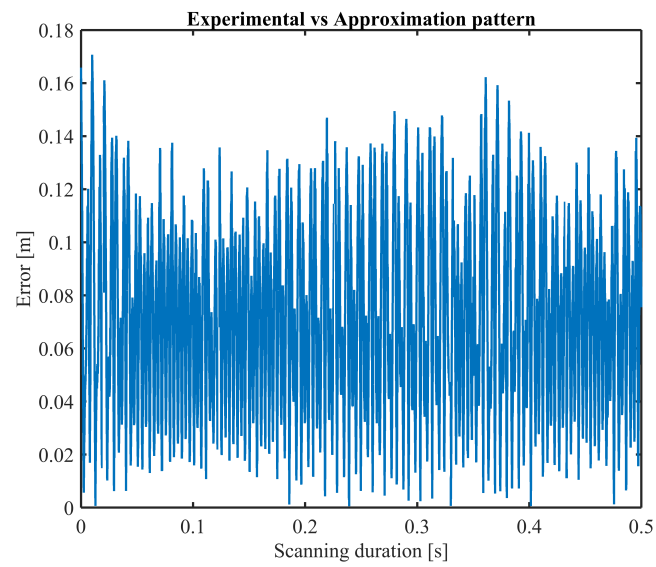
5.4 Conclusion

The definition of the resolution cell provided in Section 5.2.2 is verified through validation of the resolutions. This is done by comparing the theoretical values with experimental measurements of the horizontal, vertical, and depth resolutions. Considering the accuracy of the selected flash LiDAR, the results show that the resolution definitions are reliable.

Furthermore, experimental validation of the mechanical LiDAR scanning pattern is carried out by using scanning data of a stationary sensor. The relation among 'target size', 'target minimum point density' and 'maximum detectable range' and 'maximum detectable speed of the target' was explored which assist us to find the maximum detectable range (z_M) based on the desired application (task parameters) to construct the geometric model of sensor.



(a) Scanning patterns.



(b) Approximated pattern error.

Figure 5.19: Experimental and approximated scanning patterns comparison

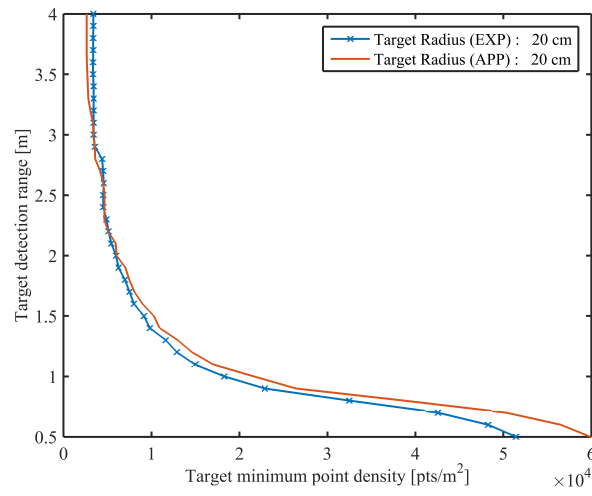


Figure 5.20: Target detection using experimental data and approximated data point density.

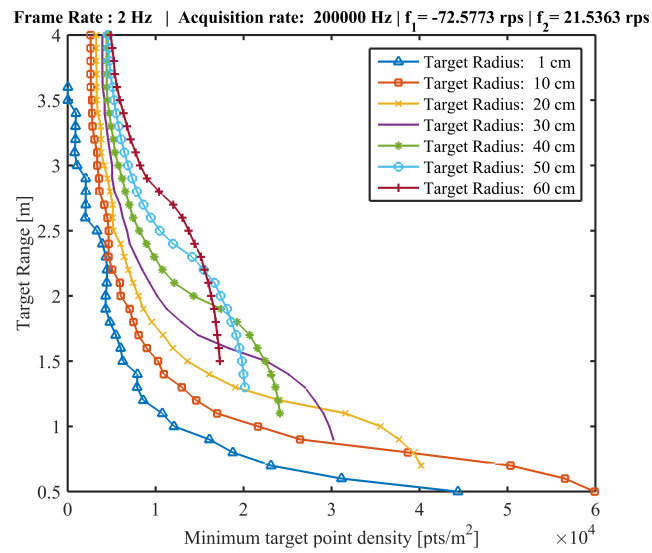


Figure 5.21: Target detection using experimental data and maximum detectable range.

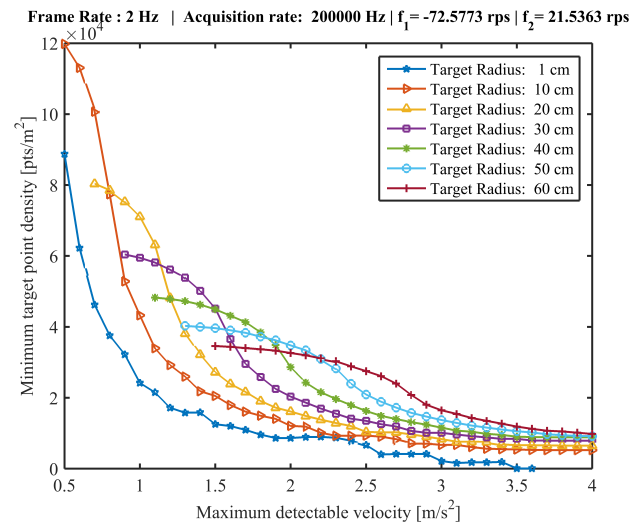


Figure 5.22: Target detection using experimental data and maximum detectable speed.

Solid-state LiDAR Coverage Model

Whoever acquires knowledge but does not practice it is as one who ploughs but does not sow.

Saadi Shirazi (1210-1291)

6.1 Overview

This chapter involves developing a coverage model for the class of solid-state (flash) LiDAR sensors utilizing the coverage model proposed in Section 3.2. This is performed through the identification of those sensor parameters which have the most significant effect on the LiDAR coverage performance (as explained in Chapter 5) and establishing a geometric model from mathematical constraints. Furthermore, an experimental verification is performed to validate the resolution criterion.

6.2 Coverage Model of Flash LiDAR

The coverage model for flash LiDAR sensor is developed in this section by defining the sensor, task and geometric models as follow.

6.2.1 Sensor Model

According to the similarity that exists between sensing mechanism of flash LiDAR and camera sensor, the flash LiDAR can be modeled using pinhole camera model. Therefore, the intrinsic parameters of flash LiDAR sensor can be defined as focal length (f), number and dimension of pixels (W, H), pulse width (T_w), and pulse repetition frequency (PRF). The sensor extrinsic parameters are defined based on the set of parameters presented in Section 3.3.3.

6.2.2 Task Model

The most common parameters which determine the required sensing quality of the environment for applications such as area coverage includes FOV, resolution, range accuracy and detection range which are explained in Chapter 5. Having the task and sensor models available, the sensor sensing region can be specified in the following section.

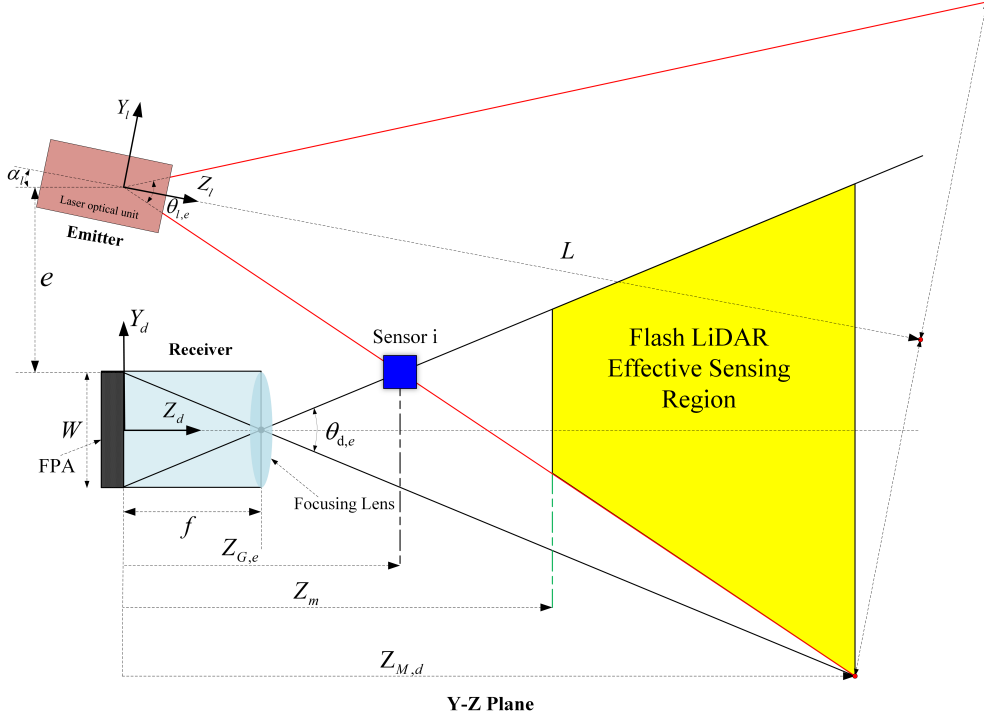


Figure 6.1: Overlooking schematic of effective sensing area for co-axial configuration.

6.2.3 Geometric Model

While the effective sensing region of the field sensors (Figure 6.1) might have a regular geometry such as pyramidal frustum (viewing frustum) for camera sensors or a conical frustum in case of co-axial flash LiDAR sensors, it could have an irregular shape, depending on the relative configuration of emitter and receiver. Figure 6.2 shows an example of irregular shape effective sensing region obtained from co-axial configuration of the flash LiDAR sensor.

Thus, defining the implicit surface covering the sensing region might be very complicated. Therefore, the following method is proposed to construct a geometric model of the sensing region of the flash LiDAR sensor. It maps the region (which presumes to be a star domain) to the ball through radial projection as explain in Section 3.3.2.

Based on the receiver FOV, the visibility region has the shape of the pyramid. Let $D_1 \subset \mathbb{R}^3$ denote the region of a double pyramid bounded by implicit surface function F_1 (Figure 6.3(a)), given by

$$F_1(x_d, y_d, z_d) = \left\| \left[\frac{x_d^2}{\tan^2(\theta_{d,a}/2)} \quad \frac{y_d^2}{\tan^2(\theta_{d,e}/2)} \right] \right\|_{\infty} - z_d^2 \quad (6.1)$$

where $\|\cdot\|_{\infty}$ is the infinity norm. Also, the emitter FOV has an elliptic cone shape. Let $D_2 \subset \mathbb{R}^3$ denote the region of a double elliptic cone modeled by the implicit surface function F_2 (Figure 6.3(c)), defined as

$$F_2(x_l, y_l, z_l) = \frac{x_l^2}{\tan^2(\theta_{l,a}/2)} + \frac{y_l^2}{\tan^2(\theta_{l,e}/2)} - z_l^2 \quad (6.2)$$

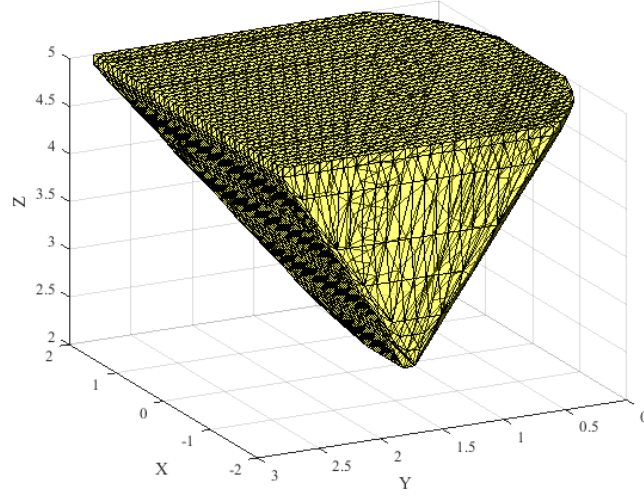


Figure 6.2: Example of the effective sensing region for a co-axial configuration.

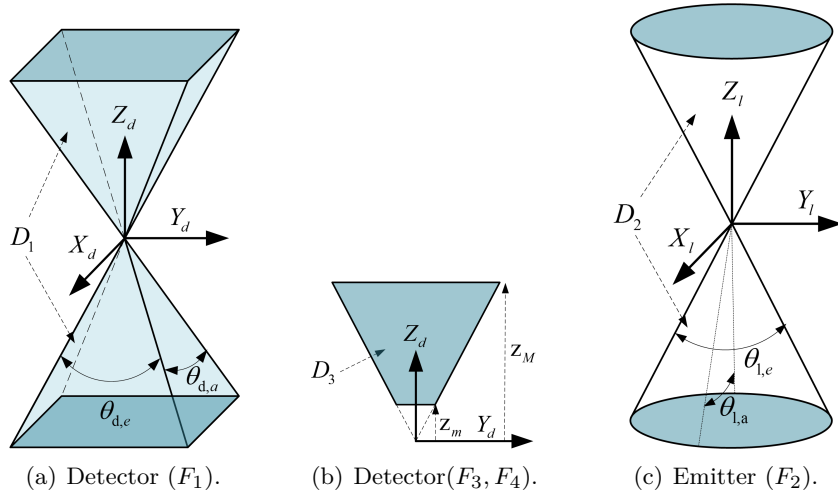


Figure 6.3: Geometric modeling of effective sensing region of flash LiDAR.

Let $D_3 \subset \mathbb{R}^3$ denote the region constructed by considering the minimum Z_m and maximum Z_M detection ranges (Figure 6.3(b)), as

$$\left| \frac{z_d - Z_m}{Z_M - Z_m} - \frac{1}{2} \right| \leq \frac{1}{2} \quad (6.3)$$

by considering the equality sign, the solution will give us two functions,

$$F_3(z_d) = \frac{z_d - Z_m}{Z_M - Z_m} \quad (6.4)$$

$$F_4 = F_3 - 1 \quad (6.5)$$

where $0 \leq z_m < z_M$. In other words, the desired task requirements are finally converted to a set of equality equations. Therefore, the effective sensing region (D_E) of the flash LiDAR is determined by

$$D_E = \bigcap_{i=1}^3 D_i \quad (6.6)$$

Eventually, instead of single implicit surface representation, there is a set of equations describing the geometric model of the sensor using the implicit surface technique.

Proposition 6.1 (Flash LiDAR as a star domain). *The effective sensing region of the flash LiDAR (D_E) is a star domain.*

Proof. The intersection of D_3 with double pyramid and elliptic cone regions includes only upper half of those regions. Since the upper half of the double pyramid and elliptic cone regions (bounded by F_1 and F_2) as well as D_3 are convex regions, their intersections D_E is also a convex region in \mathbb{R}^3 [115]. Thus, according to Remark 3.1, D_E is a star domain with respect to any point $\mathbf{O}_c \in D_E$. ■

6.2.4 Sensor Coverage Model

Given the geometric model of the effective sensing region, the performance measure is developed according to the approach explained in Chapter 3.

Let $\mathbf{r}(t) = \mathbf{O}_c + t\mathbf{u}$ for $t \geq 0$ be the parametric equation of the ray issuing from sensing center \mathbf{O}_c in direction of $\mathbf{u} = \frac{\mathbf{x} - \mathbf{O}_c}{\|\mathbf{x} - \mathbf{O}_c\|}$ where $\mathbf{x} \in \mathbb{R}^3 - \{\mathbf{O}_c\}$. Let Q be defined as the set of all solutions to the system of equations $F_j(\mathbf{r}(t)) = 0$ for $j = 1, 2, 3, 4$, as $Q = \{t | F_j(\mathbf{r}(t)) = 0, t \geq 0, \text{ for } j = 1, \dots, 4\}$.

Proposition 6.2 (Ray intersection point). *For a given point x , the intersection point $\mathbf{x}_i \in \mathbb{R}^3$ of the ray $\mathbf{r}(t)$ and the boundary of the effective sensing region (∂D_E) is determined by $\mathbf{x}_i = \mathbf{r}(t_i) = \mathbf{O}_c + t_i\mathbf{u}$ where $t_i = \{q \in Q | q \leq h, \forall h \in Q\}$.*

Proof. According to proposition 6.1 and definition 3.4, the ray $\mathbf{r}(t)$ should intersect ∂D in only one point. Since the nearest intersection point will be on the ∂D , thus, the smallest element of the set Q will be x_i . ■

Having the intersection point x_i for a given target point \mathbf{V}_t , by recalling from Equation (3.16),

$$\Gamma(\mathbf{x}) = \frac{\|r(t)\|}{\|r(t_i)\|} \quad (6.7)$$

Note that scalar parameter $t_i \in \mathbb{R}^+$ is the function of LiDAR FOV ($\theta_{l,a}, \theta_{l,e}$) and detection ranges (Z_m, Z_M). Finally, for a given directional point (\mathbf{v}_t) the performance measure $d_s(\mathbf{q}, \mathbf{v}_t)$ is defined as

$$d_s(\mathbf{q}, \mathbf{v}_t) = \left\| \begin{bmatrix} \Gamma & \Psi & \Delta(\Gamma + \Psi) \end{bmatrix}^T \right\|_F \quad (6.8)$$

where

$$\Psi(\varphi) = \frac{\tan(\theta_t/2)}{\tan(\theta_a/2)} \quad (6.9)$$

$$\Delta = \lfloor \max(\Gamma, \Psi) \rfloor^+ \quad (6.10)$$

where $\lfloor x \rfloor^+$ denote the largest integer smaller than x , and θ_t, θ_a are the nominal and acceptable view angles defined in Section 3.3.5, respectively.

6.3 Conclusion

In this chapter, the coverage model for the class of solid-state (flash) LiDAR sensors is introduced by developing the geometric model of the sensor, and proving that the obtained geometric model is a star domain. In general, different relative configurations of emitter and receiver (in the world coordinate) lead to different geometry shape of

the effective sensing region of the sensor as the overlapped region will be changed. This means redefining the surface model for the new configurations. This problem is solved by the proposed method, no matter what is the relative configuration of sensor's emitter and receiver (as long as they have overlap), it can easily map the effective sensing region into a ball.

Mechanical LiDAR Coverage Model

The place you are right now.
God circled on a map for you.

Hafez (1315-1390)

7.1 Overview

In this chapter, we develop the coverage model for the class of mechanical LiDAR (Risley-prisms rotating mechanism) sensors using the coverage model developed in Section 3.2. This includes determining the sensing region of LiDAR sensor based on sensor and task models. At the end of this chapter, optimization of the sensor network deployment is conducted utilizing the framework proposed in Section 4.3 and validated through simulation.

7.2 Coverage Model of Mechanical LiDAR

To develop the LiDAR coverage model, we need to derive the sensor and task models.

7.2.1 Sensor Model

The intrinsic parameters of this LiDAR sensor can be considered as focal length (f) for both the detector and emitter optics, pulse width (T_w), and PRF. However, based on selected scanning mechanism, other parameters might be taken into consideration such as the parameters related to geometry and material properties is Risley prisms scanner mechanism. The extrinsic parameters are defined according to the set of parameters provided in Section 3.3.3.

7.2.2 Task Model

The several common parameters which define the required sensing quality of the environment for applications such as area coverage includes FOV, resolution, point density and detection range which is explained in Section 5.3

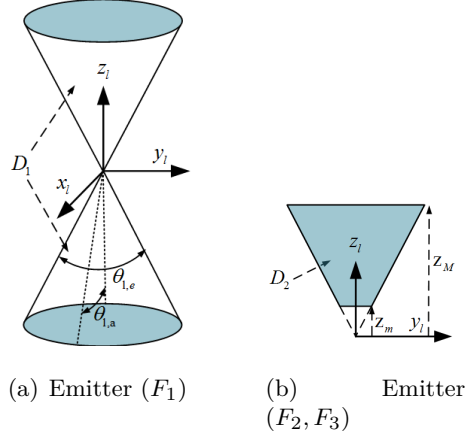


Figure 7.1: The geometric modeling of effective sensing region.

7.2.3 Geometric Model

In order to build the geometric of the sensor sensing region, it is required to convert the sensor model and task model parameters into geometric constraints. According to the LiDAR sensor configuration, the LiDAR visibility region has the shape of the truncated cone. Thus, the sensing region of a double cone ($D_1 \subset \mathbb{R}^3$) bounded by implicit surface function F_1 (Figure 7.1(a)), is given by

$$F_1(x_l, y_l, z_l) = x_l^2 + y_l^2 - \tan^2\left(\frac{\theta_{l,e}}{2}\right) z_l^2 \quad (7.1)$$

Now, by considering sensor detection range and defining $D_2 \subset \mathbb{R}^3$, similar to flash LiDAR case, we have (Figure 7.1(b))

$$F_2(z_l) = \frac{z_l - Z_m}{Z_M - Z_m} \quad (7.2)$$

$$F_3(z_l) = F_2 - 1 \quad (7.3)$$

where $0 \leq Z_m < Z_M$ and Z_m, Z_M are minimum and maximum detection range, respectively. Finally, the effective sensing region (D_E) of the mechanical LiDAR is obtained by $D_E = D_1 \cap D_2$ Figure 7.2. Similar to the flash LiDAR sensor, it can be proved that the effective sensing region of the mechanical LiDAR is a star domain. Therefore, we have a set of equations representing the geometric model of the sensor using the implicit surface technique.

7.2.4 Sensor Coverage Model

Having the effective sensing region of the sensor, we can construct the performance measure according to the approach explained in Chapter 4. Let $\mathbf{r}(t) = \mathbf{O}_c + t\mathbf{u}$ for $t \geq 0$ be the parametric equation of the ray issuing from sensing center \mathbf{O}_c in direction of

$$\mathbf{u} = \frac{\mathbf{x} - \mathbf{O}_c}{\|\mathbf{x} - \mathbf{O}_c\|} \quad (7.4)$$

where $\mathbf{x} \in \mathbb{R}^3 - \{\mathbf{O}_c\}$. Let Q be defined as the set of all solutions to the system of equations $F_j(\mathbf{r}(t)) = 0$ for $j = 1, 2, 3$, as $Q = \{t | F_j(\mathbf{r}(t)) = 0, t \geq 0, \text{ for } j = 1, \dots, 3\}$.

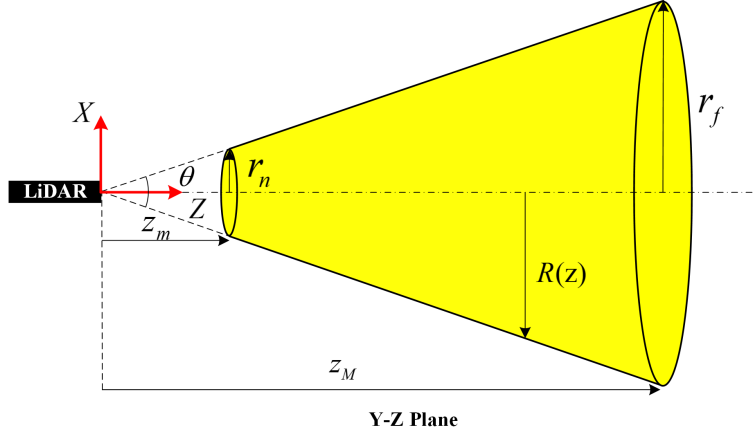


Figure 7.2: Geometric model of the mechanical scanning LiDAR (prism rotating) sensing region.

Let \mathbf{x}_i be the intersection point for a given target (directional) point \mathbf{v}_t , by recalling from Equation (3.16), we have

$$\Gamma(\mathbf{x}) = \frac{\|r(t)\|}{\|r(t_i)\|} \quad (7.5)$$

Finally, the performance measure $d_s(\mathbf{q}, \mathbf{v}_t)$ is defined as

$$d_s(\mathbf{q}, \mathbf{v}_t) = \left\| \begin{bmatrix} \Gamma & \Psi & \Delta(\Gamma + \Psi) \end{bmatrix}^T \right\|_F \quad (7.6)$$

where

$$\Psi(\varphi) = \frac{\tan(\theta_t/2)}{\tan(\theta_a/2)} \quad (7.7)$$

$$\Delta = \lfloor \max(\Gamma, \Psi) \rfloor^+ \quad (7.8)$$

and θ_t, θ_a are the nominal and acceptable view angles (defined in Section 3.3.5), respectively. The coverage model of the mechanical LiDAR sensor is defined utilizing an exponential attenuation model as

$$C_i(\mathbf{q}_i, \mathbf{v}_t) = e^{-\mu d_s(\mathbf{q}_i, \mathbf{v}_t)} \quad (7.9)$$

where $\mu > 0$ is the decaying rate.

7.3 LiDAR Sensor Network Coverage Optimization

In this section, the optimization of LiDAR sensor network deployment is considered. To evaluate the approach proposed in Section 4.3, a simulation is carried out for the LiDAR sensor network deployment optimization in area coverage task. The environment model considered for the area coverage task is shown in Figure 7.3. The target region is an uneven surface having triangular meshes (directional points). Each triangle is represented by a surface normal and the center of the triangle. A network of $n = 7$ sensors placed in random initial configuration (in 3D space) close to the target region (Figure 7.4).

The LiDAR sensors have the conical frustum geometry with $Z_M = 70m$, $Z_m = 0.6m$ and $\theta = 60^\circ$. The decaying rate of the sensor's coverage is selected as $r = 0.01$. The

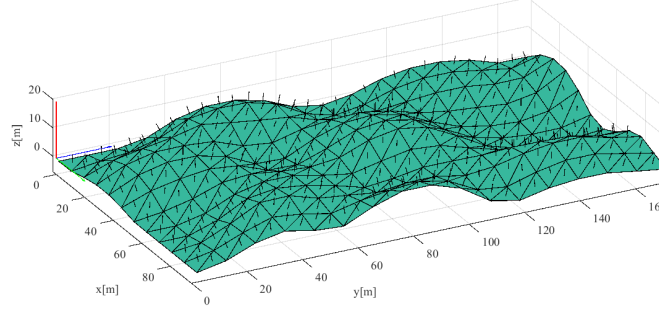


Figure 7.3: The environment model (mesh-based surfaces) selected for area coverage task.

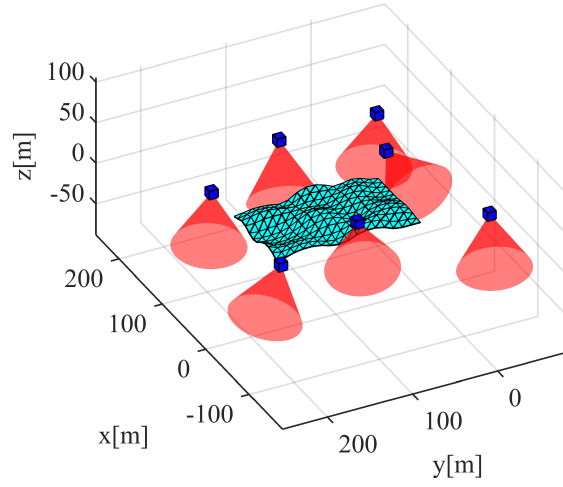


Figure 7.4: Initial configuration of LiDAR sensor network which is randomly deployed in 3D space.

relevance function $\phi(\mathbf{v}_t) = 1$ for all \mathbf{v}_t . For the proposed control law, the proportional constants are set as $K_x = 0.5$ and $K_\varphi = 1.0e - 05$ with the step size of $t_s = 0.1s$.

The sensors were regulated along the gradient direction of the performance function using the control law and after $t = 90s$, the sensors spread over the whole area as it has shown in Figure 7.5. Figure 7.6 shows the performance evaluation of the overall coverage performance function during optimization. It can be observed that \mathcal{H} increased gradually under proposed control law and became stable after $90s$. In fact, the system has converged to a critical point of \mathcal{H} . It is observed that the number of overlapped points gradually increased and reach its maximum value after overall coverage performance changes became stable as shown in Figure 7.7. Figure 7.8 illustrates the partitioning of target area using proposed voronoid approach for initial (7.8(a)) and final (7.8(b)) deployments. As it can be seen that the final region is completely covered by the sensor as each colored assigned to coverage area of one sensor.

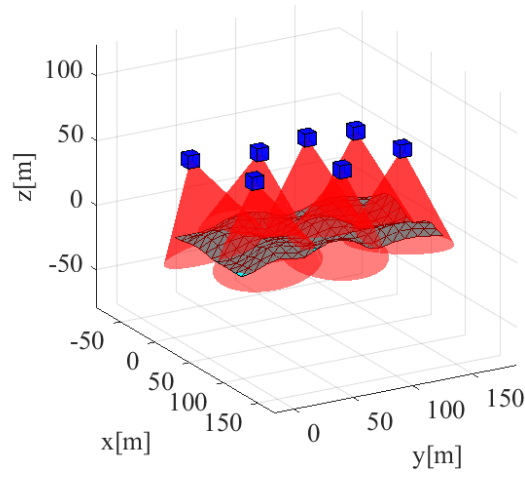


Figure 7.5: Final configuration of LiDAR sensor network after optimization.

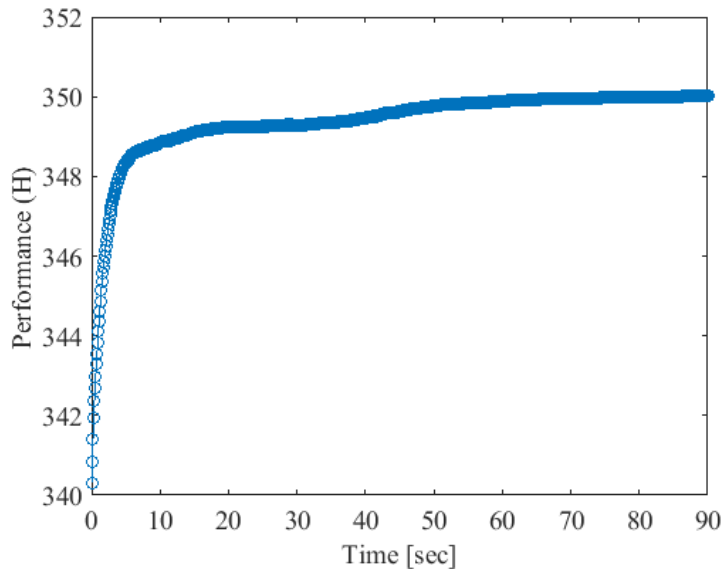


Figure 7.6: The overall coverage performance function.

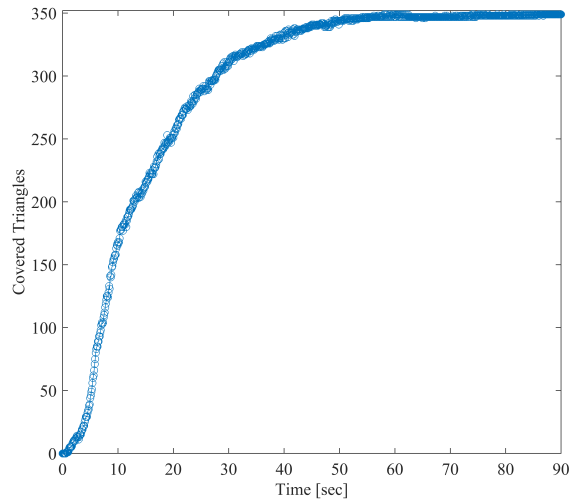
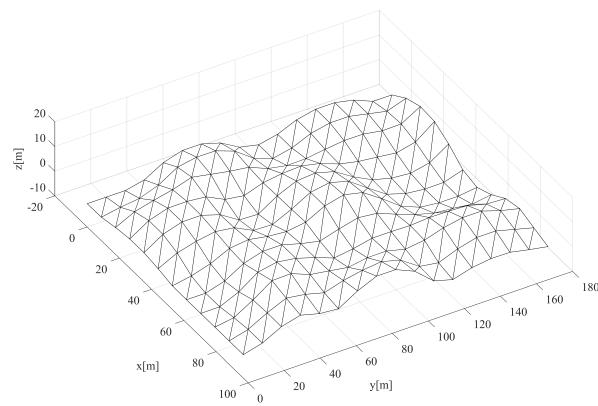


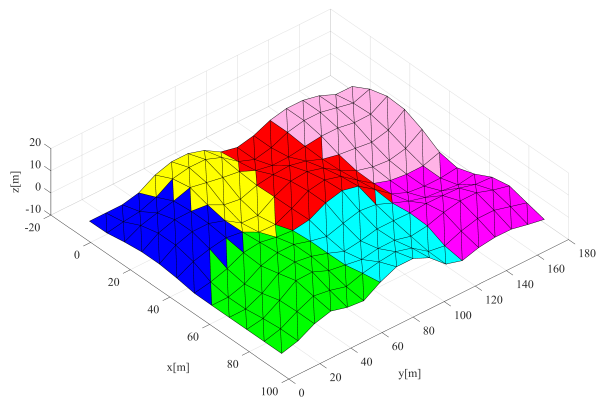
Figure 7.7: The number of covered triangles by LiDAR sensor network during simulation.

7.4 Conclusion

The coverage model for a class of mechanical LiDAR having a pair of prism rotating scanning mechanism is proposed and validated through optimization of the sensor network deployment in the simulation environment for area coverage task.



(a) Initial sensor deployment.



(b) Final sensor deployment.

Figure 7.8: Partitioning of the target area based on the proposed performance measure.

Conclusions

Intellect takes you to the door,
but it doesn't take you into the
house.

Shams Tabrizi (1185-1248)

8.1 Summary of Contributions

This dissertation presents four main contributions. The first contribution of this dissertation is developing the Infinity-norm based performance measure derived in Section 3.2. A gradient-based control law is introduced to optimize a heterogeneous anisotropic field sensor network deployment having different sensing range in Section 4.5.1. The optimal configuration of sensors is determined by making use of both unconstrained and constrained control laws. This approach offers the advantage of both simplicity and proven performance for the proposed field sensors.

The second and the major contribution is developing a coverage model for field sensors based on introducing a performance measures found in Chapter 3. This approach has two inputs of sensor and task models which are translated into geometric constraints, and later converted to geometric model. By employing this model, a performance measure is developed through mapping the sensor sensing region into an \mathbb{B}^n . This measure is a non-negative scalar-valued function that determines the proximity between an object and the field sensor with regard to the position and orientation of the object. Thus, by utilizing an exponential attenuation model of the performance measure the sensor coverage model is proposed.

In contrast to some previous studies, the presented Frobenius-norm based performance measure has the advantage of using the exact sensor geometric model, and it does not suffer from existence of multiple local optima. More importantly, the suggested coverage model proved to be a viable and promising approach that can be implemented to the most commonly used field sensors as they eventually can be considered as integration of disjoint star shapes which is the most distinctive advantage of this method.

The third contribution is developing the geometric model from the sensor and task models of the flash LiDAR sensors to establish the coverage model. This includes defining the sensor (extrinsic and intrinsic) parameters, and the primary parameters required to model the task with industrial inspection and surveillance application in Chapter 5. The different configurations of emitter and receiver lead to distinctive shapes of region boundaries. Therefore, the most important aspect of this approach is that it allows for modeling the effective sensing region of the flash LiDAR, bounded by irregular surfaces,

regardless of its computational complexity in a simple way. Furthermore, an experiment is conducted to validate the resolution cell parameters.

Developing the coverage model for the class of mechanical LiDAR sensors is the forth contribution proposed in Chapter 7. A mechanical LiDAR having the Risley-prism rotating mechanism is selected to define the sensor and task models. This is followed by the analysis of the scanning pattern along with performing simulation and experimental validations for point density of the scanning mechanism. Utilizing the sensor network deployment optimization framework provided in Section 4.4, optimization of the mechanical LiDAR sensor network deployment for covering a 3D environment is conducted, and then validated through simulation.

8.2 Conclusions

A comprehensive approach in the modeling of the field sensors coverage is addressed in this dissertation based on developing a performance measure which is sensitive to position and orientation changes of the target with respect to the sensor. Simulation and comparison with the previous works demonstrate a more competent performance of the proposed measure which leads to the extension of the coverage model for the most commonly used field sensors such as camera, LiDAR, ultrasonic and RADAR.

By implementing this coverage model, an optimization framework for field sensor networks deployment is presented. Although it is a gradient-based approach and there is the possibility to get trapped into undesired local optima, it provides an efficient solution technique for the deployment optimization problem in field sensor networks having a feasible starting point.

The effectiveness of the developed idea was demonstrated and validated through a mechanical LiDAR sensor network deployment. This measure is a powerful tool as it is applicable to the variety of field sensors. Accordingly, we expect this new approach not only reduces the complexity of modeling the performance of different field sensors but also enhance requirement and cost-oriented designs of the sensors.

8.3 Future Research Directions

This dissertation and several related works have the assumption of availability of sensor and target exact configurations where releasing this assumption can provide a more realistic coverage model. One possible solution could be integrating the motion capture system parameters into coverage model.

In modeling the detection range of the LiDAR sensor, only some primary factors are directly implemented in the construction of the geometric model while the existence of other factors that can play a significant role in affecting the detection range has not yet been fully explored. The object reflectivity effect, atmospheric visibility (laser attenuation) and saturation level of the detector are some examples of these factors that can be used to develop a more comprehensive model which in turn can improve the coverage model of the LiDAR sensors.

Owing to the unavailability of the information regarding the flash LiDAR emitter unit, the laser emitter properties (such as laser beam profile) can also be further investigated to obtain a more accurate coverage model.

In this dissertation, a first-order approximation model is used for simulation of mechanical LiDAR scanning pattern while implementation of higher order model of Risley-prism rotating mechanism could enhance the accuracy of scanning pattern model which eventually improve the sensor coverage model through determining a more realistic de-

tection range. In addition, the effect of other scanning mechanisms can be examined and optimized from the coverage point of view.

A centralized approach is proposed for Voronoi partitioning in this study. Developing a distributed partitioning approach is suitable for large-scale networks of heterogeneous anisotropic sensors which is a possible future direction to extend this approach. However, it introduces new challenges for developing an efficient distributed control for the sensor networks.

Theorems, Definitions and Propositions

3.1	Definition (Circular sector coverage)	16
3.2	Definition (Area operator)	16
3.1	Theorem (Necessary and sufficient condition for coverage)	17
3.3	Definition (Convex set)	18
3.4	Definition (Star-convex set)	18
3.1	Remark (Convexity of star domain)	18
3.5	Definition (Homeomorphism map)	19
3.1	Proposition (Radial projection map)	19
3.2	Proposition (Homeomorphism between surface and sphere)	19
3.6	Definition (Directional point coverage)	21
3.2	Theorem (Necessary and sufficient condition for coverage)	22
5.1	Definition (Maximum undetectable circle)	51
5.2	Definition (Target effective area)	52
6.1	Proposition (Flash LiDAR as a star domain)	61
6.2	Proposition (Ray intersection point)	61

Bibliography

- [1] Aleksandar Tomović. “Implementing Lensless Cameras in Autonomous Robotic Systems”. In: (2014).
- [2] Mike Musgrove. “Nikon says it’s leaving film-camera business”. In: *Washington Post*, Jan 12 (2006), p. D01.
- [3] Rucha Dixit, Harshali Chaudhari, Shital Jadhav, and Komal Jagtap. “Water Level and Leakage Detection System with its Quality Analysis based on Sensor for Home Application”. In: (2017).
- [4] Peter Hauptmann, Niels Hoppe, and Alf Püttmer. “Application of ultrasonic sensors in the process industry”. In: *Measurement Science and Technology* 13.8 (2002), R73.
- [5] S Gareth Pierce, Brian Culshaw, Graeme Manson, Keith Worden, and Wieslaw J Staszewski. “Application of ultrasonic Lamb wave techniques to the evaluation of advanced composite structures”. In: *Smart Structures and Materials 2000: Sensory Phenomena and Measurement Instrumentation for Smart Structures and Materials*. Vol. 3986. International Society for Optics and Photonics. 2000, pp. 93–104.
- [6] Jaafar Tarraf, Samir Mustapha, Mohammad Ali Fakih, Mohammad Harb, Hongjian Wang, Georges Ayoub, and Ramsey Hamade. “Application of Ultrasonic Waves Towards the Inspection of Similar and Dissimilar Friction Stir Welded Joints”. In: *Journal of Materials Processing Technology* (2018).
- [7] Johann Borenstein and Yoram Koren. “Obstacle avoidance with ultrasonic sensors”. In: *IEEE Journal on Robotics and Automation* 4.2 (1988), pp. 213–218.
- [8] David Cody Lee Cutright. “Evaluation of Ultrasonic Transducers for Use with Fire Apparatus”. PhD thesis. West Virginia University, 2017.
- [9] Benigno Maqueira, Charles I Umeagukwu, and Jacek Jarzynski. “Application of ultrasonic sensors to robotic seam tracking”. In: *IEEE transactions on robotics and automation* 5.3 (1989), pp. 337–344.
- [10] Luciano Alonso Rentería et al. *Contribución al estudio de sistemas ultrasónicos y su aplicación a la seguridad activa en vehículos inteligentes*. Universidad de Cantabria, 2009.
- [11] Kirtan Gopal Panda, Deepak Agrawal, Arcade Nshimiyimana, and Ashraf Hos-sain. “Effects of environment on accuracy of ultrasonic sensor operates in mil-limetre range”. In: *Perspectives in Science* 8 (2016), pp. 574–576.
- [12] Qin Zhang. *Precision agriculture technology for crop farming*. CRC Press, 2015.
- [13] Luciano Alonso, Vicente Milanés, Carlos Torre-Ferrero, Jorge Godoy, Juan P Ori-a, and Teresa De Pedro. “Ultrasonic sensors in urban traffic driving-aid systems”. In: *Sensors* 11.1 (2011), pp. 661–673.

- [14] Kunihiro Hoshino, Michio Shimada, Shoichi Hara, Kazuo Hitomi, Michihiro Kameyama, Hiroshi Yamanouch, Toshifumi Hori, Masahiko Sasano, Kenjiro Hikida, Naoki Niida, et al. "On Examination of the Detection Method of Leakage Oil from Sunken Ship and Quantity of the Remained Oil Using Ultrasonic Wave". In: *The Fifteenth International Offshore and Polar Engineering Conference*. International Society of Offshore and Polar Engineers. 2005.
- [15] A Buck, JM Keller, M Popescu, D Sheen, and RH Luke. "Target detection in high-resolution 3D radar imagery". In: *Detection and Sensing of Mines, Explosive Objects, and Obscured Targets XXII*. Vol. 10182. International Society for Optics and Photonics. 2017, 101821G.
- [16] Dominic Zeng Wang and Ingmar Posner. "Two Approaches to Radar-Based Moving Object Detection". In: ().
- [17] Snezhana Jovanoska, Felix Govaers, and Reiner Thoma. "People tracking and data fusion for UWB radar applications". In: *Novel Radar Techniques and Applications: Waveform Diversity and Cognitive Radar and Target Tracking and Data Fusion 2* (2017), p. 429.
- [18] John Schroeder, Brian Hirth, and Jerry Guynes. *Apparatus and method for using radar to evaluate wind flow fields for wind energy applications*. US Patent 9,575,177. 2017.
- [19] Amirshahram Hematian, Yinan Yang, Chao Lu, and Sepideh Yazdani. "Human Motion Analysis and Classification Using Radar Micro-Doppler Signatures". In: *Software Engineering Research, Management and Applications*. Springer, 2016, pp. 1–10.
- [20] Yogesh Anil Nijasure, Georges Kaddoum, Nazih Khaddaj Mallat, Ghyslain Gagnon, and Francois Gagnon. "Cognitive chaotic UWB-MIMO detect-avoid radar for autonomous UAV navigation". In: *IEEE Transactions on Intelligent Transportation Systems* 17.11 (2016), pp. 3121–3131.
- [21] Musa Aydin and Emin Kuğu. "Safe landing site detection using SRTM data for the Unmanned Aerial Vehicles". In: *Signal Processing and Communication Application Conference (SIU), 2016 24th*. IEEE. 2016, pp. 2125–2128.
- [22] Michael J Caruso, Tamara Bratland, Carl H Smith, and Robert Schneider. "A new perspective on magnetic field sensing". In: *SENSORS-PETERBOROUGH-15* (1998), pp. 34–47.
- [23] Henry P Baltes and Radivoje S Popovic. "Integrated semiconductor magnetic field sensors". In: *Proceedings of the IEEE* 74.8 (1986), pp. 1107–1132.
- [24] Pavel Ripka. "Security applications of magnetic sensors". In: *Journal of Physics: Conference Series*. Vol. 450. 1. IOP Publishing. 2013, p. 012001.
- [25] Paul H Willms and James H Stanley. *Active threat detection and elimination while in transit*. US Patent 7,180,418. 2007.
- [26] Sotoshi Yamada. "High-spatial-resolution magnetic-field measurement by giant magnetoresistance sensor Applications to nondestructive evaluation and biomedical engineering". In: *International Journal on Smart Sensing and Intelligent Systems* 1.1 (2008), pp. 160–175.
- [27] Fang Wu, Akash Vibhute, Gim Song Soh, Kristin L Wood, and Shaohui Foong. "A Compact Magnetic Field-Based Obstacle Detection and Avoidance System for Miniature Spherical Robots". In: *Sensors* 17.6 (2017), p. 1231.
- [28] Marina Díaz-Michelena. "Small magnetic sensors for space applications". In: *Sensors* 9.4 (2009), pp. 2271–2288.

-
- [29] *Magnetic field sensor example*. <http://intechchennai.com/appProxiSensor.php>. Accessed: 2018-02-01.
 - [30] Patrick Alexander Hölzl and Bernhard G Zagar. “Improving the spatial resolution of magneto resistive sensors via deconvolution”. In: *IEEE Sensors Journal* 13.11 (2013), pp. 4296–4304.
 - [31] Fang Wu, Luc Maréchal, Akash Vibhute, Shaohui Foong, Gim Song Soh, and Kristin L Wood. “A compact magnetic directional proximity sensor for spherical robots”. In: *Advanced Intelligent Mechatronics (AIM), 2016 IEEE International Conference on*. IEEE. 2016, pp. 1258–1264.
 - [32] Mercy Ndinda Kiio. “Design and Implementation of Microcontroller Based Motor Vehicle Speed Governor using a Magnetostrictive Amorphous Wire Speed Sensor”. PhD thesis. JKUAT COETEC, 2018.
 - [33] David Crolla. *Encyclopedia of automotive engineering*. John Wiley & Sons, 2015.
 - [34] Luiz GB Mirisola, Jorge Lobo, and Jorge Dias. “3D Map Registration using Vision/Laser and Inertial Sensing.” In: *EMCR*. 2007.
 - [35] Lei Chen, Ping Li, Yumei Wen, and Yong Zhu. “Note: High sensitivity self-bias magnetoelectric sensor with two different magnetostrictive materials”. In: *Review of Scientific Instruments* 84.6 (2013), p. 066101.
 - [36] Heiner Lasi, Peter Fettke, Hans-Georg Kemper, Thomas Feld, and Michael Hoffmann. “Industry 4.0”. In: *Business & Information Systems Engineering* 6.4 (2014), pp. 239–242.
 - [37] M Amac Guvensan and A Gokhan Yavuz. “On coverage issues in directional sensor networks: A survey”. In: *Ad Hoc Networks* 9.7 (2011), pp. 1238–1255.
 - [38] Aaron Mavrinac. “Modeling and optimizing the coverage of multi-camera systems”. In: (2012).
 - [39] Jose Alarcon. “A Measure of Vision Distance for Optimization of Camera Networks”. In: (2014).
 - [40] Xuebo Zhang, Xiang Chen, Xiao Liang, and Yongchun Fang. “Distributed coverage optimization for deployment of directional sensor networks”. In: *Decision and Control (CDC), 2015 IEEE 54th Annual Conference on*. IEEE. 2015, pp. 246–251.
 - [41] Xuebo Zhang, Xiang Chen, Jose Luis Alarcon-Herrera, and Yongchun Fang. “3-D model-based multi-camera deployment: a recursive convex optimization approach”. In: *IEEE/ASME Transactions on Mechatronics* 20.6 (2015), pp. 3157–3169.
 - [42] JA Krill, MJ O’Driscoll, MC Gross, SJ Papadakis, GF Ricciardi, JS Peri, and IN Bankman. “Multifunction array LiDAR network for intruder detection, tracking, and identification”. In: *Intelligent Sensors, Sensor Networks and Information Processing (ISSNIP), 2010 Sixth International Conference on*. IEEE. 2010, pp. 43–48.
 - [43] Evan Trickey, Dan Lucifora, PAS Wan, and Andrew Scott. “Enabling mine automation through the application of neptecs opal and 3dri technology”. In: *Proceedings of the 30th International Symposium on Automation and Robotics in Construction and Mining (ISARC)*. 2013, pp. 377–386.
 - [44] Stéphane Chevrel and Anne Bourguignon. “Application of Optical Remote Sensing for Monitoring Environmental Impacts of Mining: From Exploitation to Post-mining”. In: *Land Surface Remote Sensing*. Elsevier, 2017, pp. 191–220.

- [45] Chris A Hostetler, Michael J Behrenfeld, Yongxiang Hu, Johnathan W Hair, and Jennifer A Schulien. "Spaceborne lidar in the study of marine systems". In: *Annual review of marine science* 0 (2018).
- [46] Christopher Edwards. "Analysis of Stream Bed Morphology in Oil and Gas Development Areas Using LiDAR Data". In: (2017).
- [47] Harutoshi Ogai and Bishakh Bhattacharya. "Pipe Inspection Robots for Gas and Oil Pipelines". In: *Pipe Inspection Robots for Structural Health and Condition Monitoring*. Springer, 2018, pp. 13–43.
- [48] Jeff Hecht. "Lidar for Self-Driving Cars". In: *Optics and Photonics News* 29.1 (2018), pp. 26–33.
- [49] Cregg K. Cowan and Peter D Kovesi. "Automatic sensor placement from vision task requirements". In: *IEEE Transactions on Pattern Analysis and machine intelligence* 10.3 (1988), pp. 407–416.
- [50] Konstantinos Tarabanis and Roger Y Tsai. "Computing viewpoints that satisfy optical constraints". In: *Radiometry*. Jones and Bartlett Publishers, Inc. 1992, pp. 399–406.
- [51] Xuebo Zhang, Xiang Chen, Farsam Farzadpour, and Yongchun Fang. "Deployment of a Multi-Camera Network through Distributed Coverage Optimization ŪA Visual Distance Approach". submitted to IEEE/ASME Trans. Mechatronics, manuscript no. MECH-01-2017-6279(Accepted with minor revision). 2018.
- [52] KR Guruprasad and Debasish Ghose. "Heterogeneous locational optimisation using a generalised Voronoi partition". In: *International Journal of Control* 86.6 (2013), pp. 977–993.
- [53] Azwirman Gusrialdi, Sandra Hirche, David Asikin, Takeshi Hatanaka, and Masayuki Fujita. "Voronoi-based coverage control with anisotropic sensors and experimental case study". In: *Intelligent Service Robotics* 2.4 (2009), pp. 195–204.
- [54] Jing Ai and Alhussein A Abouzeid. "Coverage by directional sensors in randomly deployed wireless sensor networks". In: *Journal of Combinatorial Optimization* 11.1 (2006), pp. 21–41.
- [55] Mirko Mahlich, Roland Schweiger, Werner Ritter, and Klaus Dietmayer. "Sensorfusion using spatio-temporal aligned video and lidar for improved vehicle detection". In: *Intelligent Vehicles Symposium, 2006 IEEE*. IEEE. 2006, pp. 424–429.
- [56] Paul Dolce. *A Statistical Approach to Fusing 2-D and 3-D LADAR Systems*. Tech. rep. AIR FORCE INST OF TECH WRIGHT-PATTERSON AFB OH GRADUATE SCHOOL OF ENGINEERING and MANAGEMENT, 2011.
- [57] Seongjoon Kim, Impyeong Lee, and Yong Joon Kwon. "Simulation of a Geiger-mode imaging lidar system for performance assessment". In: *sensors* 13.7 (2013), pp. 8461–8489.
- [58] Yan Zhao, Shaokun Han, Wen Zhao, Ping Wang, and Wenze Xia. "The influence of atmospheric turbulence on 3D flash LiDAR range imagery". In: *International Conference on Optical Instruments and Technology (OIT2013)*. International Society for Optics and Photonics. 2013, 90460G–90460G.
- [59] CH Jang, CS Kim, KC Jo, and M Sunwoo. "Design factor optimization of 3D flash LiDAR sensor based on geometrical model for automated vehicle and advanced driver assistance system applications". In: *International journal of automotive technology* 18.1 (2017), pp. 147–156.

- [60] Sebastian Thrun. “A probabilistic on-line mapping algorithm for teams of mobile robots”. In: *The International Journal of Robotics Research* 20.5 (2001), pp. 335–363.
- [61] Alexander Schaefer, Lukas Luft, and Wolfram Burgard. “An Analytical LiDAR Sensor Model Based on Ray Path Information”. In: *IEEE Robotics and Automation Letters* 2.3 (2017), pp. 1405–1412.
- [62] Konrad Wenzl, Heinrich Ruser, and Christian Kargel. “Configuration of a Sparse Network of LIDAR Sensors to Identify Security-Relevant Behavior or People”. In: *Proc. of SPIE*. Vol. 7480. 2009, p. 748007.
- [63] Konrad Wenzl, Heinrich Ruser, and Christian Kargel. “Decentralized multi-target-tracking using a LiDAR sensor network”. In: *Instrumentation and Measurement Technology Conference (I2MTC), 2012 IEEE International*. IEEE. 2012, p-p. 2492–2497.
- [64] Joseph W Starr and BY Lattimer. “Evidential Sensor Fusion of Long-Wavelength Infrared Stereo Vision and 3D-LIDAR for Rangefinding in Fire Environments”. In: *Fire Technology* 53.6 (2017), pp. 1961–1983.
- [65] Ayman F Habib, Ana P Kersting, Ahmed Shaker, and Wai-Yeung Yan. “Geometric calibration and radiometric correction of LiDAR data and their impact on the quality of derived products”. In: *Sensors* 11.9 (2011), pp. 9069–9097.
- [66] Ananth Vadlamani, Mark Smearcheck, and M Uijt de Haag. “Preliminary design and analysis of a lidar based obstacle detection system”. In: *Digital Avionics Systems Conference, 2005. DASC 2005. The 24th*. Vol. 1. IEEE. 2005, 6–B.
- [67] Phillip J Durst, Christopher Goodin, Burhman Q Gates, Christopher L Cummins, Burney McKinley, Jody D Priddy, Peter Rander, and Brett Browning. “The Need for High-Fidelity Robotics Sensor Models”. In: *Journal of Robotics* 2011 (2011).
- [68] Carlos Gálvez del Postigo Fernández. *Grid-Based Multi-Sensor Fusion for On-Road Obstacle Detection: Application to Autonomous Driving*. 2015.
- [69] Yeonsik Kang, Derek Caveney, and J Karl Hedrick. “Real-time Obstacle Map Building with Target Tracking.” In: *JACIC* 5.5 (2008), pp. 120–134.
- [70] Seonghong Min, Seongjoon Kim, and Impyeong Lee. “Data simulation of Ladar sensor: Focusing on geometric modeling”. In: *Proceedings of the XXI ISPRS Congress, Commission I, Beijing, China*. 2008, pp. 3–11.
- [71] Bang Wang. *Coverage control in sensor networks*. Springer Science & Business Media, 2010.
- [72] Novella Bartolini, Tiziana Calamoneri, Tom F La Porta, and Simone Silvestri. “Autonomous deployment of heterogeneous mobile sensors”. In: *IEEE Transactions on Mobile Computing* 10.6 (2011), pp. 753–766.
- [73] Hamid Mahboubi and Amir G Aghdam. “Distributed deployment algorithms for coverage improvement in a network of wireless mobile sensors: Relocation by virtual force”. In: *IEEE Transactions on Control of Network Systems* (2016).
- [74] Marco Pavone, Alessandro Arsie, Emilio Frazzoli, and Francesco Bullo. “Equitable partitioning policies for robotic networks”. In: *Robotics and Automation, 2009. ICRA’09. IEEE International Conference on*. IEEE. 2009, pp. 2356–2361.
- [75] Katie Laventall and Jorge Cortés. “Coverage control by multi-robot networks with limited-range anisotropic sensory”. In: *International Journal of Control* 82.6 (2009), pp. 1113–1121.

- [76] Guodong Shi and Yiguang Hong. “Region coverage for planar sensor network via sensing sectors”. In: *IFAC Proceedings Volumes* 41.2 (2008), pp. 4156–4161.
- [77] Yi-Ge Fu, Jie Zhou, and Lei Deng. “Surveillance of a 2D plane area with 3D deployed cameras”. In: *Sensors* 14.2 (2014), pp. 1988–2011.
- [78] SY Chen and YF Li. “Automatic sensor placement for model-based robot vision”. In: *IEEE Transactions on Systems, Man, and Cybernetics, Part B (Cybernetics)* 34.1 (2004), pp. 393–408.
- [79] Samil Temel, Numan Unaldi, and Okayay Kaynak. “On deployment of wireless sensors on 3-D terrains to maximize sensing coverage by utilizing cat swarm optimization with wavelet transform”. In: *IEEE Transactions on Systems, Man, and Cybernetics: Systems* 44.1 (2014), pp. 111–120.
- [80] Aaron Mavrinac and Xiang Chen. “Optimizing load distribution in camera networks with a hypergraph model of coverage topology”. In: *Distributed Smart Cameras (ICDSC), 2011 Fifth ACM/IEEE International Conference on*. IEEE. 2011, pp. 1–7.
- [81] Boyu Zhang, Xuebo Zhang, Xiang Chen, and Yongchun Fang. “A differential evolution approach for coverage optimization of visual sensor networks with parallel occlusion detection”. In: *Advanced Intelligent Mechatronics (AIM), 2016 IEEE International Conference on*. IEEE. 2016, pp. 1246–1251.
- [82] Jorge Cortes, Sonia Martinez, and Francesco Bullo. “Spatially-distributed coverage optimization and control with limited-range interactions”. In: *ESAIM: Control, Optimisation and Calculus of Variations* 11.4 (2005), pp. 691–719.
- [83] Md Mofijul Islam, Md Ahasanuzzaman, Md Abdur Razzaque, Mohammad Meheddi Hassan, Abdulhameed Alelaiwi, and Yang Xiang. “Target coverage through distributed clustering in directional sensor networks”. In: *EURASIP Journal on Wireless Communications and Networking* 2015.1 (2015), p. 167.
- [84] Mac Schwager, Brian J Julian, Michael Angermann, and Daniela Rus. “Eyes in the sky: Decentralized control for the deployment of robotic camera networks”. In: *Proceedings of the IEEE* 99.9 (2011), pp. 1541–1561.
- [85] Jorge Cortes, Sonia Martinez, Timur Karatas, and Francesco Bullo. “Coverage control for mobile sensing networks”. In: *IEEE Transactions on robotics and Automation* 20.2 (2004), pp. 243–255.
- [86] Mustapha Reda Senouci, Abdelhamid Mellouk, and Khalid Assnoute. “Localized movement-assisted sensordeployment algorithm for holedetection and healing”. In: *IEEE Transactions on parallel and distributed systems* 25.5 (2014), pp. 1267–1277.
- [87] Yiannis Stergiopoulos and Anthony Tzes. “Cooperative positioning/orientation control of mobile heterogeneous anisotropic sensor networks for area coverage”. In: *Robotics and Automation (ICRA), 2014 IEEE International Conference on*. IEEE. 2014, pp. 1106–1111.
- [88] Farsam Farzadpour, Xuebo Zhang, Xiang Chen, and Tong Zhang. “On performance measurement for a heterogeneous planar field sensor network”. In: *Advanced Intelligent Mechatronics (AIM), 2017 IEEE International Conference on*. IEEE. 2017, pp. 166–171.
- [89] María Santos, Yancy Diaz-Mercado, and Magnus Egerstedt. “Coverage Control for Multi-Robot Teams With Heterogeneous Sensing Capabilities”. In: *IEEE Robotics and Automation Letters* (2018).

- [90] Stanislava Soro and Wendi Heinzelman. “A survey of visual sensor networks”. In: *Advances in multimedia* 2009 (2009).
- [91] Konstantinos A Tarabanis, Peter K Allen, and Roger Y Tsai. “A survey of sensor planning in computer vision”. In: *IEEE transactions on Robotics and Automation* 11.1 (1995), pp. 86–104.
- [92] Aaron Mavrinac and Xiang Chen. “Modeling coverage in camera networks: A survey”. In: *International journal of computer vision* 101.1 (2013), pp. 205–226.
- [93] Jose Luis Alarcon-Herrera, Xiang Chen, and Xuebo Zhang. “Viewpoint selection for vision systems in industrial inspection”. In: *Robotics and Automation (ICRA), 2014 IEEE International Conference on*. IEEE. 2014, pp. 4934–4939.
- [94] Konrad Wenzl, Heinrich Ruser, and Christian Kargel. “Multiple hypothesis tracking of two persons using a network of LiDAR sensors with stationary and directional beams”. In: *Proc. of SPIE Vol.* Vol. 7710. 2010, 77100B–1.
- [95] Konrad Wenzl, Heinrich Ruser, and Christian Kargel. “Performance evaluation of a decentralized multitarget-tracking algorithm using a LIDAR sensor network with stationary beams”. In: *IEEE Transactions on Instrumentation and Measurement* 62.5 (2013), pp. 1174–1182.
- [96] C Toth, G Jozkova, Z Koppanyi, S Young, and D Grejner-Brzezinska. “MONITORING AIRCRAFT MOTION AT AIRPORTS BY LIDAR.” In: *ISPRS Annals of Photogrammetry, Remote Sensing & Spatial Information Sciences* 3.1 (2016).
- [97] Bernard Mourrain, Scott Schaefer, and Guoliang Xu. *Advances in Geometric Modeling and Processing: 6th International Conference, GMP 2010, Castro Urdiales, Spain, June 16-18, 2010, Proceedings*. Vol. 6130. Springer, 2010.
- [98] Martin R Bridson and André Haeffliger. *Metric spaces of non-positive curvature*. Vol. 319. Springer Science & Business Media, 2013.
- [99] Wilson A Sutherland. *Introduction to metric and topological spaces*. Oxford University Press, 2009.
- [100] Jules Bloomenthal and Chandrajit Bajaj. *Introduction to implicit surfaces*. Morgan Kaufmann, 1997.
- [101] Aaron Mavrinac, Xiang Chen, and Yonghong Tan. “Coverage quality and smoothness criteria for online view selection in a multi-camera network”. In: *ACM Transactions on Sensor Networks (TOSN)* 10.2 (2014), p. 33.
- [102] *Mesh of Stanford bunny*. <http://mech.fsv.cvut.cz/~dr/papers/Habil03/node51.html>. Accessed: 2018-01-06.
- [103] Mac Schwager. *A gradient optimization approach to adaptive multi-robot control*. Tech. rep. MASSACHUSETTS INST OF TECH CAMBRIDGE, 2009.
- [104] PK Kundu, IM Cohen, and DR Dowling. *Fluid Mechanics, vol. 2*. 2002.
- [105] Jose Alarcon. “A Measure of Vision Distance for Optimization of Camera Networks”. In: (2014).
- [106] Daniel W Jaynes, James F Manwell, Jon G McGowan, William M Stein, and Anthony L Rogers. “MTC final progress report: LIDAR”. In: *Renewable Energy Research Laboratory, Department of Mechanical and Industrial Engineering, University of Massachusetts* (2007).
- [107] Ibrahim A Jawad, Marianne L Taylor, Freida Pruitt-Hudson, and Young Ho Sohn. “Range ambiguity in pulsed Doppler ultrasound: The ambiguity clarified?” In: *Journal of clinical ultrasound* 13.7 (1985), pp. 475–479.

-
- [108] H Horvath. “Atmospheric visibility”. In: *Atmospheric Environment (1967)* 15.10-11 (1981), pp. 1785–1796.
- [109] Philip Church, Kiatchai Borribanbunpotkat, Evan Trickey, Peter Iles, and Michael Sekerka. “Overview of the commercial OPAL LiDAR optimized for rotorcraft platforms operating in degraded visual environments”. In: *Proc. SPIE*. Vol. 9087. 2014, p. 908703.
- [110] Craig L Glennie, William E Carter, Ramesh L Shrestha, and William E Dietrich. “Geodetic imaging with airborne LiDAR: the Earth’s surface revealed”. In: *Reports on Progress in Physics* 76.8 (2013), p. 086801.
- [111] Philip Church, Justin Matheson, Xiaoying Cao, and Gilles Roy. “Evaluation of a steerable 3D laser scanner using a double Risley prism pair”. In: *SPIE Defense+ Security*. International Society for Optics and Photonics. 2017, 101970O–101970O.
- [112] Joshua D Vande Hey. *A Novel LiDAR Ceilometer: Design, Implementation and Characterisation*. Springer, 2014.
- [113] *PointDensity*. <http://felix.rohrba.ch/en/2015/point-density-and-point-spacing/>. Accessed: 2018-02-01.
- [114] Yafei Lu, Yuan Zhou, Mo Hei, and Dapeng Fan. “Frame frequency prediction for Risley-prism-based imaging laser radar”. In: *Applied optics* 53.16 (2014), p-p. 3556–3564.
- [115] Hoang Tuy, Tuy Hoang, Tuy Hoang, Việt-nam Mathématicien, Tuy Hoang, and Vietnam Mathematician. *Convex analysis and global optimization*. Springer, 1998.

Vita Auctoris

NAME: Farsam Farzadpour

PLACE OF BIRTH: Iran

YEAR OF BIRTH: 1984

EDUCATION: Doctor of Philosophy in Electrical and Computer Engineering,
University of Windsor, Windsor, Ontario, Canada, 2018.

Master of Science in Mechanical Engineering,
Azad University, Isfahan, Iran, 2011.

Bachelor of Science in Mechanical Engineering,
Azad University, Isfahan, Iran, 2007.